The Management of Large-Scale Photovoltaic Arrays

Zuyu Wu

PhD

University of York

Electronic Engineering

January 2021

Abstract

Photovoltaic (PV) power generation is a crucial new type of green energy in today's society. However, the relevant technologies are still not entirely mature. It is worth noting that the safety and power generation issues of PV arrays are attracting significant attention from not only engineers and manufacturers but also scholars. Since PV modules are affected by external conditions, such as tree shade, bird drops, and dust particles, its power generation efficiency is significantly reduced. In addition, a small area of accumulation on the surface of PV panels will induce the hot spot effect, which may cause firestorms.

In order to prevent PV fires and improve the efficiency of PV power generation, this thesis analyzes specific safety issues and demonstrates treatment strategies to improve PV power generation and its safety simultaneously. Firstly, considering the impact of sand and dust, the relationship between dust accumulation and power generation is drawn using numerical simulation, which can predict the influence of dust accurately. Secondly, for non-uniform aging PV arrays, a new reorganization strategy is proposed to improve its power generation. Finally, aiming at the fire issue of large-scale PV arrays, a new strategy is proposed, which improves the power generation and the safety factor. The research and knowledge of this thesis will be of great significance for future development of PV power generation and will expand the scope of this topic to a new level.

Table of Contents

Abstract....2
Table of Contents....3
List of Tables....6
List of Figures....7
Acknowledgements....9
Declaration....10
Publications....11
Abbreviations....12
Chapter 1 Introduction....14
1.1 Motivation....14
1.2 Dissertation Outline....16
Chapter 2 A Review for Solar Panel Fire Accident Prevention in Large-Scale PV Applications 18
2.1 Background....18
2.2 Root Cause Analysis for Solar Panel Fire Accidents....20
2.2.1 The hot-spot effect....20
2.2.2 Cables aging effect....25
2.2.3 Other conditions....27
2.3 Solutions to Prevent PV Fire Accidents....29
2.3.1 Preventive maintenance action in PV array....30
2.3.1.1 Construction analysis....30
2.3.1.2 Structure analysis....32
2.3.2 Fault diagnosis....35
2.3.2.1 Physical analysis....35
2.3.2.2 Fast Fourier transform....36
2.3.2.3 Time domain analysis....37
2.3.2.4 Wavelet analysis....38

2.3.2.5 Artificial intelligence method 39
2.3.3. Discussion 41
2.4 Summary 43
Chapter 3 Time-effective Dust Deposition Analysis of PV Modules Based on Finite Element Simulation for Candidate Site Determination 45
3.1 Introduction 45
3.2 Design of Dust Accumulation on PV Modules 47
3.2.1 Boundray conditions of simulation 48
3.2.1.1 Discrete phase 50
3.2.1.2 Turbulence model 51
3.2.2 Experiment setup 52
3.3 Results 55
3.3.1 Simulation results 55
3.3.1.1 Simulation results of dust deposition 55
3.3.1.2 Simulation results of the TKE 58
3.3.2 Experiment results 60
3.3.2.1 Accuracy of simulation 60
3.3.2.2 Impacts of dust depostion on temperatura and output of PV panels 61
3.4 Summary 63
Chapter 4 Cost Effective Offline Reconfiguration for Large-Scale Non-Uniformly Aging Photovoltaic Arrays Efficiency Enhancement 65
4.1 Introduction 65
4.2 Mathematical Modeling 68
4.3 Modeling The Cost of Reconfiguration 70
4.3.1 Calculation of permutation number based on branch and bound method 71
4.3.2 Cost analysis of PV array reconstruction 73
4.4. Simulation and Case Studies 74
4.5 Summary 83

Chapter 5 A New Strategy of PV Fire Prevention in Large-Scale PV Arrays: A Hybrid PV Array of Monofacial and Bifacial PV Modules 84
5.1 Introduction 84
5.2 Modeling of BPV Modules 86
5.3 Thermal Model of MPV and BPV 90
5.3.1 Thermal model of mPV 92
5.3.2 Thermal model of bPV 95
5.4 Thermal Model of MPV and BPV Configuration of The PV Array 97
5.4.1 Fire propagation 97
5.4.2 Cost-effectiveness 98
5.5 Experiment Results 99
5.6 Summary 106
Chapter 6 Conclusions and Future Work 108
6.1 Summary 108
6.2 Future Work 110
Reference 112

List of Tables

TABLE 2-1 Property of PV cells [14] 19
TABLE 2-2 Surface Temperature of PV Panels 23
TABLE 2-3 Fire Proof Solution of PV Modules 41
TABLE 3-1 Surface Temperature of PV Panels Parameter of PV Panels 53
TABLE 3-2 Turbulence Coefficient 55
TABLE 4-1 Electricity Price and Labor Remuneration in 2019 74
TABLE 4-2 PV array before arrangement for second case in China 75
TABLE 4-3 PV array before arrangement for second case in USA 76
TABLE 4-4 PV array before arrangement for second case in UK 77
TABLE 4-5 PV array before arrangement for second case in turkey 78
TABLE 4-6 PV array before arrangement for second case in Saudi 79
TABLE 4-7 Economic benefit analysis considering the minimum handling times 82
TABLE 4-8 Economic benefit analysis without considering the minimum handling times 82
TABLE 5-1 The parameters of PV materials 91
TABLE 5-2 The scales of experiment facilities 100

List of Figures

Fig. 1-1. Worldwide PV installationbs in 2018 [3]. 14

Fig. 2-1. The structure of a PV module 19

Fig. 2-2. Factors lead to PV module fire accidents 20

Fig. 2-3. Hot spot effect [13] 21

Fig. 2-4. The types of PV shading. (a) 1st shading test (b) 2nd shading test (c) 3rd shading test [20] 23

Fig. 2-5. Three types of PV arc failures 25

Fig. 2-6. Experimental setup to simulate a fire accident of solar panels 27

Fig. 2-7. Damaged combiner box by fire [32] 27

Fig. 2-8. PV module crack [36] 28

Fig. 2-9. Detection methods for PV fires accidents 30

Fig. 2-10. Dust deposition on a PV array 31

Fig. 2-11. Solution to prevent PV fires on roof-top PV array 32

Fig. 2-12. Reconfiguration of PV string. (a) bypass diode circuit (b) ON-OFF MOSFET circuit (c) 16F977A microcontroller circuit (d) TCL555 microcontroller circuit 35

Fig. 2-13. Arc detection neural network model [85] 40

Fig. 2-14. A diagram of SVM trained samples [88] 41

Fig. 3-1. Module of computation domain for the case of monsoons. (a) traditional method [109] (b) proposed method 49

Fig. 3-2. Average wind speed in England (www.xcweather.ac.uk). 49

Fig. 3-3. Measurement of RS PV panel 53

Fig. 3-4. Simulation results of dust deposition in various air conditions 56

Fig. 3-5. Diagram of dust deposition on the PV panel. (a) 0° wind direction (b) 30° wind direction (c) 45° wind direction (d) 60° wind direction (e) 90° wind direction 58

Fig. 3-6. The TKE of PV array in CFD. (a) the left view of dust particle deposition of 100 μm dust diameter with 5 m/s wind velocity (b) the top view of dust particle deposition of 100 μm dust diameter on 10 m/s wind velocity 59

Fig. 3-7. Comparison of experiment value and simulation value of dust deposition. (a) 0° wind direction (b) 30° wind direction (c) 45° wind direction (d) 60° wind direction (e) 90° wind direction 61

Fig. 3-8. Measured data (a) temperature-voltage curve (b) P-V curve.....63

Fig. 4-1. Without and with rearrangement. (a) without rearrangement (b) Output character (Without) (c) with rearrangement (d) Output character (With).....66

Fig. 4-2. PV array reconfiguration strategy. (a) PV array reconfiguration (b) PV array reconfiguration considering lobor cost 68

Fig. 4-3. Schematic diagram of PV module replacement.....71

Fig. 4-4. Flowchart of the proposed algorithm 73

Fig. 5-1. Modeling of total irradiance of components during sunrise and sunset 89

Fig. 5-2. Generation modeling of bPV components 90

Fig. 5-3. Multi-layer structure of the (a) mPV and (b) bPV panels.....92

Fig. 5-4. The equivalent thermal circuit of mPV.....93

Fig. 5-5. The equivalent thermal circuit for the bPV module.....96

Fig. 5-6. The installation strategy of the hybrid PV array 97

Fig. 5-7. The facilities of experiment 100

Fig. 5-8. The comparison of thermal test between bPV and mPV from 10:00 a.m. to 15:00 p.m. 101

Fig. 5-9. The procedure of combustion experiment 102

Fig. 5-10. The change of bPV heating.....103

Fig. 5-11. The results of thermogravimetric experiments. (a) bPV (b) mPV.....104

Fig. 5-12. The procedure of heating experiment 106

Acknowledgements

First and foremost, I would like to express my deepest gratitude to my main supervisor, Dr. Yihua Hu, for granting me the precious opportunity to further myself at the highest level. You have encouraged and helped me to progress academically from a fresh graduate to a professional researcher and a mature individual. I have learned so much from you both academically and personally. Thank you for the invaluable comments and advice on my research as well as my life and career. It is a great honour for me to be your PhD student, and I hope I have fulfilled your high expectations and faith through my achievements. Secondly, I would also like to thank my second supervisor Dr. Ruwan Gajaweera, for the generous support and academic guidance you have provided me. I will always treasure your support, encouragement and guidance.

I would also like to take this opportunity and thank my parents, especially my mother. You have always been greatly supportive of me. Your continuous help and understanding have made my life full of love, and I am grateful for everything you have done. Additionally, I would like to express my appreciation to my girlfriend. I am very thankful to her for her patience, tolerance, company and warm love. I have to say without your help, I would not have made it this far. Special thanks are also paid to my brilliant and lovely colleagues and friends; in particular to Dr. Sen Song, Dr. Kai Ni, and Chao Gong for many fruitful discussions and enjoyable moments.

Last but not least, the support from the Electronic Engineering Department of the University of York is gratefully acknowledged.

Declaration

I declare that this thesis is a presentation of original work and I am the sole author. This work has not previously been presented for an award at this, or any other, University. All sources are acknowledged as References.

Publications

[1] **Z. Wu**, Z. Zhou and M. Alkahtani, “Time-Effective Dust Deposition Analysis of PV Modules Based on Finite Element Simulation for Candidate Site Determination,” *IEEE Access*, vol. 8, pp. 65137-65147, 2020, doi: 10.1109/ACCESS.2020.2985158.

[2] **Z. Wu**, C. Zhang, M. Alkahtani, Y. Hu and J. Zhang, “Cost Effective Offline Reconfiguration for Large-Scale Non-Uniformly Aging Photovoltaic Arrays Efficiency Enhancement,” *IEEE Access*, vol. 8, pp. 80572-80581, 2020, doi: 10.1109/ACCESS.2020.2991089.

[3] **Z. Wu**, Y. Hu, J. X. Wen, F. Zhou and X. Ye, “A Review for Solar Panel Fire Accident Prevention in Large-Scale PV Applications,” *IEEE Access*, vol. 8, pp. 132466-132480, 2020, doi: 10.1109/ACCESS.2020.3010212.

[4] M. Alkahtani, **Z. Wu**, “A Novel PV Array Reconfiguration Algorithm Approach to Optimising Power Generation across Non-Uniformly Aged PV Arrays by Merely Repositioning,” *Multidisciplinary Scientific Journal*, 2020, 3(1), 32-53; https://doi.org/10.3390/j3010005.

[5] M. Alkahtani, **Z. Wu** and Y. Hu, “Gene Evaluation Algorithm for Reconfiguration of a Medium and Large Size PV Arrays Exhibition Non-Uniformly Aging," *Energies*, 2020, 13(8), 1921; https://doi.org/10.3390/en13081921.

[6] **Z. Wu**, W. Li, S. Kuka and M. Alkahtani, “Analysis of Dust Deposition on PV Arrays by CFD Simulation,” *IECON 2019 - 45th Annual Conference of the IEEE Industrial Electronics Society, Lisbon, Portugal*, 2019, pp. 5439-5443, doi: 10.1109/IECON.2019.8926897.

Abbreviations

PV	Photovoltaic
bPV	Bifacial Photovoltaic
mPV	Monofacial Photovoltaic
CO_2	Carbon Oxide
O_2	Oxygen
CFD	Computational Fluid Dynamic
FE	Finite Element
UK	United Kingdom
DC	DC current
IGBT	Insulated gate bipolar translator
MPPT	Maximum Power Point
GMPPT	Global Maximum Power Point
2D	Two Dimention
3D	Three Dimention
CdTe	Cadmium Telluride
EVA	Ethylene-vinyl Acetate
PET	Polythylene Terephthalate
TPT	Tedlar Polyester Tedlar
CIGS	Copper Indium Gallium Selenide
STC	Standard Testing Condition
CO	Carbon Monoxide
HF	Hydrogen Fluoride

HCL	Hydrogen Chloride
SO_2	Sulfur Dioxide
HCN	Formonitrile
UL	Insurer Laboratary
TKE	Turbulence Kinetic Energy
MOSFET	Metal-Oxide -Semiconductor Field Effect Transistor
FFT	Fast Fourier Transform
MCD	Minimum Covariance Determine
FIR	Finite Impulse Response
ANN	Artificial Neural Network
SVM	Support Vector Machines
DPM	Discrete Phase Model
VOF	Volume of Fluid
SiC	Silicon Carbon
ECM	Earth Capacitance Measurement
TDR	Time Domain Reflectomery
RTCT	Reconfigurable Total Cross-tied
COA	Classical Optimization Algorithm
B&B	Branch and Bound
GA	Genetic Algorithm
PERC	Passivated Emitter and Rear Contact

Chapter 1 Introduction

1.1 Motivation

Compared with traditional thermal power generation, photovoltaic (PV) power generation is endowed with numerous competitive advantages, because it is renewable and environmentally friendly. Moreover, PV power is an essential factor for achieving global sustainable development strategies as it generates no greenhouse gas emissions such as carbon dioxide, saving costs on emission control. For example, every doubling of installed monocrystalline silicon and polycrystalline silicon PV systems would reduce greenhouse gas emissions of the world by 24% and 17%, respectively [1]. Therefore, with rising concerns of global energy shortage and environmental pollution, PV power generation technologies attract increasing attention. Statistics show that the total installed capacity of PV power was 480.357 GW, which occupied 22.33% of the total installed renewable energy capacity of the world in 2018 [2]. Besides, according to the list of PV installations in each country around the globe in 2019 released by the International Renewable Energy Agency (IRENA), the latest global solar installed capacity was 97.1 GW, of which the newly installed capacities in Asia, Europe, America, Africa, and the Middle East were 56 GW, 19 GW, 12.8 GW, 1.2 GW, and 2 GW, respectively [3]. The major PV installation countries and their cumulative PV installations are illustrated in Figure 1-1.

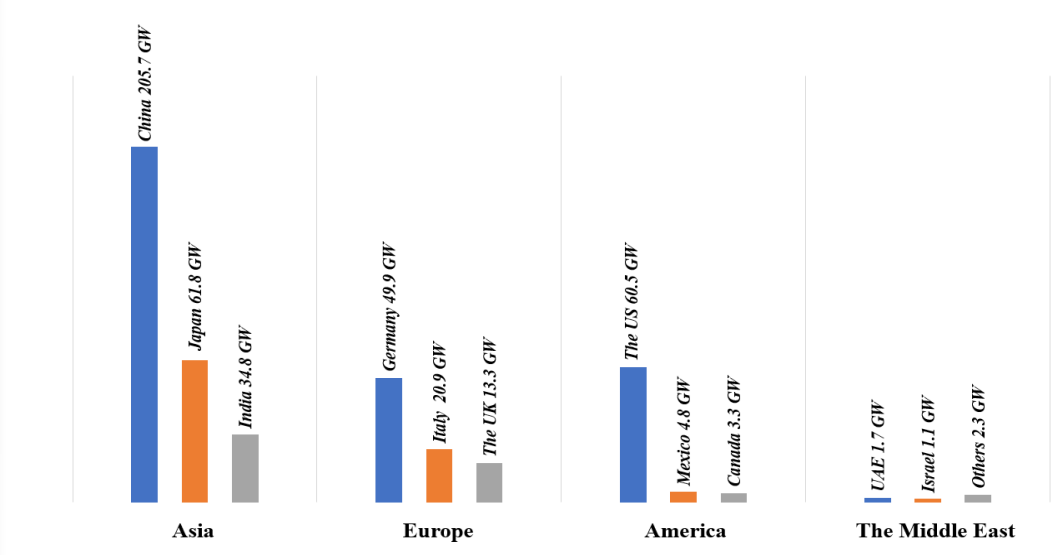

Fig. 1-1. Worldwide PV installationbs in 2018 [3].

However, in the growing PV industry, PV arrays still face challenges such as power generation efficiency, PV system failure, and fire risks. With the development of PV-integrated building applications, the efficiency and safety of PV power generation have attracted much attention. At

present, dust accumulation is the main factor affecting the efficiency of PV arrays. When soils such as sand and dust cover PV panels in large areas, the shading blocks the sunlight and results in power loss. The power loss caused by regional differences varies from 4.4% to 43% [4]. When a small area of accumulated dust blocks the PV panel, the PV cells underneath will heat up sharply. The PV panel will overheat and damage when the temperature of the cells reaches a certain point, known as the hot spot effect. As the PV industry is witnessing vigorous development, power efficiency and safety issues are the challenges to overcome. These issues are being investigated and researched by not only manufacturers but also engineers and scholars.

As PV power generation is regarded as the future direction of energy generation, it is essential to study the related technologies that can improve PV safety and power generation efficiency, further promoting the development of PV industry. It was recently reported that a significant data center of Apple in Arizona was on fire, where more than 300 solar PV modules were damaged. Similarly, the PV array of Taipei Water Park caught fire, covering an area of about 400 m^2 [5]. In recent years, many similar accidents occurred, causing widespread public concerns about the safety of PV arrays. Currently, the PV array safety-related research is a hot topic in electrical engineering, including hot spot effect, DC arcs, reconfiguration, fault detection, etc. Although various mature technologies have been widely adopted in these areas, scholars and engineers are continually seeking new technologies to improve the safety level and power output efficiency of PV arrays. In this thesis, the author conducted a comprehensive study on the safety issue of large-scale PV arrays. Innovative solutions are also proposed to be applied in the PV engineering applications.

The target of this work is to overcome three common but challenging problems in large-scale PV arrays, which are shown as follows:

i. To establish a highly accurate 3D calculation model with the predictions and characteristics of local dust accumulation, simultaneous power generation, and temperature of PV modules by using numerical simulation. The current PV arrays follow Computational Fluid Dynamics (CFD) calculation and are mostly based on the traditional 2D model, which is unable to observe the distribution of soil accumulation on PV panels. The proposed calculation method is equipped to observe the amount of accumulated dust and precise temperature control of PV cells. Moreover, the proposed calculation model's incident flow can be divided into five incident angles, which can calculate the dust fall of the PV panel surface according to the monsoon wind, thereby improving the reliability of dust distribution of a PV array.

ii. In the view of addressing the low power generation caused by non-uniform aging in large-scale PV arrays and profit maximization, a PV reconfiguration strategy based on genetic algorithms is proposed. The strategy reduces the exchange time of PV modules and achieves the maximum power simultaneously without needing a replacement. In contrast, the traditional solution for non-uniform aging in PV arrays is to replace brand-new PV modules manually, which is labor-intensive and material-consuming. Therefore, the strategy will save maintenance costs and improve power generation efficiency, which will be highly favoured by industrial applications.

iii. As for the fire hazard of PV arrays, a novel array reorganization strategy is proposed, which is a hybrid array of bifacial and monofacial PV modules. This strategy can effectively prevent the spread of fire in the array and avoid large-scale combustion events. The traditional preventive method for PV fires is to regularly inspect and clean PV modules, which will consume extensive manpower and financial resources in large-scale arrays. In contrast, the new strategy is cost-friendly and low-risk, and it improves the array output. In addition, this method is fault-tolerant and improves the reliability of the hybrid PV array.

1.2 Dissertation Outline

This research focuses on comprehensively and innovatively solving the urgent problems of fire and power generation in large-scale PV arrays. The dissertation consists of six chapters. An outline of the structure is organized as follows:

Chapter 1 introduces the motivation of this study and the challenges that need to be solved in this study. Besides, the objectives and a brief introduction of the research contents are illustrated.

Chapter 2 comprehensively reviews the threats that PV arrays face, the consequences of the hot spot effect, and the current solutions. The purpose is to highlight that PV arrays have various threats of power generation efficiency reduction and combustion, and it is necessary to investigate the causes. Moreover, effective management can provide guidance for future research on improving the safety of PV arrays.

Chapter 3 discusses the proposed calculation method that includes an accurate 3D model to predict dust accumulation on PV panels. Firstly, the development and principles of the model are explained. Secondly, the inlet conditions of the calculation model are studied to expand its feasibility under different monsoon conditions. Finally, the function of the calculation model is introduced in detail according to the working conditions of the target regions, such as wind speed,

latitude, and ambient temperature. Moreover, the output power under the corresponding conditions is found to match different management strategies.

Chapter 4 introduces the PV array reconfiguration strategy based on a genetic algorithm to solve the non-uniform aging problem in large-scale PV arrays. The swapping among rows is employed to form a new array to achieve the purpose of increasing profit. By calculating and comparing the PV power generation revenue of five different countries, the feasibility of the new strategy was verified.

Chapter 5 introduces a new type of PV array installation strategy, namely, a hybrid array of monofacial and bifacial PV modules, which solves the fire safety problem of PV arrays. Firstly, the heat transfer of the two types of PV panels is analyzed, and the relationship between the ignition temperature and the ambient temperature is explored. Secondly, according to the turbulence field analysis, a safe row-to-row space is defined in the array. Finally, in the context of safe installation, the row-to-row space with the maximum output power is further defined.

Chapter 6 draws a summary of the main contributions of this dissertation. It also provides suggestions for future research areas.

Chapter 2 A Review for Solar Panel Fire Accident Prevention in Large-Scale PV Applications

2.1 Background

PV panels have been widely applied to harness solar power for their renewable and environment-friendly features. However, the working environment of PV panels is usually not pleasant in practice, leading to fast aging and degradation of power generation, and the PV panels even suffer from risks of fire accidents. According to [6], there is a 2% probability that a fire may occur to PV arrays each year, with 0.6% of the fire accidents occurring in residential areas and 3.5% of them started from some roof-top PV modules.

When the solar panels catch fire, it results in power generation reduction and causes secondary damage such as toxic gas emissions. As shown in Fig. 2-1, the constituent materials of a PV panel are mostly organics. The energy released by glass fiber, ethylene-vinyl acetate, and polyethylene terephthalate (PET) compounds in making epoxy resin printed circuit boards are 1.012, 0.54, 0.073 MJ, respectively, based on the data from Tewarson and Quintiere [7]. Hydrogen compounds such as HF and HCL that are toxic are produced during the fire accident of solar panels. In 2009, 1826 PV modules with a generation capacity of 383 kW solar PV arrays were damaged in a fire accident in California, USA [8]. In the same year, another 15 solar PV module-related fire accidents were reported in the Netherlands [9]. In 2012, a solar panel-related fire occurred in a warehouse in Goch, Germany, which caused a burning area of about 4000 m^2 [8].

The root cause of the solar panel-related fire accident is usually associated with a deficit in the PV system. Previous analysis of solar panel fire events indicated that the causes of fire could be divided into two types: arc fault and spontaneous combustion [5][10]. The main reasons for the arc failure include low quality of PV modules, installation errors, and DC arc ignition backboard induced by junction and combiner boxes. Some aging solar panels, especially those with components not meeting their specified standards, can spontaneously ignite under high temperatures and sunlight due to chemical reactions and hot spot effects [11].

Solar panels can be made from crystalline silicon or amorphous. At present, the materials used for PV cells vary in different regions [12]. For example, according to Table 2-1, based on the characteristics of high melting point, low density, and good highlight performance, the crystalline silicon is suitable for the roof-top installation in residential areas. To avoid fire accidents, some

fire-proof obstacles must be installed between two modules, which effectively prevent the spread of fire in a large-scale PV array. Practically, more thin-film PV modules are used in urban areas. This, along with other technologies such as highly efficient CdTe single-junction cells, can achieve the fastest response speed in the visible range. For example, based on the mean spectral ratio, which is the ratio of smoky and clear irradiance in Table 2-1, the value of CdTe is smaller than other PV cells. It is illustrated that the effect of smoke on CdTe is the greatest. Meanwhile, the smoke in the near-infrared and infrared ranges has the least effect on monocrystalline silicon cells in the visible range. It has the highest response due to the thin-film technologies (e.g., copper indium gallium selenide (CIGS) solar cells). These results have an impact on PV fire-prone areas [13-14]. As for the protection from fire of ground PV array for commercial use, the installation distance between each module can be calculated according to different materials of PV modules.

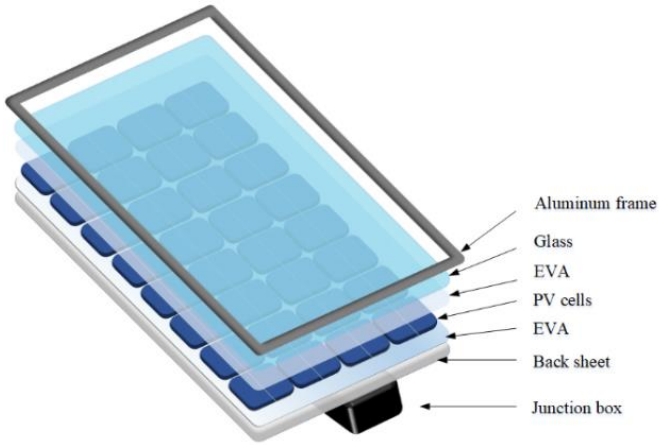

Fig. 2-1. The structure of a PV module

TABLE 2-1 PROPERTY OF PV CELLS [14]

	Monocrystalline	Polycrystalline	CdTe	GIGS
Melting point	1420 °C	1410 °C	1092 °C	986 °C
Material density	2.32 g/cm^3	2.32 g/cm^3	5.85 g/cm^3	5.75 g/cm^3
Mean spectral ratio (smoky/clean)	0.9246	0.9211	0.9175	0.9213

In large-scale PV arrays, the power generation mismatch accelerates the aging process of the solar panels [15] due to non-uniform patterns of shading, irradiance, and temperature of each panel. According to [16], approximately 51% of the PV related fire accidents are related to installation errors or low quality of PV modules, which further causes cable faults on PV modules. On the

contrary, the hot-spot effect is liable for a relatively lower percentage of solar panel fire accidents. The low manufacturing quality of solar panels is a significant contributor to solar panel fire accidents. In order to reduce the risks of solar field panel-related fire accidents, this review summarizes the causal factors and some effective fire prevention solutions to the field solar panels. There are two leading solutions to alleviating the hot spot effect in PV arrays, namely restructuring PV modules and reconstruction of the distribution of PV arrays. As aged PV modules are easier to cause DC arc shock and damage, real-time fault detection mechanisms are helpful for preventing such damages. In addition, solar panels must be tested against strict engineering standards to reduce the risks of fire damage post-installation.

In the following sections, a comprehensive review will be provided for solar panel fire accidents in large-scale PV applications. Section 2.2 illustrates the reasons for the solar PV related fire accidents, which include hot-spot effect, DC arc, and other conditions. In Section 2.3, the methods for reducing the probability of solar PV-related fire accidents are discussed, which include structure reconfiguration and fault diagnosis. Section 2.4 presents the summary.

2.2 Root Cause Analysis for Solar Panel Fire Accidents

According to the summaries of [5][7][10][11][16][18-37], the main causes of PV fires are shown in Fig. 2-2. There are 36% of fire events caused by installation errors, and 15% accidents caused by the quality of PV modules [16]. Most fire events were found to be caused by DC arc [22-31] due to low quality of PV modules, lack of drainage of PV systems, aging of combiner box, and aging of IGBTs in inverters. In addition, the hot spot effect should not be overlooked [18-21].

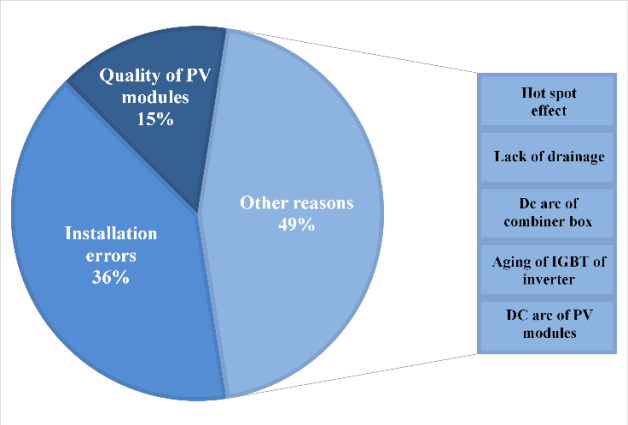

Fig. 2-2. Factors leading to PV module fire accidents

2.2.1 Hot-spot effect

In PV modules, series-connected cells are usually used. Some PV cells suffer from partial shades from surrounding objects, such as fallen leaves, dust accumulation, and bird drops, while other PV modules do not. Hot spots may be produced due to non-uniform power generation status amongst the PV cells. The hot spot effect occurs if the temperature exceeds 5% above the standard temperature in a period in the standard testing condition (STC, 1000 W/m^2, 25 °C). Since the performance of PV cells is different in several cases, some shaded PV cells have obvious defects. The hot spot effect increases the local currents and voltages of PV modules, which results in a local temperature rise on the PV module, causing the modules to spontaneously ignite. Fig. 2-3 shows a PV fire accident, which was caused by the hot spot effect.

Fig. 2-3. Hot spot effect [13]

Under the STC, the hot spot temperature of opaque PV modules is higher than that of semitransparent PV modules by 2~3 °C, which drops with an increment as far as the numbers and areas of hot spots are concerned. Moreover, the efficiencies of PV modules have been predicted in the one and two hot-spot situations. For the one-hot-spot situation, the efficiencies of opaque and semitransparent PV modules are 10.41% and 10.62%, respectively. In the two incidents involving hot spots, the efficiencies of the opaque and semitransparent PV modules are 10.41% and 10.54%, respectively [18]. Hu et al. [19] compared different degrees of shading and found that the minor size shading would cause the temperature of the PV panel in the shaded part to rise rapidly to cause a fire. Hu et al. [20] tried to obtain the condition of the hot spot effect by comparing different shading conditions on PV modules. They found that different levels of impacts result from different environments. The experimental conditions of the irradiance and surface temperature of PV panels are (820 W/m^2, 25 °C), (740 W/m^2, 22 °C), and (690 W/m^2, 24 °C), respectively. The shading comparison diagram is shown in Fig. 2-4. For the first shading tests, three PV panels were connected in series, with one of them covered with an opaque material to simulate the partial shades. It was recorded by the thermal imager that a hot spot was observed at the location of the shade. During the period of minor shading, the I-V curve was shifted

dramatically. In Fig. 2-4, $V_{m'}$ is the voltage of an unhealthy module, and V_{array} is the voltage of the PV array. Fig. 2-4 (b) shows the second shading test, where a PV module was partially covered by tissue paper to create a partial shade on the solar panel so that certain lighting can penetrate the paper and reach the solar panel. In the experiment, the faulty power unit was short-circuited by a bypass diode until it cannot generate enough current to support the load, shown as the shift in the I-V curve. I_f is the shaded module current, and I_H is the healthy module current. As for the third shading test shown in Fig. 2-4 (c), three PV panels were covered to create a large size of the shade. In this case, the shaded PV areas were short-circuited through the bypass diode, and all solar energy was converted into heat, such as the shift of I_f in the I-V curve. However, a healthy PV panel can still convert the partial incoming solar energy into electricity, thereby decreasing the panel temperature. The comparative results shown in Table 2-2 illustrates that the only significant temperature increase is presented for the case with minor shading, which is prone to generate hot spots in PV modules.

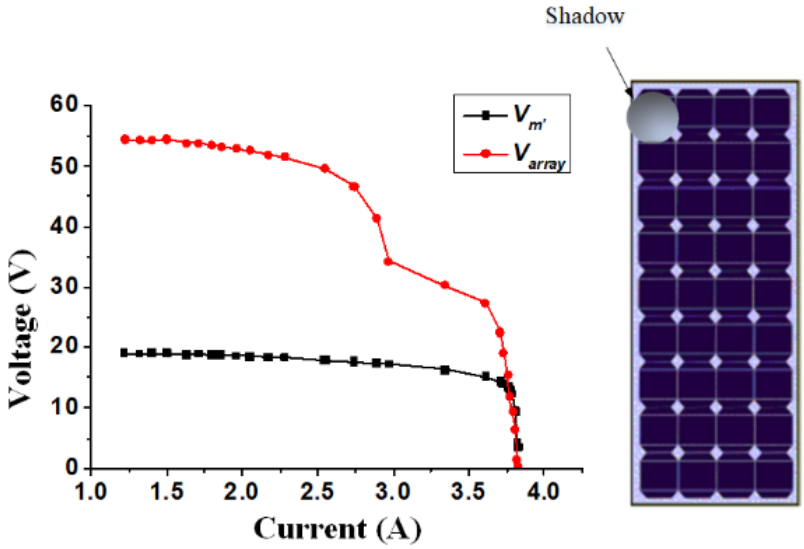

(a)

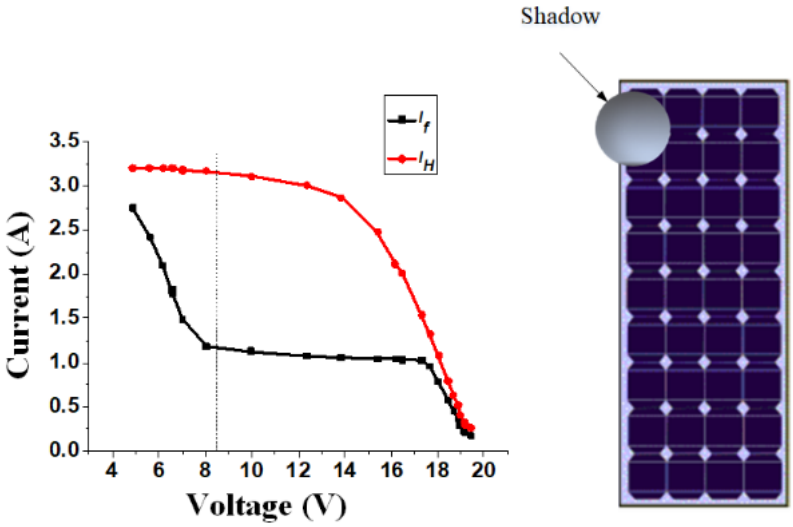

(b)

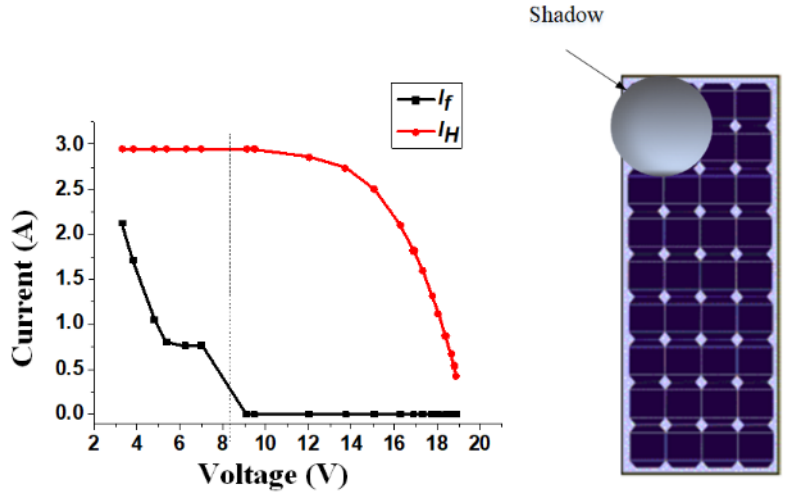

(c)

Fig. 2-4. The types of PV shading. (a) 1st shading test (b) 2nd shading test (c) 3rd shading test [20]

TABLE 2-2 SURFACE TEMPERATURE OF PV PANELS

	1st Test (820 W/m^2, 25 °C)	2nd Test (740 W/m^2, 22 °C)	3rd Test (690 W/m^2, 24 °C)
Unhealthy panel temperature	87.2 °C	33.8 °C	36.0 °C
Healthy panel temperature	44.3 °C	31.7 °C	33.7 °C

Meanwhile, Vasko et al. [21] observed the hot spot situations on PV cells, which were forward biased by a current power supply. After 30 mins heating, the temperature layer became non-uniform, and the hot spots were usually generated adjacent to bus bars. When the forward current of a PV cell exceeds a certain threshold, hot spots will occur under the forward bias conditions. The forward current is higher than the short circuit current in a healthy module because the short circuit current determines the upper limit of the module size before the hot spot formation becomes prohibitive. At the beginning of the electrical and temperature measurements, the voltage on the power supply was slightly different. Besides the formation of hot spots, the low-temperature transient is also caused by the initial heating and capacitive processes. With the appearance of the hot spots, the PV output voltage remained virtually the same, and the voltage and temperature of the hot spot were linearly interrelated. Assuming that all the healthy PV modules in a PV array have identical parameters concerning effective solar illumination intensity S (kW/m^2), ambient temperature T_a (°C), and total heat exchange coefficient U_{pv} (W/m^2·K). Fault diagnosis could be achieved based on Eq. (2.3), which is derived from (2.1) and (2.2). When the module faces a fault, the calculated U_{pv} will be different from that of a healthy module [19].

$$S=V\cdot I+U_{pv}A_m(T_m-T_a) \tag{2.1}$$

$$T_a=\frac{[\frac{I_{mpp}V_{mpp}}{\eta_e-\mu(T_m-T_{ref})}-I_f\cdot V_f)]T_H-[\frac{I_{mpp}V_{mpp}}{\eta_e-\mu(T_m-T_{ref})}-I_{mpp}V_{mpp}]T_H^{'}}{I_{mpp}V_{mpp}-I_f\cdot V_f} \tag{2.2}$$

$$U_{pv}=\frac{S-E}{A_m(T_m-T_a)} \tag{2.3}$$

where T_m is the PV module temperature (°C); T_H is the healthy PV module temperature (°C); $T_{H'}$ is the faulty PV module temperature (°C); A_m is the PV module area (m^2); E presents the electrical output power of the PV module (W); I_f is the current of the healthy module in fault string (A); V_f is the voltage of the healthy module in fault string (V); T_{ref} is the reference temperature 25 °C; V_{mpp} and I_{mpp} are the voltage (V) and current (A) reached at the maximum power point, respectively; η_e is the efficiency of the PV module at certain T_m. For a silicon PV module, the efficient temperature coefficient is μ=0.05%/°C.

In general, aging is accelerated if the PV panel is overheated over a long time. In addition, studies in [20] and [22] showed that when the solar irradiance is greater than 800 W/m^2, the temperature difference between the maximum temperature of the hot spot and the average temperature of the module is about 10 °C. If fewer than 5% of modules have a temperature difference of more than

10 °C, the PV array's power output remains stable. Therefore, even if there are partial shades and PV cell performance defects, the overheating part of the PV cell is not the load necessarily, and the hot spot effect may not occur. Even if a hot spot effect occurs, its severity is also related to multiple factors. Since the hot spot effect is caused by a short-circuited PV cell, the current of the PV string produces a reverse bias. To avoid excessive reverse bias, current crystalline silicon components generally have two or three diodes in parallel to prevent hot spots in PV cells.

2.2.2 Cable aging effect

An arc is the phenomenon of glow discharge produced by the inter-electrode electromotive force breakdown medium. Circuit and device damages are both likely to cause an arc failure. Once a DC arc occurs, PV panels will have a high probability of burning. As is shown in Fig. 2-5, the arc failures of the PV system are divided into three types: series arc fault, parallel arc fault, and ground arc fault [22]. The series arc occurs mainly due to loose device interfaces, resulting in a small spacing and current breakdown spacing. The parallel arcs usually occur between phase and neutral lines, as well as between phase lines because of the broken line insulation. The ground arc refers to the arc current flowing from a live conductor into the earth, which is usually caused by the failure of insulation in the high-voltage phase line.

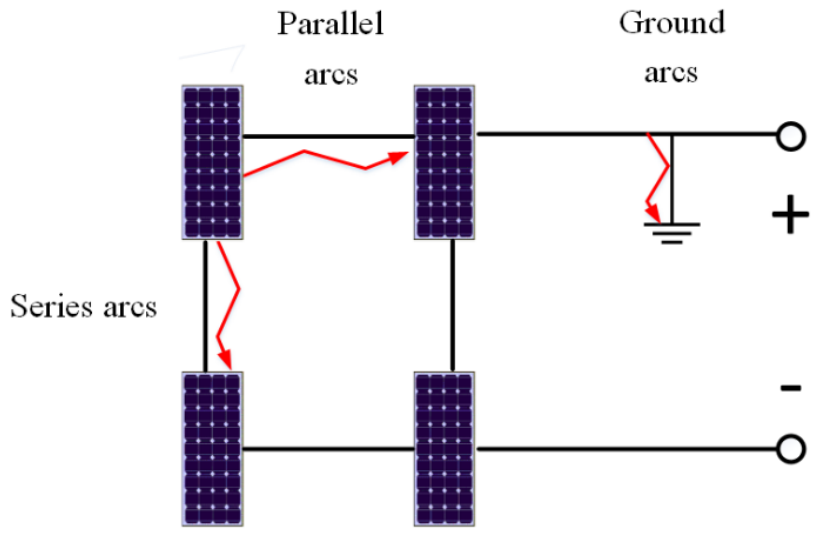

Fig. 2-5. Three types of PV arc failures

Some researchers have observed the significant damages of PV panel fire accidents through experiments and proposed the corresponding protection methods to prevent such accidents. Liao et al. [7] compared the four burning conditions of single-sided PV panels with the irradiance of 15, 20, 30, and 40 kW/m^2, respectively. The experiment setup is shown in Fig. 2-6. A high-power bulb is used as a predicted source to illuminate the front of PV panel *A*, and at this time, the natural

combustion scenario of the PV panel is simulated. Then, PV panel *B* is ignited, and the heat transfer phenomenon of the adjacent PV panel is simulated. Finally, make the back of the *C* PV panel face up, simulating the scenario that the PV panel is ignited by the flame underneath it when an arc fault fire accident occurs. According to the experimental results, at 15 kW/m^2 irradiance, the solar panel was on fire in 200s, but at 40 kW/m^2 irradiance, the solar panel was on fire in 25s. The PV panel is prone to fire accidents when the irradiance exceeds 26 kW/m^2. This is a critical environmental condition as it takes shorter than 50s to cause a fire accident [23]. In [24-25], when setting 10~80 kW/m^2 of applied radiation intensity to simulate firing the flame radiant heat flow, the heat flux on the surface of the sample can be up to 70 kW/m^2 [26]. In the pre-experiment, it was found that the radiant heat flow of 30~40 kW/m^2 can ignite the sample and be safe and controllable. Theoretically, the waste produced after the complete combustion of PV panels is carbon dioxide and water. However, because PET decays during combustion, its chemical bonds are randomly reorganized. The carbon group of the PET molecular chain on the oxygen atom first attracts the hydrogen atom, and then the ester bond is broken down into acids, and vinyl esters transitioned through the six-member rings state, and these cracked products are formed after some secondary processes [7]. Therefore, the decomposition products of PET combustion include CO, CO_2, acetaldehyde, aromatic acids, and vinyl esters. Besides, outdoor oxidation is the most significant problem of ethylene-vinyl acetate film, which is caused by ultraviolet rays and humid hot O_2. Therefore, HF, HCL, SO_2, HCN, and other flammable and toxic gases are generated after the final reaction. Among them, the hydrogen produced by HF or HCL causes secondary damages to PV panels.

The relationship between the time of the fire propagation and the radiation heat flow was obtained, which is $t^{-0.5} \propto q_e^n$ as shown in (2.4) [27]. Besides, the fire caused by the arc fault from TPT is the membrane of the backboard of a PV module. The fire starts rapidly and becomes more intense from the membrane.

$$\frac{1}{\sqrt{t}} = \frac{1}{\sqrt{\pi}} \frac{2q_e^n}{\sqrt{k\rho c(T - T_0)}} \tag{2.4}$$

where t is the ignition time (s), q_e^n is the heat flux (W/m^2), k is thermal diffusivity (W/m·K), ρ is the air density (kg/m^3), c is specific heat capacity (J/kg·K), T is the thermal degree (°C) and T_0 is the reference thermal degree (°C).

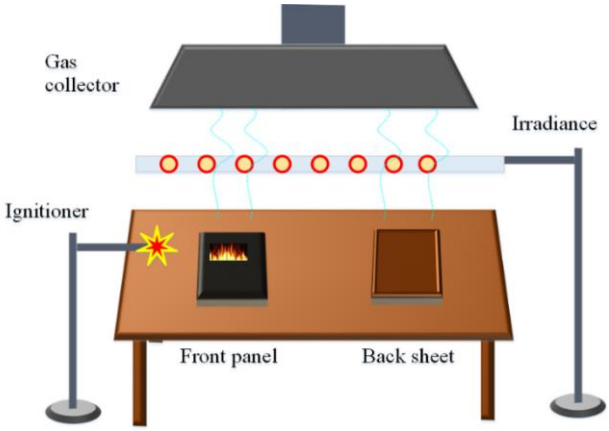

Fig. 2-6. Experimental setup for simulating a fire accident of solar panels

Moreover, the increase of resistance, heating or arcing causes the components to burn out, resulting in a fire. If any of the joints is loose, it may cause a DC arc and consequently a fire [28-29]. If the connector is not wrapped and protected properly to prevent infiltration of sand and dust, the contact resistance of the connector will increase. When the ground wire is not connected, the equipment such as the combiner box lacks effective ground protection. Once there is a virtual connection or a lightning strike, it will cause a short circuit to the ground, which not only degrades the power generation efficiency but also causes serious consequences such as burning of the combiner box. As shown in Fig. 2-7, explosion accidents during the combustion period in PV arrays have a large impact on the safety of operation and maintenance personnel. The explosion mainly comes from the IGBTs and capacitors inside the inverter [30]. The power of a capacitor explosion can penetrate a 2 mm thick steel plate. The possible reasons for the destruction of the combiner box and DC cabinet include unreliable grounding, low cable insulation resistance, bad connector contact, and wiring disorders, etc. [31].

Fig. 2-7. Damaged combiner box by fire [32]

2.2.3 Other conditions

PV modules may also suffer from physical damages. For instance, the cracks of PV modules are caused by pressure. If the welding area of the module is too small, it will easily cause the panel to rupture over a long time. Cracking is the main cause of PV module faults. These cracks are usually not visible to naked eyes and can only be detected through specific testing methods. All PV modules must have certain degrees of pressure resistance to prevent them from being crushed. The quality of material (the choice of glass) and the manufacturing process are the main determinants of the PV module quality. The main factors for the solar panel breakage are environmental conditions, construction, and installation method.

The low vacuuming temperature and foreign matter that enters the crack will generate bubbles, which will affect delamination and seriously cause the module to be completely scrapped, as shown in Fig. 2-8. Component delamination is a serious problem because it allows moisture to penetrate, which will lead to catastrophic failure. At this point, the broken components on the panel need to be replaced. When moisture penetrates the protective layer of the solar module and contacts within the internal circuit, it seriously accelerates the degradation process of a PV module, which eventually leads to catastrophic consequences for the module and the entire PV system [33]. Gluing is caused by the products and materials with poor quality. Over time, the backplane sometimes turns yellow or brown. This is a chemical reaction between the inferior materials and sunlight. Once it begins to change color, ethylene-vinyl acetate will continue to change from its original state, inevitably causing damage to the material [34].

Without good drainage measures on the roof-top, it is easy to cause water accumulation throughout the year. It not only leads to a decrease in PV efficiency but also causes the aging and corrosion of cables, which may lead to fire accidents. For a ground PV array, the impacts of rainwater may cause soil erosion, landslides, etc., causing serious damages to the PV panels [35].

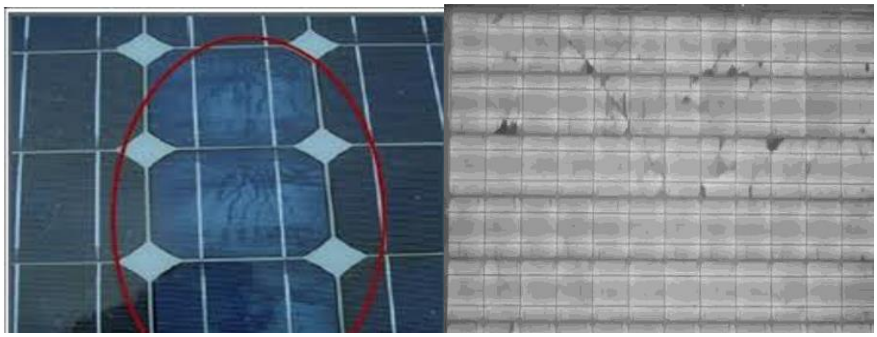

Fig. 2-8. PV module crack [36]

The quality of solar panels must be guaranteed by proper regulations. PV modules have to pass the test of UL 61730-2 “PV Module Safety Assessment Part 2: Test Requirements” [37], with a

fire rating of C (basic fire-proof rating). The components installed on buildings should at least reach the rating of C, and the price of PV modules with different fire-proof ratings varies significantly. Components installed on existing roofs should be subjected to barrier tests and flame spread tests. Components used for roofing materials should be subjected to other subsequent test materials specified in UL 790 “Standard for Standard Test Methods for Fire Tests of Roof Coverings” [38]. There is no international standard for the combustion performance testing methods and judgment rules of modules on different buildings. The industry standard JG/T 492-2016 “General Technical Requirements for Building Photovoltaic Modules” [39] stipulates that PV modules should meet the flammability rating requirements of building materials or building modules in alternative locations and meet the requirements of GB8624 “Combustion Performance” [40]. Relevant regulations on building materials, products, and their product classification, the fire resistance test methods, and measurement rules need to comply with the provisions of GB15763.1 “Building Safety Glass Part 1: Fireproof Glass”, GB/T 12513 “Fire-resistant test method for glass-encrusted components” and GB/T 9978.1 “Fire resistance test method of building components” [41-43].

To sum up, based on the above-mentioned PV production and installation standards, it can be found that the fire safety of PV-building integration is related to the design of PV modules and certification of the PV façade elements. The combination of good quality PV modules with a design-safe PV system can solve many safety issues observed so far.

2.3 Solutions to PV Fire Accidents

Depending on different fire-causing factors in the PV array, this section summarizes existing different solutions for different factors. Existing approaches to avoiding solar PV fire accidents are mainly preventive actions, which are shown in Fig. 2-9. The preventive actions include array recombination and detection algorithm research. The studies [44-54] illustrate the reconfiguration of PV modules or PV arrays, and the studies [55-82] introduce some algorithms to detect the faulty PV modules.

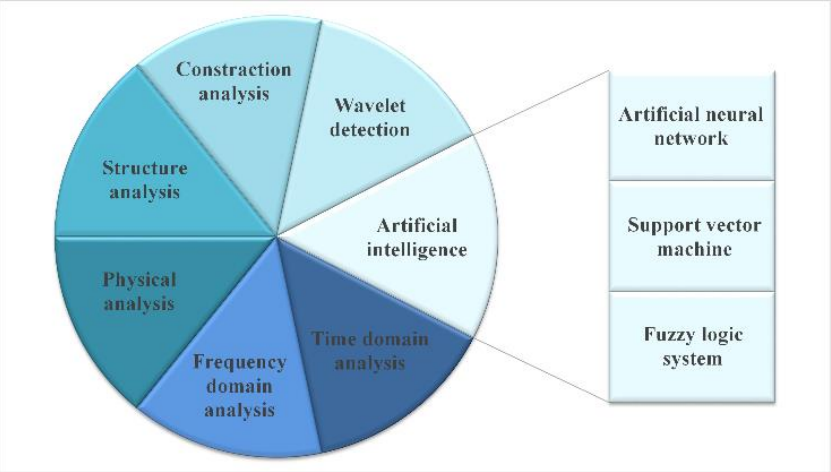

Fig. 2-9. Detection methods for PV fires accidents

2.3.1 Preventive maintenance actions in PV arrays

In PV arrays, shades and dust accumulations are unavoidable, which are also the biggest threats to the safety of PV arrays. Therefore, some preventive maintenance actions such as conducting a periodical cleaning can be very effective in slowing the aging process of PV components and mitigating the hot spot effect.

2.3.1.1 Construction analysis

There are currently two styles of solar panel installation: ground-mounted and roof-top mounted. The surrounding environmental conditions, equipment conditions, and temperature changes of the project location need to be concerned for the ground-mounted PV arrays [40]. Due to the influence of turbulent kinetic energy (TKE) among the modules, the soiling on the surface of the module must be uneven, resulting in the hot-spot effect and PV module fire accidents. It is necessary to establish a flexible inspection and cleaning mechanism or use a data collection system to decide whether unplanned maintenance is necessary to reduce the risk of fire in different environments. However, if the distance between any two PV panels in the array is too far or too close, the generation capacity of a PV array will be reduced. As shown in Fig. 2-10, the spacing D between two PV panels should be large enough to avoid the shading effect, which is selected according to latitude, time angle, etc. The latitude angle (φ) of the winter solstice is -23.45 °, and the time angle (ω) corresponding to 9:00 am is 45 ° [45-46]. In this case, not only the optimal photoelectric conversion efficiency can be guaranteed, but also the TKE value can be obtained to avoid dust deposition. Therefore, calculating the distance between two panels according to (2.5) can obtain the most suitable distance between PV panels.

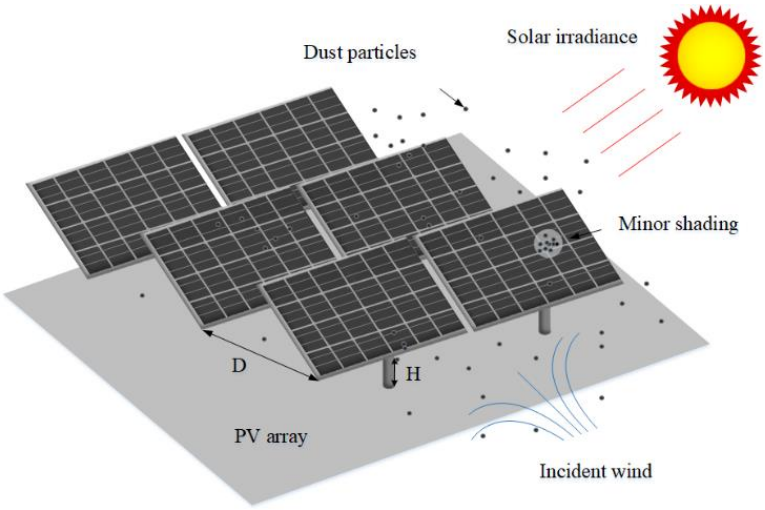

Fig. 2-10. Dust deposition on a PV array

$$D = \frac{\cos A \times H}{\tan[\sin^{(-1)}(\sin\phi\sin\delta + \cos\phi\cos\delta\cos\omega)]} \tag{2.5}$$

where D is the distance between obstacles (m), A is the azimuth of the sun (°), φ represents the latitude (°), δ means the declination (°), ω is the time angle (°) and H is the PV array height difference (m).

Considering that the roof-top buildings are in close contact with people, the following factors need to be noted: 1) whether personnel injuries caused by the high voltage of the DC line in the event of a fire can be avoided by string arrangement design or equipment technology improvement; 2) plan the location of the roof upper and lower channels and electrical equipment according to the meteorological data of the project location to reduce the time of power-off; Enough firefighting passages are provided to ensure rapid passage during a rescue. At the same time, the roof array distribution map is marked at the entrance of the bottom of the passage, and the opening and closing points of the power lines are marked. The marking should be easy to identify and well-marked to prevent fires. It can be cut off quickly; 3) the module arrangement includes both horizontal and vertical arrangements, and the corresponding purlin arrangement also has two directions. When the module is arranged horizontally, the purlins are arranged vertically, as shown in Fig. 2-11. In this case, due to the chimney effect, the fire spreads faster than arrays with vertically arranged components [47-49].

Overall, strictly controlling the entry threshold of construction units, paying attention to environmental risks during the initial site selection, standardizing the cable connection construction, and establishing a reasonable operation and maintenance system and cycle according to the actual conditions of different projects can effectively reduce potential dangers. By improving

the technology and considering the design and training of the roof owner and local fire department, the impact of the fire can be reduced. That is to say, through comprehensive management before, during, and after the accident, the loss can be minimized or avoided [50].

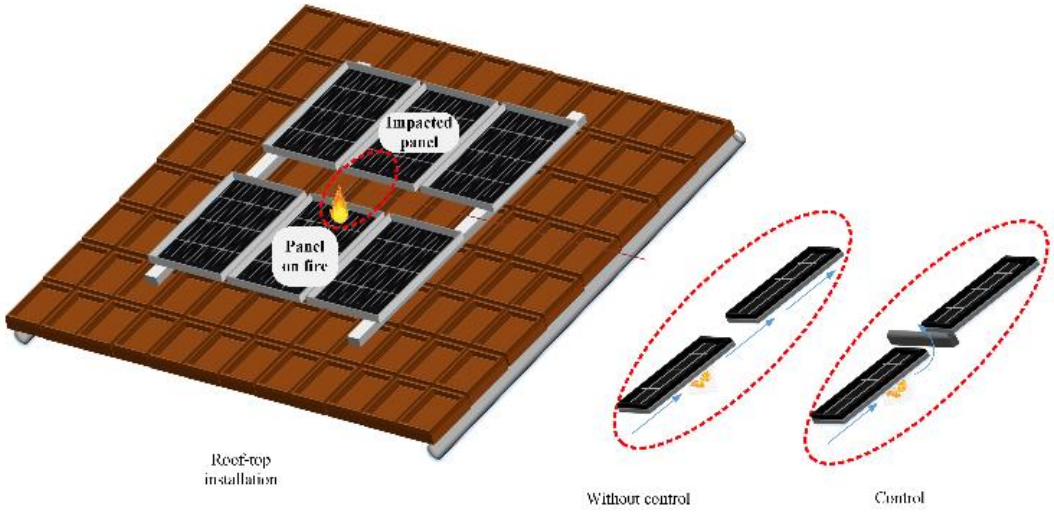

Fig. 2-11. Solution to PV fires on roof-top PV array

The impact of dust reduction on PV panels is enormous, both for the ground and roof-top mounted PV arrays. Formula (2.6) is used to estimate dust flux around the PV array, and CFD simulation can accurately calculate the annual dust drop and dust distribution of a PV array, and thus a suitable cleaning cycle and cleaning method for the local PV array can be obtained. Proper cleaning can effectively reduce the fire probability of PV arrays.

$$F_D = aEc\frac{\rho_\alpha}{g}u_*^3\left(1+\frac{\frac{u_*}{\kappa}In(z/z_0)}{u_*}\right)\left(1-\frac{(\frac{u_*}{\kappa}In(z/z_0))^2}{u_*^2}\right) \tag{2.6}$$

where E is the erosion factor, α is the sand blasting efficiency, c is the empirical proportionality constant, g is the gravitational acceleration (m/s^2) , ρ_α is the air density (kg/m^3), u^* is the friction velocity (m/s). κ is a constant obtained empirically (about 0.35 for turbulent flow), and z_0 is the roughness length (m).

2.3.1.2 Structure analysis

Hot spots occur when the PV module is partially blocked, and part of the solar cell string becomes a reverse bias and dissipates energy in the form of heat. If the solar cell consumes more power than the maximum power of the PV cell, which maintains the maximum power under hot spot

conditions, the PV cell will be completely damaged and open-circuited. To protect the series PV cell, the bypass diodes are added to the PV cell string [51].

K. Kim proposed the first hot-spot mitigation technique that uses bypass diodes to reconfigure PV modules [52]. The model structure is shown in Fig. 2-12 (a). In the research, K. Kim shaded 1 of a 24-cell string and found that a bypass diode imposes 0.5 V across the substring. However, there are still currents passing through the shaded PV cell. Actually, the bypass diode can be treated as a load, which does not generate power. By using Kirchhoff's Voltage Law, the reverse voltage in the circuit can be described in Eq. (2.7). Once a hot spot is detected, there are two approaches to mitigating the potential risks. For short PV string (2~3 cells), the traditional bypass diodes are more effective in reducing the probability of hot spots effect. For long PV string, a low reverse-breakdown PV cell limits the power dissipation in the hot-spotting time. It is an effective prevention method if the power dissipation can be managed without damaging the cell.

$$V_R = (N-1)V_F + V_D \tag{2.7}$$

where V_R is reverse voltage (V), V_F is voltage drop (V), and V_D is the diode voltage (V). (N-1) means the voltage drop from node 1 to node N.

The advantage of this technique is reducing the temperature of solar cells in hot spots. Meanwhile, the probability of causing hot spots is also reduced for longer PV strings.

Based on the traditional bypass diode, S. Daliento proposed a modified bypass diode reconfiguration, namely, an ON-OFF MOSFET for PV modules in a hot-spot scenario [53], which is shown in Fig. 2-12 (b). This method is applicable to any PV module, which composes of series-connected cells. When the PV panel is partially shaded, this solution can significantly reduce the hot spot temperature by transferring the reverse voltage of a normal PV cell to the series-connected MOSFET in each sub-panel. To conclude, when the panel cell is not shaded, the gate-source voltage (V_{gs}) approximately equals the $V_{subpanel}$. Conversely, the reverse voltage forces the V_{gs} and V_{DS} to degrade, hence blocking, or partially blocking I_{DS}, resulting in the increase of V_{DS}. Finally, V_{DS} can be subtracted from the total reverse voltage due to the existence of the MOSFET. However, this topology has some drawbacks, such as the possible mismatch between the $V_{subpanel}$ and the uncontrolled V_{gs}, and the breakdown risk of the MOSFET. The formula is shown below:

$$V_R = (N-1)V_F + V_D - V_{DS} \tag{2.8}$$

where V_{DS} is the MOSFET drain–source voltage drop (V).

This method was verified by testing the reduction of hot spots temperature of polycrystalline silicon and monocrystalline silicon PV modules, which cooled down to about 20 °C and 24 °C, respectively.

Based on the single ON-OFF MOSFET switch circuit, M. Dhimish proposed a double MOSFET switch circuit, which is more effective in mitigating the hot spots effect [54]. The model is shown in Fig. 2-12 (c). Switch 1 is connected in series with the PV cells, and the general state is "on." When a hot spot situation occurs, switch 1 will open to further alleviate the hot spot effect. Switch 2 is in parallel connection with the PV cells, and the general state is "off." When the PV string is open, it will open to circulate current. To ensure the health of the PV module, switch 2 is controlled by the 16F877A microcontroller and activated twice every three hours. Because M. Dhimish found that three hours is the maximum allowable duration before the hot spot reappears in the PV cells, and the number of activations is determined by thermal image analysis. As for the 16F877A, it is a microcontroller-based system that prevents hot-spot operation using open-circuit PV modules. This method not only reduces the heat spot temperature by 17 °C but also increases the output power by 3.8%.

Simultaneously, P. Guerriero proposed a new bypass diode circuit, which is an evolution circuit from S. Daliento [49]. The diagram is shown in Fig. 2-12 (d) [55]. In the circuit, the drain-source voltage drop of MOSFET *M1* supplies power to the TLC555 digital oscillator, and its output voltage drives MOSFET *M2*. Therefore, as long as *M1* works normally, the oscillator is turned off, and its output is low, and *M2* is also turned off. When a part of the PV cells is blocked, the drain–source voltage drop of *M1* increases and the oscillator turns on and begins to provide an output signal that alternates between high and low. The output signal remains high for approximately 97% of the time. During this time interval, *M2* is on, so *M1* remains off. Conversely, if there is no longer partial occlusion, *M1* is turned on, its drain–source voltage drop is decreased, and the oscillator is turned off, returning to normal operating conditions.

This method can reduce the hot spot temperature to 50 °C and increase the output power by 8% in a shadow-shaded scenario. Different from others, this solution addresses the rising temperature of shaded cells completely. Meanwhile, the oscillator will not generate more power on bypass events since the oscillator sleeps in the rest time.

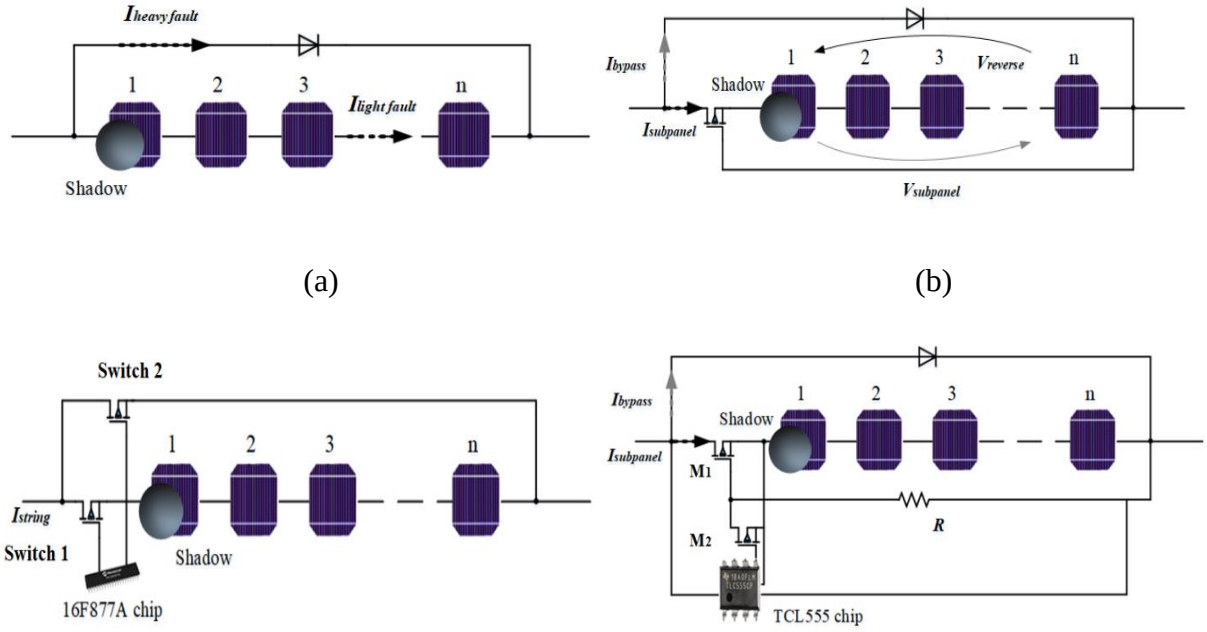

Fig. 2-12. Reconfiguration of PV string. (a) bypass diode circuit (b) ON-OFF MOSFET circuit (c) 16F977A microcontroller circuit (d) TCL555 microcontroller circuit

By changing the structure of the PV string, as well as by some controllers, the probability of hot-spot effect can be effectively reduced. This method not only reduces the risk of a PV array but also increases the power of PV output [56].

2.3.2 Fault diagnosis

In 2011, the US Insurer Laboratory (UL) launched the UL Standard 1699B draft [57], which is the DC arc detection standard of circuit safety outline of DC arc fault protection for the PV systems [58]. At present, numerous methods can detect the arc fault of PV systems: physical analysis (clustering method) [59-62], Fast Fourier Transform (frequency domain analysis) [63-67], time-domain analysis [68-71], wavelet detection (multi-resolution analysis) [72-81], and Artificial Intelligence method (neural networks, support vector machines, fuzzy logic systems, etc.) [82-90].

2.3.2.1 Physical analysis

In the event of an arc failure, the heat, arc, noise, or electromagnetic signals will be emitted. The physical analysis is based on the physical properties of sound, light, and radiation are detected by the cluster method. As for the famous and widely used physics-based model, the Myer arc model

is suitable for low current arcs [59], which assumes that thermal causes power loss and the formula is shown below:

$$\frac{1}{g}\frac{dg}{dt} = \frac{1}{\tau}\left(\frac{i_{arc}^2}{P} - 1\right) \tag{2.9}$$

where g is arc conductance (S), i_{arc} is arc current (A), P is the static cooling power (W), and τ is the arc time constant determined empirically (s).

In addition, Peng et al. used fuzzy logic to indicate clustering to detect arc failure [60]. The maximum mold value of the electromagnetic radiation signal of the fault arc after noise reduction is selected as the fault criterion. In [61], the Hilbert antenna is used to measure the electromagnetic radiation signal of the DC arc, the frequency of the electromagnetic radiation signal, the pulse interval, and the pulse cluster duration as the basis for the failure. Physical-based detection methods install devices in local locations in the system, making it easier to locate fault locations [62]. However, because these models involve many parameters, the operation is complex and is not easy to be implemented.

2.3.2.2 Fast Fourier transform

Fourier Transform is a classical frequency domain-based method, and it is recommended to carry out fault detection in the frequency band of 1 to 100 kHz [63-64]. The time of the Fast Fourier Transform (FFT) detection method is shorter than 16 ms. It effectively disconnects the arc from the inverter in the DC microgrid. While this algorithm may not affect the converter startup. In this case, the time domain changes dramatically, and the size of the high-frequency content in the frequency domain increases like an arc failure, leading to unnecessary tripping [65-66].

The FFT transformation of single current mutation and electromagnetic radiation waveform is carried out, and its spectral characteristics are analyzed. The spectral characteristics of current and electromagnetic radiation signals are similar, with the highest frequency of 13 MHz. The electromagnetic radiation field is proportional to the current rise rate. At the beginning of the current steep rise edge, the inductor of the arc is close to zero. The estimated maximum amplitude of arc electromagnetic radiation spectrum is derived based on (2.10) [67]:

$$f_0 = \frac{1}{2\pi\rho\varepsilon} \tag{2.10}$$

where ε is the dielectric constant of the air (F/m), and ρ is the arc resistivity (kg/m^3).

According to (2.8), the frequency with the largest amplitude in the electromagnetic radiation spectrum is only related to the arc resistance and the dielectric constant in the air. The resistivity of arcs generated by different inter-polar distances and electrode diameters may vary, and the frequency of electromagnetic radiation in DC arcs may be different. Therefore, the pulse interval, characteristic frequency, and duration of the arc electromagnetic radiation signal can detect DC arc failure as feature parameters.

2.3.2.3 Time domain analysis

The advantage of time-domain analysis is intuitive and accurate. The time-domain representation of the system output can be obtained from differential equations or transfer functions. In [68-69], the accuracy rate of fault detection in a PV module detected by the Minimum Covariance Determinant (MCD) estimator under STC is 98%, and the false alarm rate is 0.01%. This method is to operate the voltage and current of different PV modules into the MCD estimator at the same time instant. Then, the distribution of the I-V curve to the centerline of each PV module can be used to detect arc faults. The MCD estimator can be determined as (2.11).

$$\alpha = \frac{med_i((x_i - \hat{\mu}_S)^T \hat{C}_S^1 (x_i - \hat{\mu}_S))}{m} \tag{2.11}$$

where $\hat{\mu}_S$ and $\hat{C}_S$ are estimates of sample mean and covariance matrix computed using the MCD estimator, and x_i is a data subset.

In [70], Schimpf et al. used the Finite Impulse Response (FIR) estimator to detect the arc fault. The idea of this method is that when the arc detector is integrated into the PV module, the detector can only measure and monitor the PV current and the PV voltage. Due to the need of shunt resistors, Hall sensors, or current transformers, the only signal used as the arc detector input is the PV voltage. The arc voltages measured on the PV module varies significantly according to their positions in the system. The operation of FIR estimator fault detection is that first passing the input signal through a bandpass filter whose cut-off frequencies are 1 kHz and 7.5 kHz. The estimator then compares the current signal value to the previous value, and when the difference is 0, the system is fault-free.

In [71], Yao et al. found that the selection of time window length will impact the current waveform pattern. The research shows that time-domain analysis, although simple, is very effective in identifying arc failures because it has long enough time to ensure the randomness of the test.

2.3.2.4 Wavelet analysis

At present, wavelet analysis is the mainstream detection method, which is a gradually multi-scale refinement of signal functions through telescopic translation operation, and finally reach the high-frequency time segmentation and low-frequency subdivision, so as to focus on any detail of the signal [72-75]. According to the fault signal, it sets the motion threshold of the fault alarm device in a normal state and in a different value range, thus solving the difficult problem of Fourier transformation. Wu et al. [76] selected the db4 wavelet for wavelet decomposition, and they selected the energy value of the high-frequency wavelet component as the fault standard, and the reliable value between the normal state and the fault state is used as the fault alarm threshold. Meanwhile, Lu et al. [77] selected the standard deviation as the characters in the time domain, and they took the energy of each band after the db5 wavelet decomposition as the frequency domain feature. Then they constructed the feature plane, and divided the critical fault line within the feature plane to detect the arc. The maximum signal and wave detail are determined by experiments. The variance and model values of the numbers are the three time-frequency domain standards, and time domain-based measurements are proposed. Mix the condition with the arc fault of the frequency domain, and the judgment of this method has a single method with high precision and reliability, which further reduces the error rate and suppression rate of the detection method [78]. The accuracy of wavelet decomposition fault detection is 100% [71][79].

According to the basic principle of the time-domain emission method [80], the relative position of the fault point and the measuring point can be calculated as:

$$dis = \frac{v\tau}{2} \tag{2.12}$$

where v is the wave speed in the cable (m/s); τ is the signal of time-delay value in the fault.

For a row wave, if the distance of propagation is L along the cable within a cycle time T, the propagation speed of the wave is v, then, it can be obtained that:

$$v = \frac{L}{T} \tag{2.13}$$

When the transmission line loss is very small or the test signal is high-frequency, the wave speed can be derived as:

$$v = \frac{2\pi f}{\beta} = \frac{\omega}{\beta} = \frac{\omega}{\omega\sqrt{LC}} = \frac{1}{\sqrt{L_0 C_0}} \approx \frac{c}{\sqrt{\mu_r \varepsilon_r}} \tag{2.14}$$

where c is the speed of light, which is 3 x 10^8 m/s; μ_r is the relative magnetic guide coefficient of the medium around the cable at high frequencies; ε_r is the relative dielectric constant of the medium around the cable at high frequencies.

According to (2.14), the transmission speed of the pulse wave in the cable is not related to the structure, length, and conductor material. It only depends on the relative magnetic conductivity and relative dielectric constant of the cable insulated medium. For the cables made of different conductor materials, the insulation medium is the same, and the signal travels at the same speed inside it.

This method fills the blank of arc fault detection and positioning on the DC bus in the PV system and effectively prevents accidents caused by arc failure. Because the detection signal of this method has sharp self-correlation, it can have a good anti-jamming ability and high accuracy in the on-line detection and positioning of DC bus arc fault [81].

2.3.2.5 Artificial intelligence method

In recent years, artificial neural networks (ANN), support vector machines (SVM), fuzzy logic, and other intelligence algorithms have replaced thresholds to decide whether there is an arc fault.

The ANN aims to obtain the model through learning and use the model to predict the desired target value. In the field of arc detection, the position of DC arc can be detected by using the data of the neural network. He et al. in [82] used an RBF neural network to determine if there is an arc fault, but it is easy to result in local optimization and slow training. The study [83] used a genetic algorithm optimized BP neural network to judge arc fault. The ANN method is fast and accurate for arc detection [84].

The arc detection neural network model is shown in Fig. 2-13, using a three-tier structure [85], where P is the input matrix; i, j, and k represent the number of nodes at each layer respectively; w_{ij} is the weight between the implied layer j node and the output layer i node, and w_{jk} is the weight between the node k of the output layer and the node j of the implied layer. The implied layer activation function selects the S-type activation function, and the output layer activation function selects the linear activation function.

(a) Input layer: Input layer nodes are related to the number of input data. The input to the model is the 12th to 31st harmonics after the FFT, so the junction of the input layer is 20.

(b) Implied layer: Implied layer nodes are not fixed and can be adjusted as needed. Currently, there is no universal way to determine the number of implied layer nodes. If the number of nodes is too small, the network performance is poor or cannot be trained. If there are too many selections, although the error can be reduced, it will increase the network training time, making it easy to fall into the local minimum point and not able to reach the optimal solution. The determination of the number of implied layer nodes is obtained by formula (2.15) [86].

(c) Output layer: The output layer only needs one node, where the output 0 and 1 respectively represent the arc-free and arc-less.

$$n = \sqrt{n_1 + n_0} + \beta \tag{2.15}$$

where n is the implied layer junction, n_1 is the input layer junction, n_0 is the output node, and β is the constant between 1 and 10.

According to (2.16) and combined with the results of a large number of experiments, it is found that the training effect is the best when the number of implied layer node points is 14.

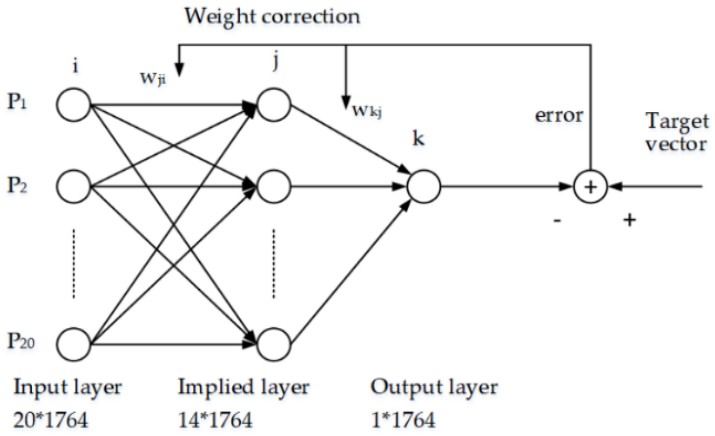

Fig. 2-13. Arc detection neural network model [85]

In addition, the studies [87] and [88] use an SVM algorithm to extract the mean current and high-frequency components from the time-frequency domain. Fault criteria are used to train the model, and the obtained model can be used to indicate whether an arc fault occurs.

SVM is a better-supervised learning algorithm. This algorithm is used to solve the separation hyperplane problem that can divide the training data set normally and has a very large geometric

interval. As shown in Fig. 2-14, all of the “circle” means training data. Among them, the red circle is the support-vector. "Wx+b=0" means the separation hyperplane. Actually, there are countless hyperplanes corresponding to linearly separable data sets. Among them, the separation hyperplane with the largest geometric interval is unique. Compared with ANN, SVM searches the global minimum data during training, while ANN will only search the local minimum data. And the performance of SVM is highly related to the quality of training data.

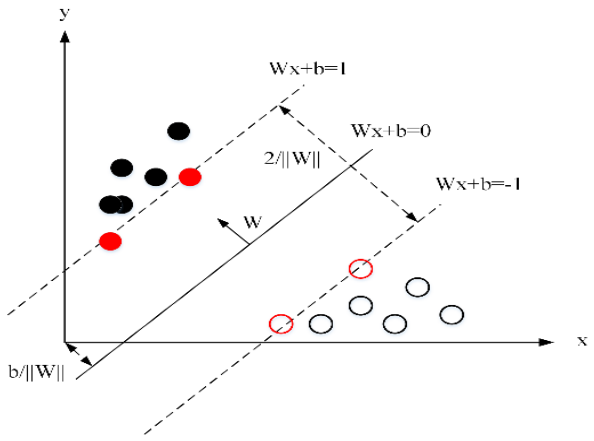

Fig. 2-14. A diagram of SVM trained samples [88]

In [89] and [90], the authors used a fuzzy logic system to detect the arc fault in the PV array. The accuracy of this method is up to 98.8%. The operation of the arc detection system based on fuzzy logic is: First, input the initial signal to the fuzzification process. Then, use the predefined rules to classify arc faults and normal operation. It should be mentioned that the rules in fuzzy systems are designed based on fault modes and mechanisms.

2.3.3. Discussion

The method of fire prevention and detection of PV Arrays can be summarized as the optimal distance method (ground-mounted PV array), obstacle-adding method (roof-top mounted PV array), and reconfiguration of PV components, physical analysis, frequency domain analysis, time-domain analysis, wavelet detection, and the artificial intelligence algorithm. The advantages and disadvantages of these methods are shown in Table 2-3. Due to the increasing fault cases, there are many databases that can be used in the future. Therefore, artificial intelligence methods will be concerned popular in the future.

Based on these methods, isolation devices can be added to PV arrays with fire-proof materials, and the alarm system can be set up according to the intelligent algorithm to identify the DC arc

failure, thus minimizing the probability of a PV fire. In addition, the safety training of firefighters is essential due to the large number of toxic gases produced by PV combustion [91].

TABLE 2-3 FIRE PROOF SOLUTION OF PV MODULES

Method	Adopted technique	Advantage	Disadvantage	Accuracy	Reference
Distance of each PV panel (ground mounted PV modules)	Design the optimal spacing between each panel	Avoid the hot-spot effect while ensuring maximum power capacity of the PV array	Error in the amount of dust accumulation on the surface of PV panels	Not mention	[40][45-46]
Obstacle of each PV panel (roof-top mounted PV modules)	The baffle is used to block the air flow between each panel	Blocking the airflow between PV panels reduces the flame burn trend	Increased roof load, and the rescue of firefighters made it more difficult	Not mention	[47-50]
Structure analysis	Add bypass diode or MOSFET in the circuit	Reducing hot-spot effect and improve the power efficiency	Increased cost of PV modules	Not mention	[51-55]
Physical analysis	Detect arc faults through physical	High accuracy on small collections of data with less than 200 data objects	These models involve many parameters, the operation is complex and is not easy to implement in simulation	High	[59-62]

Frequency domain analysis	Detect arc faults by using FFT in the frequency domain	Fast and high universal	This algorithm may not work properly at the inverter or converter startup. It is easily to trip.	Below 90%	[84]
Time domain analysis	Detect arc faults through estimators in the time domain	Intuitive, high accuracy, and easy to operate	Constrained by time window	98%	[68-69]
Wavelet detection	Detect the arc faults through the wavelet at time-frequency domain	Effective and directly	Limited by vibration diagnostic and analytical instruments, resolution, and analysis software functions.	100%	[71][79]
Artificial intelligence detection	Detect the position of DC arc by using ANN, SVM, and fuzzy logic system.	High accuracy, easy, and convenient	Need a huge data-base	About 99%	[87-88]

2.4 Summary

The safety of PV power generation and PV arrays is receiving increasing attention. Especially, the possibility of fire needs to be reduced and timely maintenance is required. The hot spot effect and aging of PV panels were found responsible in previous fire accidents, which can be caused by the dust density around the PV array, the ambient temperature, and the material structure of the PV array. Preventive solutions to the fire accident can be categorized as solar panel reconfiguration

and fire fault detection algorithms. The advantages of reconfiguration of PV modules include reducing hot spots and improving power efficiency. Meanwhile, the advantage of the fire fault detection algorithm is detecting the fault positions accurately.

In order to reduce the probability of PV fire accidents, there are technical specifications to comply with. Firstly, the PV module needs to pass the UL 790 “Safety Standard for Roofing Material Fire Test” combustion and flame spread test. Secondly, the inverter should be designed without fuses to avoid the fire caused by DC side faults. The internal inverter transformer, PCB board, and other internal components prone to high temperature should be made of non-combustible or non-combustible materials. Thirdly, the internal components of the junction box, control equipment, and power distribution equipment should be made of non-combustible materials. Fourthly, all cables require flame retardant coating and they should be made of low smoke and low toxicity materials. Fifthly, fire-proof sealing measures should be applied to holes, such as cable inlets and outlets of power distribution equipment in houses, equipment inlet holes, cable inlets and outlets of junction boxes, cable penetration holes, cable trenches, and cable trench interfaces.

In addition to research on the mechanism and prevention of PV fires, it is also necessary to consider fire safety issues of PV-building integration. In order to improve the safety of fire prevention and extinguishing of PV systems, it is basal to conduct fire risk investigation and hazard assessment, and test and evaluate the combustion properties and fire resistance of PV modules. Secondly, considering the impact on building safety, it is advised to conduct a comprehensive risk assessment for potential failure units of PV building integration. Particularly, design fire separation facilities and use fire-proof materials to reduce losses caused by fire accidents. Thirdly, realize the management intelligentization of electrical fire monitoring and early warning, and strengthen the investigation of hidden fire hazards of the equipment. Specifically, the fire prevention and control system should be able to automatically identify and eliminate fire risks. For example, set up an appropriate automatic fire alarm system, intelligent protection against DC arc, and intelligent blocking components. Finally, it is also critical to strengthen the daily fire supervision and management, and regularly hold the fire safety training on PV power generation.

Chapter 3 Time-effective Dust Deposition Analysis of PV Modules Based on Finite Element Simulation for Candidate Site Determination

3.1 Introduction

Adopting solar energy is now the mainstream of the renewable energy industry. However, the dust particles affect the PV power generation efficiency seriously. At present, the output power efficiency of PV panels in standard test conditions (STC, 1000 W/m^2, 25 °C) is decreased by 18%~20.2% due to the dust shading [92-93]. In addition, the dust accumulation also increases the surface temperature that decreases the power generation [94-96]. Meanwhile, the relation between the dust deposition and output power efficiency is analyzed to estimate the soiling management of PV modules. The PV power decreased linearly by 1.7% per g/m^2 [97]. Therefore, in order to maintain the PV power generation for a PV array, the frequency of cleaning is three times a month [98-99]. The soiling management of solar panels not only improves the power generation efficiency but also protects the PV panel from the hot-spot effect. It damages the PV panel, so a reasonable cleaning cycle is necessary, which places great demand on the researches on the dust distribution and deposition on the PV panel surface under different field conditions.

There are currently two methods to detect the impact of dust deposition on PV panels: finite element (FE) simulation and experiment. In [100], Wasim. J et. al. carried out an experiment in Doha, Qatar (STC, PV tilts 22 °) to compare the dust accumulation in each panel, including a two-week observation, a one-month observation, a two-month observation, and a six-month observation, respectively. From [100], the complete data of dust deposition is from 2 months' investigation, which is the most suitable exposure period so far, and the dust accumulates 100 mg/m^2/day. In [97], Rohit. P et. al. summarized some experiments to collect the data on dust accumulation and transmittance. Because the period of experiments generally lasts for between several weeks and one year, which is time-consuming, many other scholars employ FE simulation to discuss the dust deposition and power generation issues. It is hard to quickly analyze the dust flow in a new region where PV farms are going to be constructed. Luke. S et. al. in [101] implemented the prediction of particle accumulation by using computational fluid dynamics discrete phase module (CFD-DPM), where the dust particles can be expressed as a spherical model in the simulation. Based on [101], the authors in [102] created a model in CFD software to calculate

and analyze the impact of dust deposition on PV panels. Meanwhile, in order to analyze the shielding effect of the front panel on the rear panel, Hao. L et. al. also introduced the impacts of dust on PV array in [103] by using the two-dimensional (2D) based FE analysis, and the accuracy of FE simulation was verified in [104].

Nevertheless, although these previous methods provide some good ideas, some shortcomings also exist. Firstly, the research in [101] only focuses on the effects of particles in the airstream but does not systematically introduce the applications that are attached or surrounded by particles, especially for temperature-sensitive objects, such as PV panels. Then, [102] only focused on investigating the influence of dust particle deposit on the PV panels along with a fixed wind direction. Because of the turbulence kinetic energy (TKE), the dust deposition on the surface of the PV panel is non-uniform. Finally, in [103], the same problem occurs when detecting the density of dust accumulation in different parts of each panel in a PV array. However, these studies have only analyzed the situations with the horizontal wind direction and the dust particles distributing around the PV panel and ignored the relationship between dust motion and PV panels, which is also the limitation of a 2D model. However, the influence of wind direction on sand and dust distribution cannot be neglected. Different horizontal wind directions will cause sand and dust to accumulate on different parts of a PV panel, which stimulates a more actual situation. If dust particles are taken into account, the values in the analytical results can be closer to the actual ones [105-107]. Significantly, because of the viscosity and collision of dust particles, the power can reach two peak values. When the wind speed is low enough, the viscous force of dust to PV panels is higher than the collision force, and the dust deposition reaches the critical value, which means the cumulative value of dust under this condition does not change. When the wind speed increases significantly, the viscosity of dust to PV panels is less than the collision force, and the dust deposition reaches the critical value, in which case the cumulative mass no longer changes. This change depends on the TKE value. The dust accumulation not only reduces the photoelectric conversion efficiency but also causes the PV panel to generate heat, which accelerates the aging of PV cells and causes the hot-spot effect. Although the above literature paves the way for studying the dust distribution issue on PV panels, few studies focus on the relationship between PV dust deposition and power generation by using numerical simulation.

This study proposes to predict the dust deposition concerning different wind directions and wind speeds, thus obtaining a specific relationship between the PV output power and dust deposition by using the 3D model in CFD aiming at a typical district (Liverpool, England). CFD is a powerful software that can be used to calculate and express the physical characteristics of fluid motion,

including flow and dust distribution, and temperature. Firstly, this study establishes a physical model in CFD. In terms of the setups, they keep in accordance with the real situations. In detail, according to the data from the local meteorological station, the wind speed in Liverpool is from 4.43 m/s to 6.48 m/s yearly. The particle size is from 10-100 μm in the airstream, and the wind direction always shifts. Therefore, following the wind velocity in Liverpool, this study simulates the effects of wind-dust at 0°, 30°, 45°, 60°, and 90° wind direction on PV panels. Then, in virtue of the CFD simulation results, the influence of dust on PV panels is further discussed, such as temperature and power generation. Finally, in order to verify the data obtained by using CFD, an experiment is conducted on PV panels. The power efficiencies in different situations of dust accumulation are measured. By analyzing the dust accumulation characteristics under different wind directions and wind speeds, the power efficiency can be derived in these environmental conditions. The significance of the research mainly includes: Firstly, the analysis cycle has been greatly shortened in comparison with the experimental method. Moreover, during the simulation process, the turbulent energy between the panels is obtained so that the quantity of dust accumulation of large-scale PV arrays can be predicted. Thirdly, the dust distribution can be observed by changing the wind direction to PV panels, complying with the real conditions.

The structure of this chapter is as follows. Section 3.2 illustrates the methodology to express the relationship between the dust deposition and output power of PV panels. In the CFD simulation, the wind flow can be set as the boundary condition. Meanwhile, the discrete phase is set as the injecting particles. By changing the wind speeds and directions, the shading and temperature on the surface of a PV panel are analyzed. In Section 3.3, the data between dust deposition, temperature, and output voltage are analyzed. Simulation and experiment results are compared, and the uncertainty of simulation is analyzed. Section 3.4 presents the summary.

3.2 Design of Dust Accumulation on PV Modules

As for PV modules, shadings and temperature rise decrease the open-circuit voltage of a PV panel. Therefore, it is necessary to get the local climate information before choosing a location to build a PV station. By using numerical simulation, the data of dust deposition on a PV panel were obtained with respect to different wind speeds and different wind directions in a short time.

Moreover, the accuracy of dust accumulation on the surface of the PV panel was validated by experiments. Finally, the relation between the power generation of PV panels and dust accumulation is analyzed with different volumes of dust particles, which was obtained both by the simulation and experiment. On the one hand, a reasonable cleaning cycle improves power

generation efficiency. Using CFD simulation can help to plan the solar panel cleaning cycle. On the other hand, the simulation is convenient for helping choose the right place to build a PV station.

3.2.1 Boundray conditions of simulation

Initially, a 3D model is established in the CFD simulation environment, where a boundary is set, as shown in Fig. 3-1. The distance between the ground and the bottom of the PV panel is *H*. In order to avoid the boundary effect, the distance between the inlet and a PV panel is set as *5H*, and the distance between a PV panel and the outlet is *9H*. The height of the computation domain is *6H*, and the width of the domain is *10H* [108]. The PV panel used in the simulation has a volume of 300×210×20 mm, which is established as a PV panel (RS PRO). According to [109-111], the optimal tilt angle is set as 56° for the solar panel installation with the maximum power generation.

It is important to analyze the impact of wind direction on PV panels because the wind direction is uncertain in a year. The physical model is built, which is shown in Fig. 3-1. The previous study only introduces a single wind direction facing the PV panel, which is shown in Fig. 3-1 (a), but it cannot represent the universal cases. On the other hand, the proposed method considers the change of wind directions, which is shown in Fig. 3-1 (b).

According to the records from the UK meteorological station, solar irradiance, wind speeds, and wind directions can be obtained in a year. The wind speeds in England dropped from 6.48 m/s to 5.45 m/s from January to March 2019, which is shown in Fig. 3-2 (1 mph= 0.447 m/s). The main wind direction is South-West in this period. Then, from April to September, the wind speeds decreases from 5.45 m/s to 4.43 m/s. In this period, the wind direction is changed to West from South-West. Finally, the wind speed rises from 5.45 m/s to 6.48 m/s from October to December with the wind direction of South-West. Therefore, the chosen wind speeds for simulation are: 4.43 m/s, 4.71 m/s, 5 m/s, 5.22 m/s, 5.45 m/s, 5.73 m/s, 6 m/s, 6.24 m/s, and 6.48 m/s. Over a year in Liverpool, the most frequently encountered wind direction is from North-West to West. Hence, in the simulation, the incoming wind directions are set as 0°, 30°, 45°, 60°, and 90° for the PV panel with respect to the horizontal direction.

In order to avoid the shading effects among PV panels, the space *D* between PV panels should be set as a certain value, which is based on the latitude, time angle, etc. The latitude angle (φ) of the winter solstice is -23.45°, and the corresponding time angle (ω) at 9:00 am is 45°. In this situation, the efficiency of photoelectric conversion is the maximum value in a day. Therefore, according to (3.1) [102], the distance between two panels is 0.43 m, which is the most suitable distance to make

the PV panel absorb the irradiance.

The distance between a PV panel and the ground has a great influence on the eddy current of the wind, so it is necessary to establish a realistic model to investigate this effect. Based on the Reynolds number (*Re*) [108], the Realizable *k-ε* model is selected. The Realizable *k-ε* model satisfies the constraint condition of *Re*. Therefore, the Realizable *k-ε* model corresponds to the real situation, which can simulate the injecting diffusion speed accuracy.

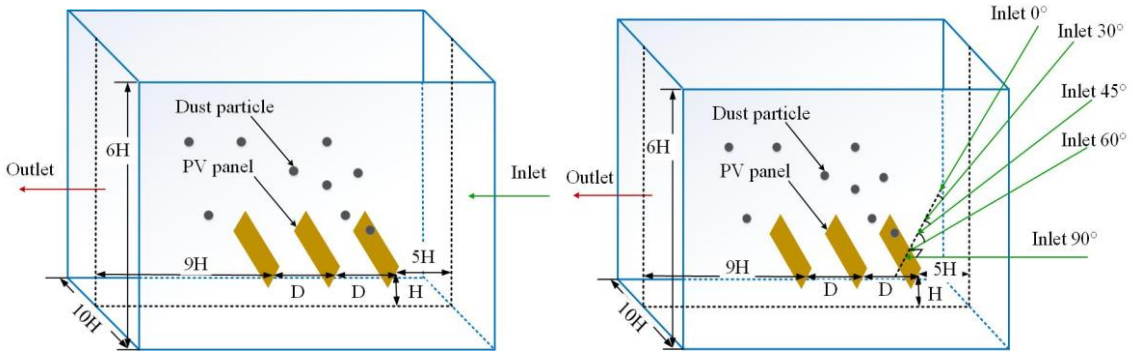

(a) (b)

Fig. 3-1. Module of computation domain for the case of monsoons. (a) traditional method [109] (b) proposed method

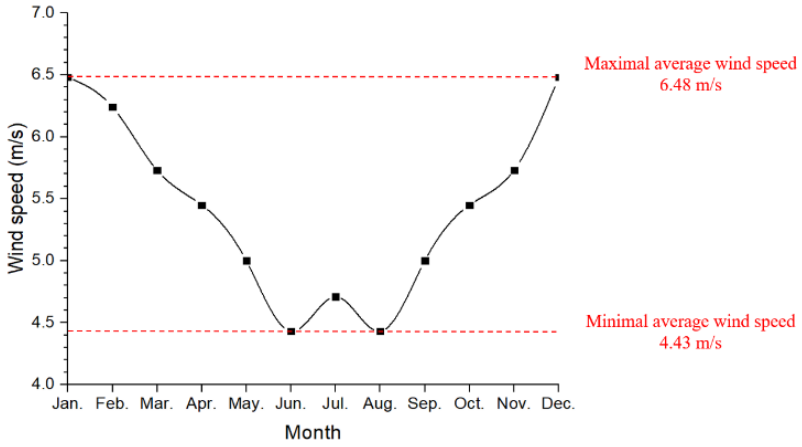

Fig. 3-2. Average wind speed in England (www.xcweather.ac.uk).

$$D = \frac{\cos A \times H}{\tan[\sin^{(-1)}(\sin\phi\sin\delta + \cos\phi\cos\delta\cos\omega)]} \tag{3.1}$$

where *D* is the obstruction spacing (m), *A* is the solar azimuth (°), φ is the latitude (°), δ is the

declination (°), H is the PV array height difference (m) and ω is the time angle (°) [103].

3.2.1.1 Discrete phase

DPM Model of Lagrange uses the liquid phase as a continuous medium in the calculation and solves the fluid control equations in Euler's coordinate system. The solid sand phase is regarded as a discrete medium in the Lagrangian coordinate system. To solve the sand particle motion, the equations use the iterative calculation to perform the solid-liquid coupling [112-114]. Aeolian sand belongs to multiphase flow, in which the particle phase is a discrete phase and the gas phase is continuous.

In the DPM model, since the shapes of dust particles are irregular, it is difficult to analyze the external force in the numerical simulation calculation, such as the collision force and viscous force, etc. In this study, a general assumption is made that the particles are spherical, and there are no collisions between the particles. Hence no internal energy is generated. Under this assumption, the particle tracking can be expressed by the discrete phase equation. During the period of particle motion in the turbulent field (airflow), the particles are one-way coupled with the airflow. It will generate collision force and adhesion force between each particle. However, the volume fraction of the particles are smaller than 10^{-6}, so the collision force and adhesion force produced by the particles during the particle tracking process is negligible. Due to the particle motion in the non-near-wall turbulent flow, the particles are affected by Magnus force, which means the particles in the airflow move and rotates randomly. However, the Magnus force is much smaller than the viscous force. As a result, the Magnus effect is neglected in the simulation.

In this model, the continuous phase flow field is first solved, and the discrete phase (dust particles) is added after the calculation results converge, and the discrete phase is set to perform an iterative calculation once every 10 steps of the continuous phase calculation.

The DPM equation can be expressed as follows:

$$\frac{du_p}{dt} = \frac{3}{4}\frac{C_D \rho \left| u_p - u \right|}{\rho_p d_p}(u - u_p) + \frac{g(\rho_p - \rho)}{\rho_p} + \vec{F} \tag{3.2}$$

$$\begin{cases} C_D = \dfrac{24}{\mathrm{Re}}(1 + 0.15\,\mathrm{Re}^{0.687}) & (C_D \le 1000) \\ C_D = 0.44 & (C_D > 1000) \end{cases} \tag{3.3}$$

$$\mathrm{Re} = \rho u L \Big/ \mu \tag{3.4}$$

where C_D is the drag coefficient, ρ is the fluid density (kg/m^3), ρ_p is the particle density (kg/m^3), u is the wind velocity (m/s), u_p is the velocity of the particles (m/s), and $\vec{F}$ is an additional acceleration (force/unit particle mass) term. *Re* is Reynolds constant, L is the length of fluid field (m), and μ is the viscous force (Pa·s).

Eq. (3.3) can illustrate the drag force, gravity force, and lift force (Saffman force) of the dust particles in the CFD simulation [101], [104].

3.2.1.2 Turbulence model

In the study of two-phase flow, there are two hypothetical methods: the first method is to use the fluid as a continuous medium and the particle group as a discrete system. The second method is to treat the fluid as a continuous medium. The particle group is also regarded as a quasi-continuous medium or quasi-fluid. FLUENT corresponds to a discrete phase model, continuous phase flow model (VOF model, mixed model, Euler model). This study chooses the discrete phase model as the simulation model. FLUENT solves the continuous phase (gas) transport equation while simulating the second phase (solid particles) of the discrete phase in the flow field in Lagrange coordinates. The discrete phase model in FLUENT assumes that the volume fraction of the second phase is generally smaller than 10%, which means the effect of particle-particle interaction and particle volume fraction on the continuous phase is not considered.

Therefore, in the CFD simulation, the airflow, namely the wind-velocity inlet, can be described as a continuous phase. It can be expressed by the Navier-Stokes equation [103], which describes the conservation of viscous incompressible fluid momentum as:

$$\rho \frac{du}{dt} = -\nabla p + \rho F + \mu \Delta u \tag{3.5}$$

where ρ is the fluid density (kg/m^3), u is the wind velocity (m/s), p is the pressure (Pa), F is the external force (N), and μ is the dynamic viscosity coefficient.

The physical structure of the turbulence model consists of large vortices and small eddies, where large-scale vortices are affected by inertia, while small-scale vortices are determined by viscous forces. In the wind-sand two-phase flow, the discrete phase is coupled with it, and the Lagrangian algorithm is used to track the particles in the turbulent flow field.

When the airflow is turbulent, the turbulence model requires an extremely large computer memory and a high computational speed. The realizable *k-ε* model is able to release the burden of computational memory and achieve high precision.

In the calculation process, the turbulent energy equation from [115-116] is used to express the motion dynamics of the wind-sand field, and the turbulence intensity decides the wind flow degree.

The turbulent energy equation is:

$$K = \frac{3(uI)^2}{2} \tag{3.6}$$

where the turbulence intensity *I* can be described as:

$$I = 0.16\,\mathrm{Re}^{-1/8} \tag{3.7}$$

where *u* is the wind velocity (m/s), *Re* is Reynolds constant.

In the assumptions of the model, the two-phase flow model selected is a flow model of gas and solid particles. In this model, the prediction of dust deposition, collision, friction, and stickiness with solid walls is relatively accurate. This is in line with the situation simulated in this study. The air carries particles with a lower concentration (1.17 kg/m^3) and smaller particle sizes (10 μm to 100 μm). The collision between particles during the movement can be ignored. It is believed that particles and gases have good followability. While achieving better numerical simulation, it guarantees accuracy and saves time.

3.2.2 Experiment setup

An experiment is designed to verify the deposition of dust particles on the solar panels in the simulation and the effect of dust deposition on the power generation efficiency of PV panels. The equipment includes a fan (SHT-30 portable propeller ventilator), a pipe, a solar panel (RS PRO), a thermometer (IP 54), a voltmeter, an electronic scale (APTP 452), and sands. The dust particles under 100 μm were sieved by using 150 mesh sieves.

The system configuration of the experiment is shown in Fig. 3-3. PV panels are placed in the courtyard with four walls, and the walls can serve as the boundaries of the entire area. In this way, PV panels can avoid the interference of the outside wind to the greatest extent. Meanwhile, the natural sunlight and the ambient temperature make the settlement and power generation effect

more realistic. The fan as a jet source provides turbulent energy for dust particles. The pipe can be used as a boundary layer to prevent the wind flow from diffusing. Meanwhile, dust particles are injected into the entrance port, so the sand and dust move randomly with the turbulent flow direction to distribute on the PV panel. A thermometer and a voltmeter are used to measure the data when the voltage changes with the temperature.

In [111], the data measured under STC can be used as a reference, such as the surface temperature, dust density, and output power of the PV panel. After measuring the quantity of the dust particles, which are deposited on the PV panel. The relationship between solar power generation and dust density can be obtained.

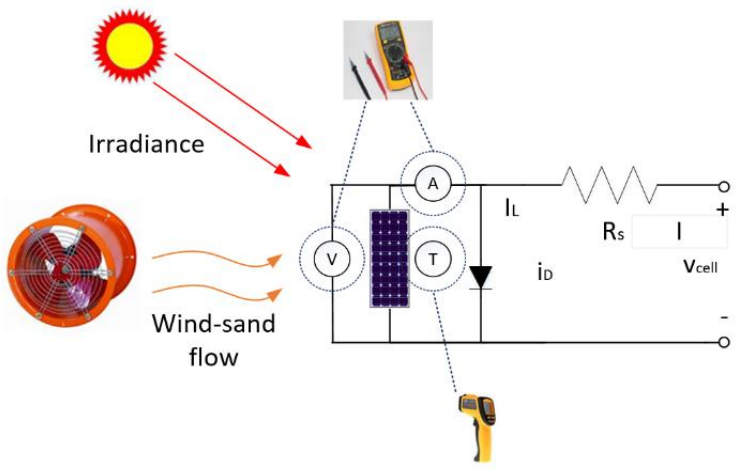

Fig. 3-3. Measurement of RS PV panel

In this study, the RS PV panels are used, whose physical size is 300×210×20 mm. Technical specifications of the PV panel are shown in Table 3-1, which are measured under the STC. The optimal tilt angle of the PV panel is set to 56°. There are 36 PV cells in the PV module. The PV power generation efficiency of PV panels was studied by observing the occlusion rate of PV cells by dust particles.

TABLE 3-1 SURFACE TEMPERATURE OF PV PANELS PARAMETER OF PV PANELS

Symbol	Parameter	Value
W_p	Peak Power	5 W
V_{mp}	Max. power Voltage	17.5 V
I_{mp}	Max. power Current	0.29 A
V_{oc}	Open Circuit Voltage	22.0 V

I_{sc}	Short Circuit Current	0.32 A

According to the flow equation (3.8), when the distance between the PV panel and the tuyere increases, the wind speed decreases. The wind velocity at a certain position in the wind field can be described as:

$$v = QA \tag{3.8}$$

$$Q = \alpha S \tag{3.9}$$

$$\frac{v_1}{v_0} = \frac{QA_0}{Q_0 A} \tag{3.10}$$

where A_0 (m^2) and Q_0 (m^3/s)are the airflow at the cross section and the flow rate at the outlet of the air duct, respectively. Meanwhile, A (m^2) and Q (m^3/s) are the airflow at the cross section and the flow rate at a certain distance from the outlet, respectively. α is the turbulence coefficient and S is the distance between the specification place and the tuyere (m).

The dust fluxes can be described as [117]:

$$F_D = aEc\frac{\rho_\alpha}{g}u_*^3(1+\frac{u_{*t}}{u_*})(1-\frac{u_{*t}^2}{u_*^2}) \tag{3.11}$$

$$u_{*t} = \frac{u_*}{\kappa} In(z / z_0) \tag{3.12}$$

where E is the erosion factor, α is the sandblasting efficiency, c is the empirical proportionality constant, g is the gravitational acceleration (m/s^2) , ρ_α is the air density (kg/m^3), u_* is the friction velocity (m/s) and u_{*t} is the threshold friction velocity (m/s). κ is the empirical constant, which is roughly 0.35 for turbulent flow, and z_0 is the roughness length (m).

Considering the effect of wind speed on the dust particle motion, and according to (3.11) and (3.12), the density of incident particles is set to 0.1 g/s. The turbulence coefficient is shown in Table 3-2. The turbulence coefficient α and jet diffusion angle 2α are affected by the turbulent intensity. When the turbulent intensity increases, the surrounding medium is driven to increase. In this situation, the turbulence coefficient α is 0.12. The wind speed of the fan used in this experiment is 10 m/s. According to (3.10), the position of the PV panel can be calculated to identify the

incident wind speed.

TABLE 3-2 TURBULENCE COEFFICIENT

Nozzle Type	α	2α
Shrinking Nozzle	0.066	25°20´
	0.071	27°10´
Cylindrical Tube	0.076	29°00´
	0.08	
Axial fan with air deflector	0.12	44°30´
	0.20	68°30

Finally, the surface temperature of the PV panel is measured with a thermometer. Meanwhile, the voltage value of the PV panel is detected by a voltmeter. To get an accurate temperature-voltage relationship, the detection of the data is continuously monitored within 30 minutes. Then, repeat the experiment after the PV panel is cooled for 10 minutes.

3.3 Results

In this part, firstly, the dust particles accumulated on the surface of PV panels in different environments were simulated, and the accuracy of dust accumulation was verified by experiments. Then, the change of temperature of the PV panel surface and the occlusion is measured under different dust accumulation conditions. Finally, the power variation of the PV panel is measured.

3.3.1 Simulation results

3.3.1.1 Simulation results of dust deposition

The results display the dust accumulation when the wind flows from different angles in terms of 0°, 30°, 45°, 60° and 90° to the PV panel, as shown in Fig. 3-4. The dust accumulation on the surface of the PV panel is different when the wind speed varies. The table in Fig. 3-4 shows that the samples of dust density are minimal, middle, and maximal wind speeds with different inject angles. In the numerical simulation, FLUENT was used to count the particle weight with zero velocity on the surface of the PV panel. In the test, a simulated wind tunnel is used to perform a

blowing experiment to simulate the wind speed and blowing angle under actual conditions. After multiple times (at least 3 times), weight measurement is performed when the weight is no longer increased. The weight includes the dust and PV panel.

Referring to the trend in Fig. 3-4, it is known that there are two peak values for the quantity of dust deposition. The curve in Fig. 3-4 shows the values of dust accumulation with different wind inlet angles. The number of dust particles accumulates at the first peak value, while the wind speed changes between 4.43 m/s and 5 m/s. During this period, the wind velocity is not high enough, and the viscosity is higher than the collision force between the dust and PV panel. As the wind speed increases, the turbulent energy is greater than the viscous force, and the dust on the surface of the PV panel begins to decrease. Then, the dust particles accumulate at the position with the second peak value, while the wind speed changes between 5 m/s and 6 m/s. During this period, the wind velocity is high enough, and the collision force is higher than the viscous force between the dust and PV panels. After that, the quantity of dust on the PV panel surfaces tends to be stable. Moreover, the critical value of dust deposition is not only decided by the wind speed but also the wind direction. For example, in the first steady time period, the maximum dust deposition at 90° is achieved with the wind speed of 5 m/s. It is obvious at the time of the second peak.

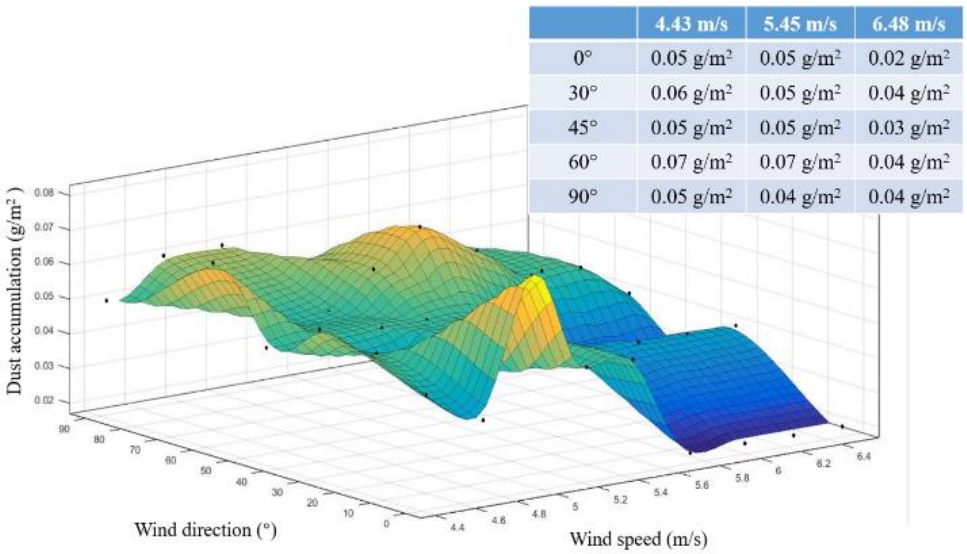

	4.43 m/s	5.45 m/s	6.48 m/s
0°	0.05 g/m²	0.05 g/m²	0.02 g/m²
30°	0.06 g/m²	0.05 g/m²	0.04 g/m²
45°	0.05 g/m²	0.05 g/m²	0.03 g/m²
60°	0.07 g/m²	0.07 g/m²	0.04 g/m²
90°	0.05 g/m²	0.04 g/m²	0.04 g/m²

Fig. 3-4. Simulation results of dust deposition in various air conditions

According to Fig. 3-4, a set of theoretical principles can be derived to directly observe the dust accumulation of PV panels in England. Influenced by the wind directions, the dust distribution and dust density of PV panels are different. The formula group (3.13) shows the relationship between the wind speed and dust accumulation at certain wind directions.

$$\begin{cases} y_{0^\circ} = -0.1315x^5 + 3.6069x^4 - 39.3442x^3 + 213.3849x^2 - 575.3697x + 617.0866 \\ y_{30^\circ} = -0.0112x^5 + 0.3276x^4 - 3.7934x^3 + 21.8242x^2 - 62.3825x + 70.9352 \\ y_{45^\circ} = -0.0059x^5 + 0.1803x^4 - 2.1471x^3 + 12.5746x^2 - 36.2668x + 41.3162 \\ y_{60^\circ} = -0.0262x^5 + 0.7603x^4 - 8.7744x^3 + 50.3571x^2 - 143.6585x + 163.9765 \\ y_{90^\circ} = 0.0056x^5 - 0.1875x^4 + 2.4407x^3 - 15.4579x^2 + 47.8541x - 58.0582 \end{cases} \quad (3.13)$$

where x is the wind speed (m/s) and y is the density of dust accumulation (g/m^2).

Although in some situations, the quantities of dust deposition are the same, the distribution varies when the wind changes. For example, in Fig. 3-5, the cases with 5 different wind directions and 8 different wind speeds are compared. There are two situations for dust distribution: focus deposition and average deposition. Combined with Fig. 3-4, Fig. 3-5 shows a more visual representation of the cumulative distribution of sand and dust at different wind speeds and wind directions. In Fig. 3-5 (a), the dust accumulation on the PV panel with a 0° wind inlet is a focus deposit on a part of the panel. Therefore, the irradiance on this part is very week, which is only 600 W/m^2, which is the same as that shown in Fig. 3-5 (d). In addition, Fig. 3-5 (b), Fig. 3-5 (c), and Fig. 3-5 (e) show the same situation, which is affected by the average dust accumulation. In this circumstance, the irradiance is 800 W/m^2. The average dust distribution generally only affects the PV power generation, and the concentrated distribution of dust can damage the PV panels. The reason for this is that the dust covering the surface of the PV panel affects the irradiance and blocks heat dissipation. It impacts the power generation efficiency of a PV panel, which will be explained in the next section.

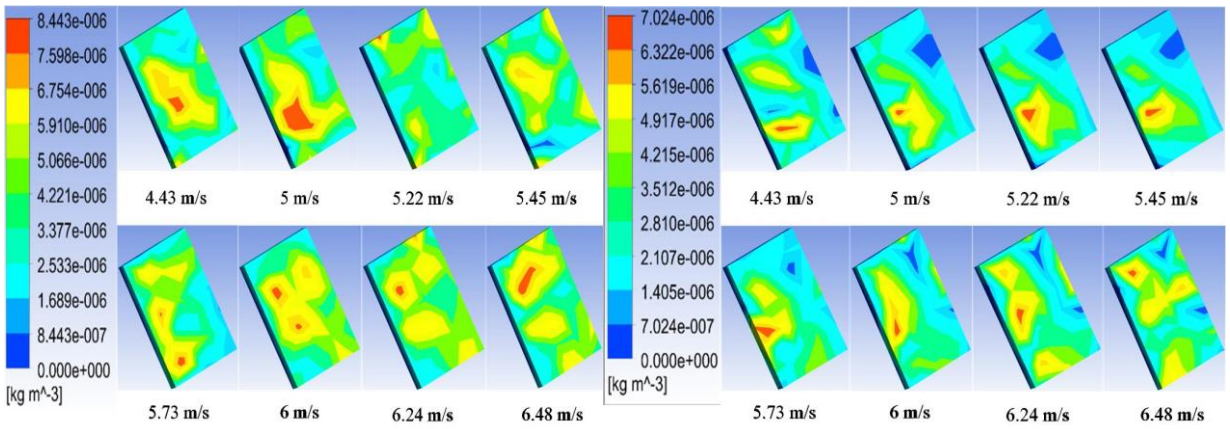

(a) (b)

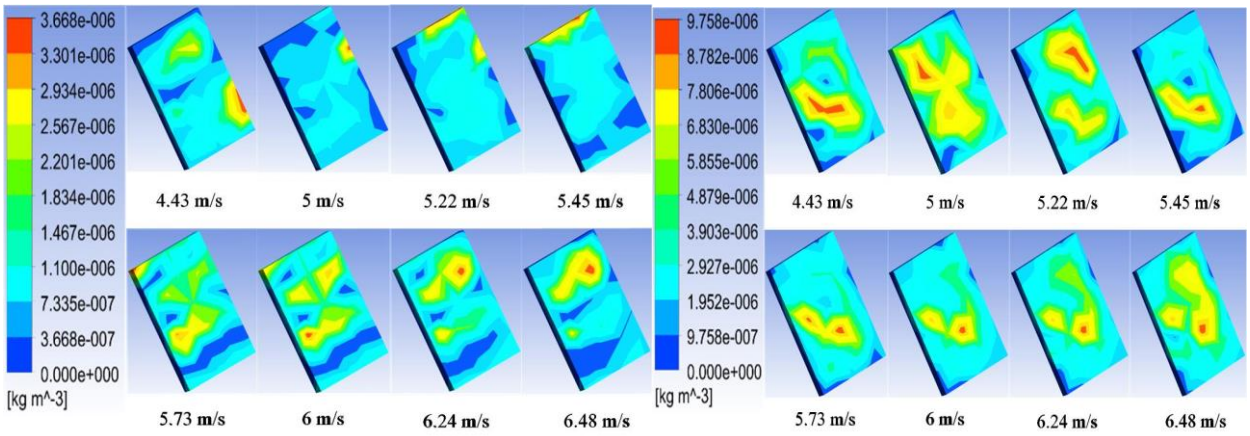

(c) (d)

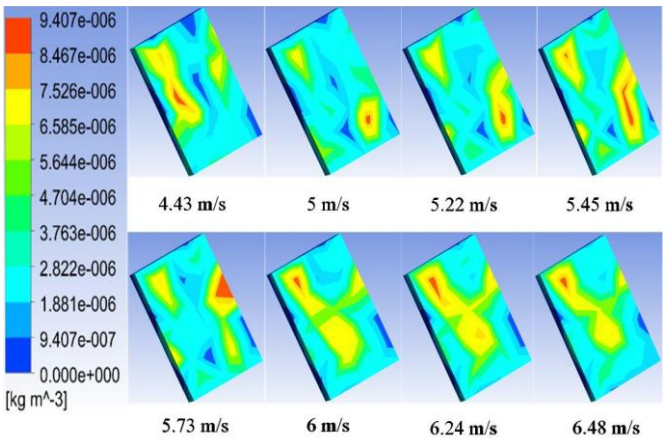

(e)

Fig. 3-5. Diagram of dust deposition on the PV panel. (a) 0° wind direction (b) 30° wind direction (c) 45° wind direction (d) 60° wind direction (e) 90° wind direction

3.3.1.2 Simulation results of the TKE

After analyzing the PV panels, the PV array needs to be briefly analyzed. After all, in the PV array, the front, and rear PV panels have a turbulent effect, which is important for power generation. In order to figure out the dust particle motion around the PV array, the TKE should be analyzed in the CFD simulation. By analyzing the PV array, the following information is derived: The turbulence impacts the dust distribution around the PV panels. The TKE is shown in Fig. 3-6.

According to (3.4), (3.5), and (3.6), the TKE is affected by the velocity and turbulence intensity, and the higher the turbulence intensity is, the greater the TKE is. Meanwhile, the turbulence intensity is determined by the Reynolds constant. The larger the Reynolds constant is, the greater the fluid density is, and at this time, the inertia effect is greater than the viscous force. Therefore,

the impact of the particle on the PV array is related to the wind velocity.

In Fig. 3-6 (a), the TKE distribution of the PV array is uneven, and the turbulent energy between the first panel and the second panel is large, and the upper portion is particularly dense, indicating that the particle concentration here is high. Due to the blockage of the first and second PV panels, the wind speed is decreased when reaching the third panel, so the TKE between the second PV panel and the third PV panel is reduced. Finally, due to the influence of turbulence, a large number of dust accumulate in the back-bottom part of the third panel, and when the wind speed increases, the accumulation amount increases too.

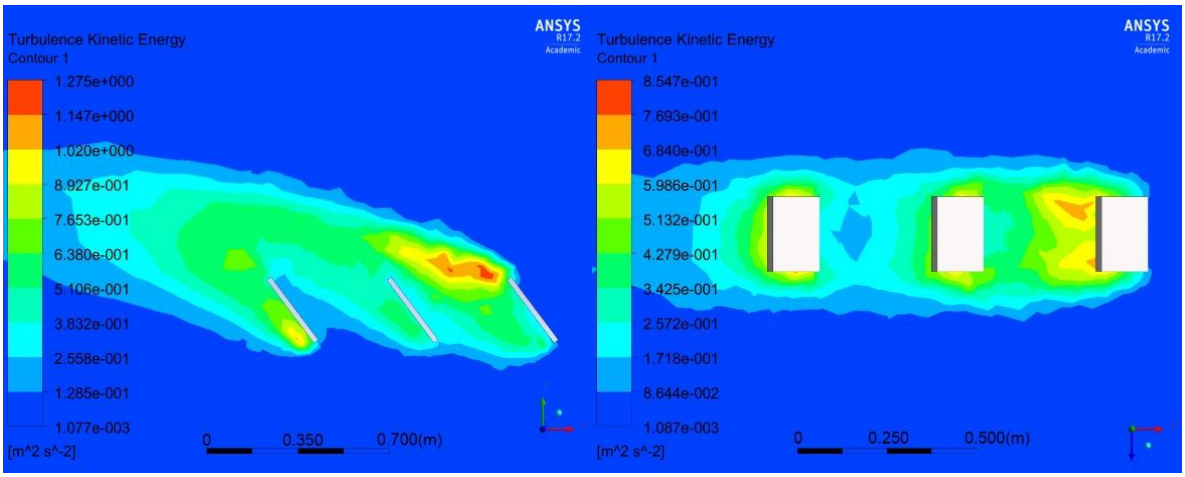

(a) (b)

Fig. 3-6. The TKE of PV array in CFD. (a) the left view of dust particle deposition of 100 μm dust diameter with 5 m/s wind velocity (b) the top view of dust particle deposition of 100 μm dust diameter on 10 m/s wind velocity

It can be observed from Fig. 3-6 (b) that the front panels decrease the TKE to the rear panels, and it can be seen from the top view that the TKE between the PV panels is not uniform, and as a result, fewer particles accumulate on the rear panels. Thus, the amount of dust accumulated on the surface of the PV panel is different, which is affected by the front panel. However, the non-uniform TKE drives the particles to adhere to a small part of the PV panel and causes a high temperature in that part. Therefore, the panel in the middle should be concerned to prevent the hot spot effect.

To sum up, at different wind speeds, the TKE in the PV array is different. Combining with Fig. 3-2 and Fig. 3-5, in the northern area of England, represented by Liverpool, the amount of PV dust deposition is generally small, which is suitable for the construction of PV power stations. The minimal dust deposition cycle is from December to March, and the maximal value is from August to October. Therefore, from August to October, PV panels need to be maintained to avoid hot-spot

effects and DC arc shock caused by dust.

3.3.2 Experiment results

3.3.2.1 Accuracy of simulation

The particle densities from the simulation and experiment results are shown in Fig. 3-7. Comparing the simulation results with the experimental results, it is found that the two groups of data witness a very similar trend. Analyzing the diagram in Fig. 3-7, when the wind speed varies in a year, the errors of dust accumulation between experiment and simulation are not totally the same in each wind direction. From 0 ° to 90 ° wind inlet, the average error is 0.5%, 0.4%, 0.2%, 0.2% and 0.3% respectively. As a result, the actual dust deposition value can be predicted by using (3.14) in the England. Therefore, since the finite element simulation results are highly accurate, the simulation data can be used to predict the real situation of local PV power generation.

$$\begin{cases} y_{0^\circ} = (-0.1315x^5 + 3.6069x^4 - 39.3442x^3 + 213.3849x^2 - 575.3697x + 617.0866)(1 \pm 0.5\%) \\ y_{30^\circ} = (-0.0112x^5 + 0.3276x^4 - 3.7934x^3 + 21.8242x^2 - 62.3825x + 70.9352)(1 \pm 0.4\%) \\ y_{45^\circ} = (-0.0059x^5 + 0.1803x^4 - 2.1471x^3 + 12.5746x^2 - 36.2668x + 41.3162)(1 \pm 0.2\%) \\ y_{60^\circ} = (-0.0262x^5 + 0.7603x^4 - 8.7744x^3 + 50.3571x^2 - 143.6585x + 163.9765)(1 \pm 0.2\%) \\ y_{90^\circ} = (0.0056x^5 - 0.1875x^4 + 2.4407x^3 - 15.4579x^2 + 47.8541x - 58.0582)(1 \pm 0.3\%) \end{cases} \quad (3.14)$$

where x is the wind speed (m/s) and y is the density of dust accumulation (g/m^2).

According to Fig. 3-7, the first two batches of experiments were carried out at a low airflow angle, where the dust particles carried by the airflow were less constrained on the surface of the solar panel, and the sedimentary motion of the particles was more cluttered, resulting in relatively large data changes in the experiment and a large deviation in the simulated results.

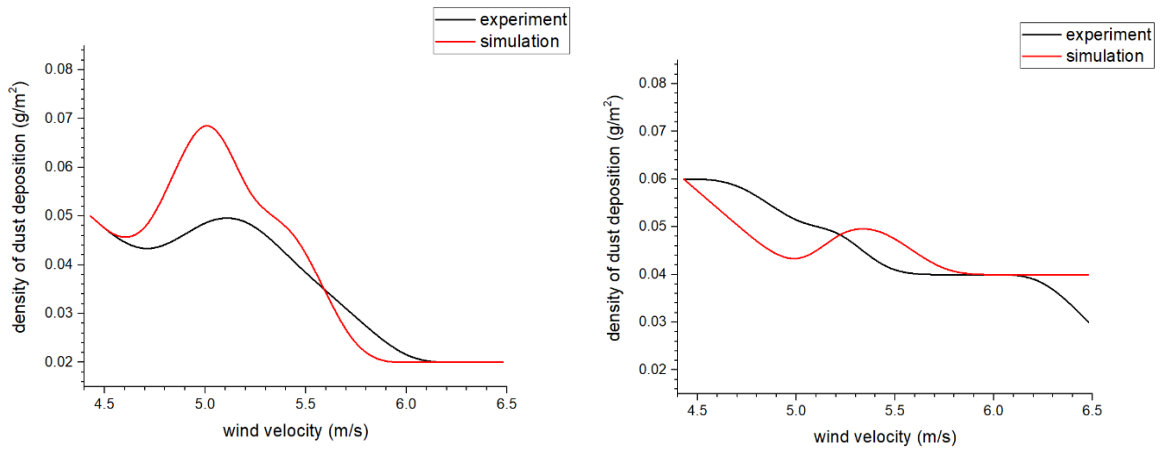

(a) (b)

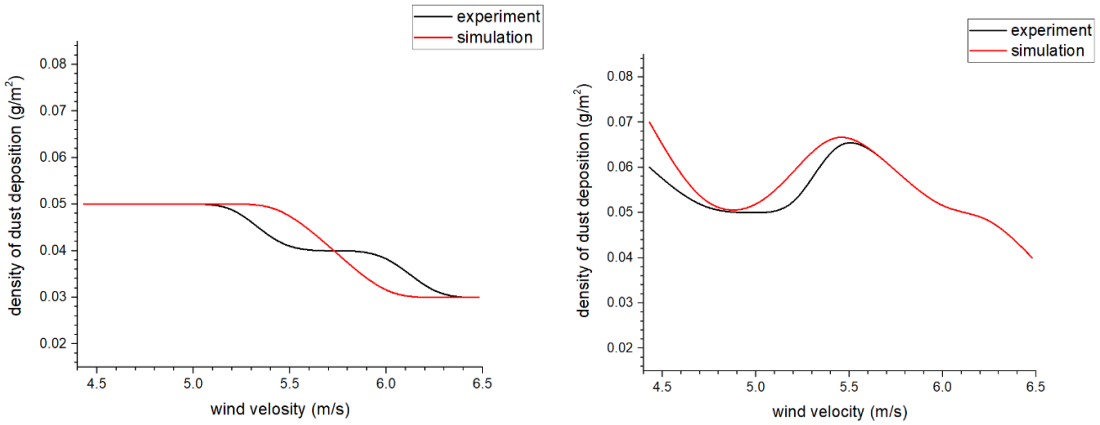

(c) (d)

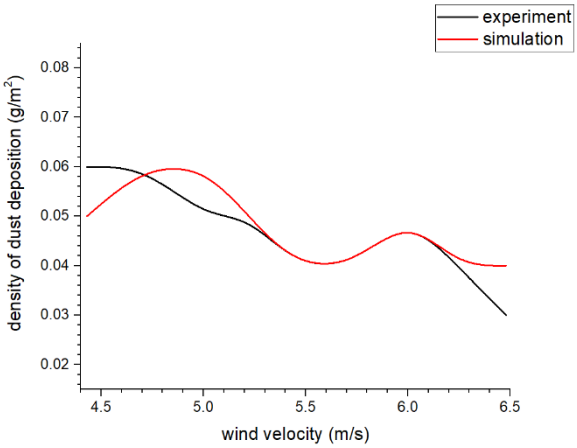

(e)

Fig. 3-7. Comparison of experiment value and simulation value of dust deposition. (a) 0° wind direction (b) 30° wind direction (c) 45° wind direction (d) 60° wind direction (e) 90° wind direction

To conclude, after verification, the dust is related to the wind speed, and a lower wind speed results in a lower dust density. In addition, due to the high accuracy of simulation results, the situation of dust deposition in a region can be detected by using CFD simulation.

3.3.2.2 Impacts of dust depostion on temperature and output of PV panels

Since the dust accumulation of PV panels in a region can be obtained through simulation, this section will analyze the impact of sand and dust accumulation on temperature and PV power generation efficiency. It can determine whether a place is suitable for building a PV station.

The comparison between a clean PV panel and a dusty PV panel was implemented with 100 μm dust particles at the wind speed of 5 m/s when the wind flows vertically (90°) to the surfaces of

the PV panels. The maximum surface temperature of the clean PV panel is 28.1 ℃ in Liverpool over one day, and the maximum surface temperature of the dusty PV panel is 32.6 ℃ in the same condition. Since the material of the PV panel is polysilicon, it is very sensitive to temperature changes. Since the dust covering the surface of the PV panel prevents the heat of the panel from being released, and cannot be transmitted outward, the temperature becomes high.

From Fig. 3-8 (a), it can be seen that the panel surface temperature has a great influence on the output voltage of the PV panel. When the surface temperature of the PV panel reaches 33.2 ℃, it does not increase further. The dust covering the surface of the PV panel not only blocks the irradiation but also blocks the heat dissipation that affects the power generation efficiency. Therefore, when the dust accumulates on the PV panel, the output voltage of the PV panel decreases. In addition, when the temperature rises, the forbidden bandwidth of the solar cell becomes narrower, so the open-circuit voltage decreases. Because the bandgap is narrow, more electrons can transit from the valence band to the conduction band, and the short circuit current increases, and the temperature affects the open-circuit voltage. The impact on the short-circuit current is small, so the overall temperature rises, and the battery power drops. Then, the output power at a certain temperature is obtained when the dust accumulates in different situations.

From Fig. 3-8 (b), there are two situations for dust accumulation: almost average accumulation and focusing on a part of a PV panel. Considering the factors of shading area and temperature rise, the PV power generation decreases by 46%~70% in different environmental conditions. When the dust deposition focuses on a part of a PV module, the irradiance of the shading part is roughly 600 W/m^2. Because of the quantity of the dust particles on the PV panel, there are three situations:

(a) There is 0.02 g/m^2 dust shading on 1 PV cell, and 1 cell occupies 5% of a module.
(b) There is 0.04 g/m^2 dust shading on 4 PV cells, and 4 cells occupy 10% of a module.
(c) There is 0.05 g/m^2 to 0.08 g/m^2 dust shading on 14 PV cells, and 14 cells occupy 30%~40% of a module.

When the dust deposits averagely on a PV module, the irradiance of the shading part is 800 W/m^2 approximately. There are also three situations of dust accumulation:

(a) There is 0.02 g/m^2 dust shading on 4 PV cells, and 4 cells occupy 10% of a module.
(b) There is 0.04 g/m^2 dust shading on 9 PV cells, and 9 cells occupy 20%~30% of a module.
(c) There is 0.05 g/m^2 to 0.08 g/m^2 dust shading on 18 PV cells, and 18 cells occupy 50% of a module.

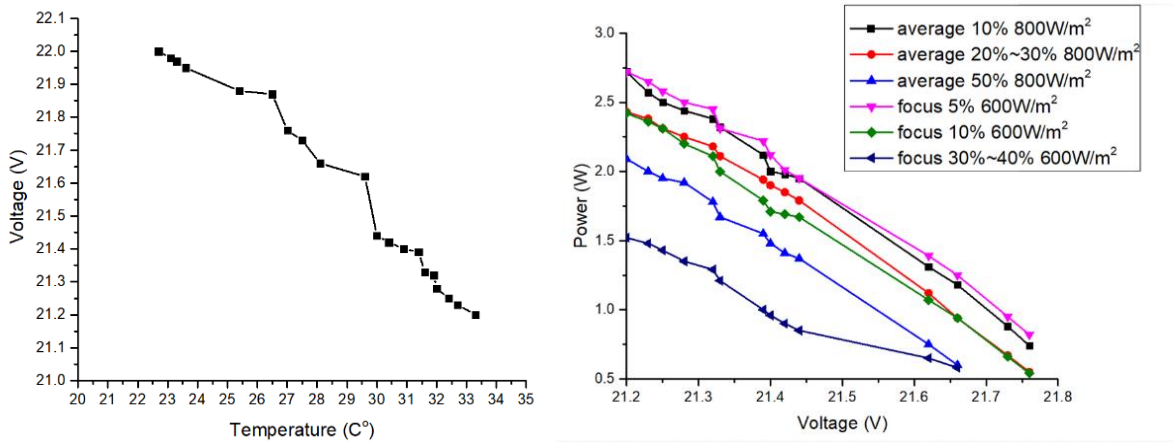

(a) (b)

Fig. 3-8. Measured data (a) temperature-voltage curve (b) P-V curve

To sum up, dust deposition affects PV power generation efficiency. The thicker the dust is, the lower the output voltage is because the temperature of the PV panel rises sharply within 5 minutes. In addition, due to the impacts of dust deposition on PV power generation, the selection of PV stations should be concerned while the region has a large quantity of dust accumulation. If a station is chosen in a large dusty place, it will invest many resources in cleanings, such as cost and labor.

3.4 Summary

The deposition of dust particles on PV panels was studied by CFD simulation and further verified by an experiment in this study, which is based on the weather of Liverpool, England. The wind field was predicted by the Realizable *k-ε* turbulence model, and the DPM model of turbulent particle diffusion was used to simulate the dust deposition behavior. As long as the boundary conditions of the local situation are set, the corresponding environmental conditions can be obtained. Meanwhile, calculations are made in advance to predict the local suitability for building PV power plants.

Due to the influence of the monsoon, the most dust accumulation is presented from March to August. According to the experiment, the essence of dust effect on the efficiency of PV power generation affects the temperature of the surface of the PV panel. Dust particles impact the PV panels, and they also increase the temperatures of PV panels. After the measurement process, it was found that the output power of the PV panel is decreased from 46%~70% due to dust accumulation and the surface temperature change of the PV panel. Therefore, according to the dust shading and the surface temperature change of PV panel, the relationship between dust deposition and PV power generation can be obtained. As a result, the output power in a certain area can be

predicted. Meanwhile, in the PV array, there is an influence among the panels, resulting in uneven coverage of dust.

In summary, the numerical simulation method can accurately predict the dust accumulation on the PV panel and the distribution of the approximate dust pattern, which provides guidelines for the solar panel dust removal in the wind-sand environment. Meanwhile, based on the significant influence of the solar panel temperature on the output efficiency, how to effectively reduce the temperature in the local micro-environment of the solar panel will be the focus of the next step.

Chapter 4 Cost Effective Offline Reconfiguration for Large-Scale Non-Uniformly Aging Photovoltaic Arrays Efficiency Enhancement

4.1 Introduction

Thanks to the decrease in cost, solar energy generation is becoming popular all around the world over the years [19][118-122]. Currently, large-scale PV power plants are gaining popularity in the global renewable energy market, primarily owing to the mass production of PV modules with reduced cost and high energy conversion efficiency [123-124].

There are three factors that determine the PV generation system efficiency. They are the PV cell efficiency, PV array efficiency, and energy conversion efficiency. PV cell and energy conversion have been widely studied to improve the efficiency. With the improvement of technology, monocrystalline silicon and polycrystalline silicon production cost is decreased obviously. Currently, the typical polycrystalline silicon PV cell efficiency is 17.7% (Yinli Solar); the monocrystalline silicon PV cell efficiency is 19.8% (Yinli Solar) [125]. In energy conversion, a new generation of switching devices such as super junction MOSFET, silicon carbon (SiC) MOSFET, and new power electronics topologies such as multi-level DC-AC converter and resonant DC-DC converter have obviously improved the energy conversion efficiency [126-128]. Due to the soft-switching topology and high-quality switching devices, the energy conversion rate can be over 95% [128]. Therefore, there is limited room for improving efficiencies of PV cells and energy conversion. However, there is a large room for improving the PV array efficiency.

The non-uniform aging of PV array is a common phenomenon in the long service time, which is caused by dust, shadow, and water corrosion [129-131]. Fig. 4-1 is an example of aging improvement and global maximum power point (GMPPT). For the aging improvement, we need to change the position of PV modules according to the aging information. After rearrangement, the PV array output characteristic may still be with multi-maximum power points. GMPPT is a necessary algorithm that finds the global maximum power point. We can see from Fig. 4-1 that before rearrangement, the array GMPPT is 564 W. After rearrangement, the array global maximum power point is 690 W. The efficiency of the whole array can be improved by 22.3% when the working point of the array is at the GMPPT. Therefore, the proposed aging array rearrangement is complementary with GMPPT.

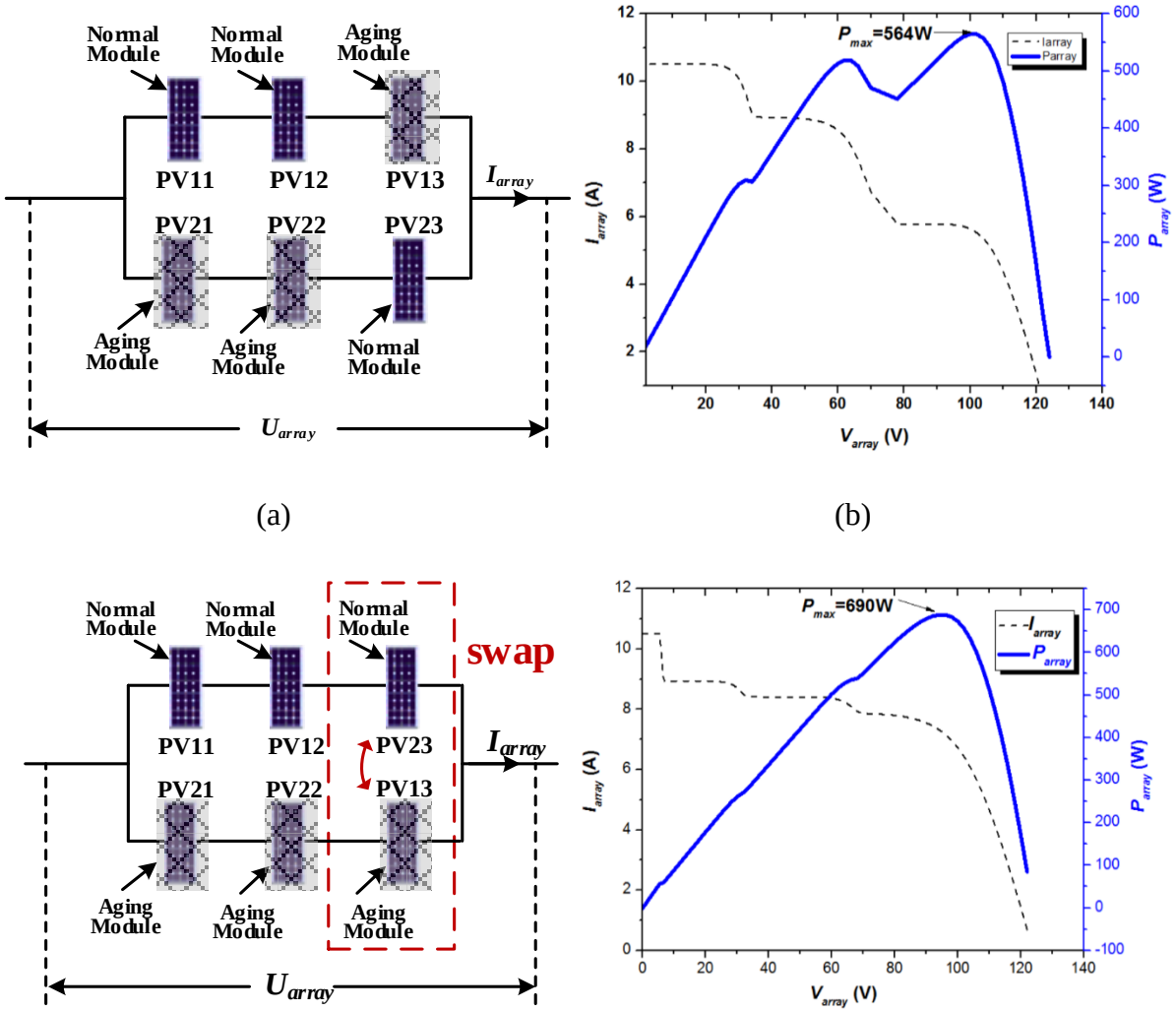

Fig. 4-1. Without and with rearrangement. (a) without rearrangement (b) Output character (Without) (c) with rearrangement (d) Output character (With)

To increase the effective service time, there are two important steps. The first step is PV array fault diagnosis; the second step is PV array reconfiguration. For PV array fault diagnosis, thermal camera [20][132-136], earth capacitance measurement (ECM) [137], time-domain reflectometry (TDR) [138], and applying voltage/current sensors are four popular methods for PV fault diagnosis. Due to the non-uniform temperature distribution of faulty PV arrays, thermal cameras can be adopted to locate the faulty PV modules in the online application background [20][132-136]. ECM can locate the disconnection of PV modules, and TDR can estimate the degradation of PV arrays, while both ECM and TDR can only be employed in offline fault diagnosis [137-138]. For scale PV array fault diagnosis, power loss analysis is proposed in [139-140]. For PV array reconfiguration, [141-144] only the small-scale reconfiguration example is given. Paper [145] proposed a classical optimization algorithm (COA) to reconfigure a total cross-tied (RTCT) arrays.

The branch-and-bound algorithm is employed to minimize the cost, while the COA still needs strong computational efforts. The look-up table method is developed in paper [143] for small-scale PV arrays, which is almost impossible to be used for large PV arrays. Paper [146] developed an exhaustive search algorithm. In order to speed up the selection of a configuration, paper [147] developed a sorting algorithm based on the best–worst paradigm. The fuzzy logical algorithm was also proposed to search for the best reconfiguration [148]. Paper [149-151] gives the summary of the state-of-art online reconfiguration of PV array.

However, there is no report on large-scale PV array reconfiguration. Currently, PV array reconfiguration is mainly implemented by relay networks, which needs a large number of relays and high system cost. For large-scale PV arrays, the only feasible solution for PV reconfiguration is swapping PV modules by human labor offline, as shown in Fig. 4-2. In order to decrease the labor cost, the key technology is to develop an optimized reconfiguration strategy to decrease the swap times and achieve the maximum power at the same time. In this paper, the optimized reconfiguration strategy with the minimum swap times and maximum output power is proposed to decrease the labor cost.

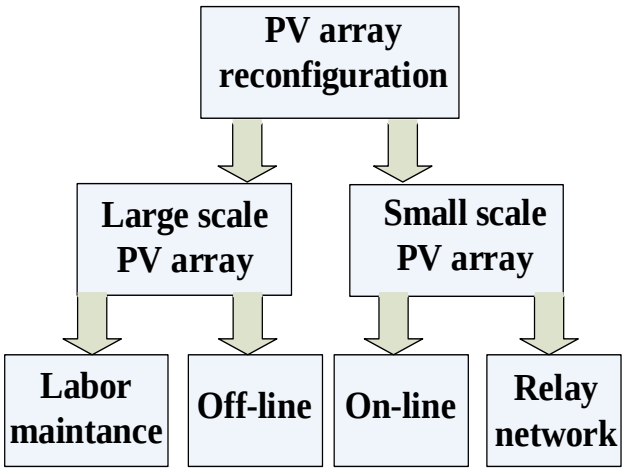

(a)

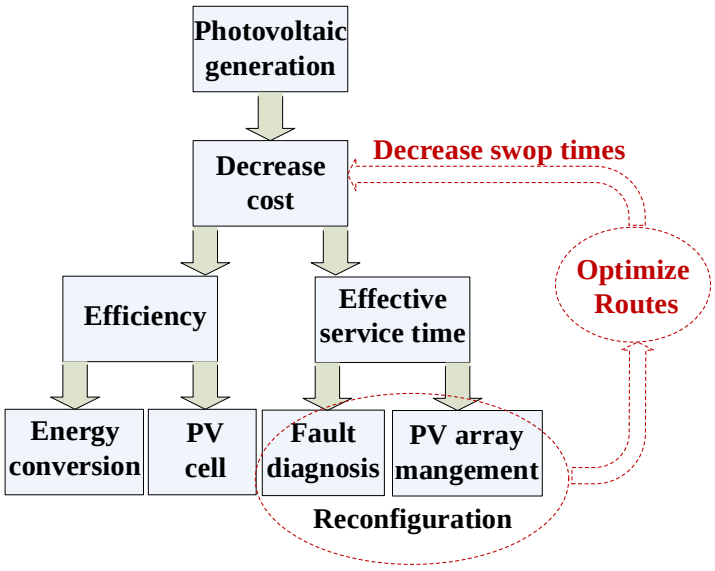

(b)

Fig. 4-2. PV array reconfiguration strategy. (a) PV array reconfiguration (b) PV array reconfiguration considering labor cost

For this chapter, in section 4.2, four levels model including cell-unit, PV module, PV string and PV array are introduced. In section 4.3, two physical methods are illustrated. In section 4.4, the lost cost PV array rearrangement strategy is developed. Meanwhile, simulation and experiment are presented to verify the proposed method. The summary is given in the final part.

4.2 Mathematical Modeling

Non-uniform aging is a common problem in PVs which can be caused by lasting dust, shading, or water corrosion over a long time [129-130].

The electrical characteristics of PVs are influenced by both temperature and illumination. The electrical model of the PV cell is expressed by [119].

$$I = I_{\mathrm{L}} - I_{\mathrm{o}}[\exp(\frac{\varepsilon \cdot V}{T_m}) - 1] \tag{4.1}$$

$$\varepsilon = \frac{q}{N_s \cdot K \cdot A} \tag{4.2}$$

$$I_L = \frac{G}{G_{ref}}[I_{Lref} + k_i(T_m - T_{ref})] \tag{4.3}$$

$$I_o = I_{oref}\left(\frac{T_m}{T_{ref}}\right)^3 \exp\left[\frac{q \cdot E_{BG}}{N_s \cdot A \cdot K}\left(\frac{1}{T_{ref}} - \frac{1}{T_m}\right)\right] \tag{4.4}$$

where I is the PV module output current, I_L is the photon current, q is the quantity of electric charge, A is the diode characteristic factor, K is the Boltzmann constant, I_o is the saturated current, T_m is the PV module temperature, G is the irradiance, V is the output voltage, G_{ref} is the reference irradiance level (1000 W/m²), I_{Lref}, I_{oref} are the reference values for I_L and I_o. k_i is the current-temperature coefficient provided by the PV manufacturer. T_{ref} is the reference temperature, N_s is the number of series-connected cells, T_m is the PV module temperature. ε is a constant depending on q, N_s, K, A, and is calculated by the following equation:

$$I_{sc\_ref} - I_{mpp\_ref} = \frac{I_{sc\_ref}}{\exp\left(\frac{\varepsilon \cdot V_{oc\_ref}}{T_{ref}}\right) - 1}\left[\exp\left(\frac{\varepsilon \cdot V_{mpp\_ref}}{T_{ref}}\right) - 1\right] \tag{4.5}$$

where I_{mpp_ref}, I_{sc_ref}, V_{mpp_ref} and V_{oc_ref} are the maximum power point (MPP) current, short-circuit current, MPP voltage and open-circuit voltage at a reference condition defined by the relevant standard.

A PV string consists of s PV modules, with the terminal voltage V_{string} and current i_{string}. Let the terminal voltage, current and maximum current from the k th PV module be $V_{module,k}$, $i_{module,k}$ and $i_{module,k}^{max}$, respectively. The following relationship can be established.

$$i_{string} = i_{module,1} = i_{module,2} = \ldots = i_{module,s} \tag{4.6}$$

$$V_{string} = V_{module,1} + V_{module,2} + \ldots + V_{module,s} \tag{4.7}$$

Similarly, the bucket effect indicates that the maximum current in the PV string is limited by the minimum $i_{module,k}^{max}$ of those non-bypassed modules. That is $i_{string} \le i_{module,k}^{max}$, $1 \le k \le s$, and the k th module is not bypassed.

In order to calculate the number of reconfigured PV panels T_{st}, the following notations are needed. Assume that the original PV array has m rows of PV panels connected in parallel, and each row has n panels connected in series. Define the reconfiguration function $f(k)$ for k= 1,2,…m*n, so that the value of $f(k)$ equals an integer from $\{1,2\ldots m*n\}$, and it represents the correspondence between the original PV array and the reconfigured PV array. For instance, for any PV module located in

the *i*-th row and *j*-th column, then this module corresponds to a number $k = i*n+j$, this module will be moved to the location of i'-th row and j'-th column, where are determined from the relation $f(k) = i'*n+j'$ that is, $j' = f(k) \bmod (n)$, $i' = \frac{f(k)-j'}{n}$.

In the calculation process of T_{st}, it is crucial to note that the movement of a panel within one row is not counted as a movement, since all modules in the same row are connected in series. It is also helpful to note that swapping two rows is not indeed a movement, as such a swap does not change the topological structure---this case usually scarcely happens. Keep this in mind, and T_{st} can be calculated as follows.

$$T_{st} = \min\{T_{st}^{l} : l = 1,2,3,\ldots,m!\} \tag{4.8}$$

where T_{st}^{l} is the number of reconfigured PV panels under the *l*-th permutation of these rows of the reconfigured solution. In the simplified approaches, such a permutation can also be ignored and one calculates the number of reconfigured PV panels for the reconfigured solution. For simplicity, let us assume that the first one *l*=1 corresponds to the reconfigured solution without row permutation, therefore all the other T_{st}^{l} can be calculated similarly.

$$T_{st}^{1} = \sum_{i=1}^{m} | A'_i \setminus A_i | \tag{4.9}$$

where $|.|$ means the number of elements of a set (i.e. the potential of a set), set A_i is defined as the set of panels in the *i*-th row, i.e. the set{n*(i-1)+1, n*(i-1)+2,…,n*(i-1)+n}; A'_i is the set of reconstructed panels consisting of the images of elements in A_i mapped by the reconstruction solution, i.e. A'_i={f(n*(i-1)+1), f(n*(i-1)+2),…,f(n*(i-1)+n) }; $A'_i \setminus A_i$ means to find the set of elements in A'_i but not in A_i.

4.3 Modeling the Cost of Reconfiguration

After the aging map of a PV array is detected, a remedial measure can be employed to rearrange the faulty PV modules prior to the replacement of the faulty modules, which increases the capital cost. For large-scale PV arrays, there are many reconfiguration routes. Different routes have different line reconnection times and wiring distances that determine the efficiency and cost of the reconfiguration progress. In order to propose an optimized reconfiguration solution, it is necessary to model the reconfiguration cost, which is approximated by the number of reconfigured panels for simplicity.

4.3.1 Calculation of permutation number based on branch and bound method

Branch-and-Bound (B&B) algorithm is one of the fundamental schemes for combinatorial search problems. It has been widely applied to NP-hard optimization problems such as intelligent system design, integer programming, SAT problems, and theorem proving. Many kinds of research concerning the theory and application of B&B have been reported in the literature. B&B has four basic components: the rules of branching, selection rules, elimination rules, and termination conditions. Branch rules and termination conditions depend on the specific search problem, and the selection rules referring to the slipknot point to identify the table has a better one or more nodes in order to further expand, elimination rules for as much as possible will not be able to derive the optimal solution of a node-set to promulgate the point. The PV array module calculated by GA should be switched on and off again, and the minimum number of replacements is required.

It is shown in Fig. 4-3 that the PV array switch replacement belongs to a wiring problem. Its solution space is a graph, so it is used as the first extended node from the starting position *a*. The feasible nodes adjacent to and accessible to the extended node are added to the queue of the node, and these squares are marked as 1, that is, the distance from the starting position *a* to these modules is 1. Then, the first node is taken from the node queue as the next extension node, and the unmarked position adjacent to the current extension node is marked as 2 and stored in the node queue. This process continues until the algorithm searches until the target location *b* or the queue at the node is empty. Then, *a* and *b* are interchanged with each other.

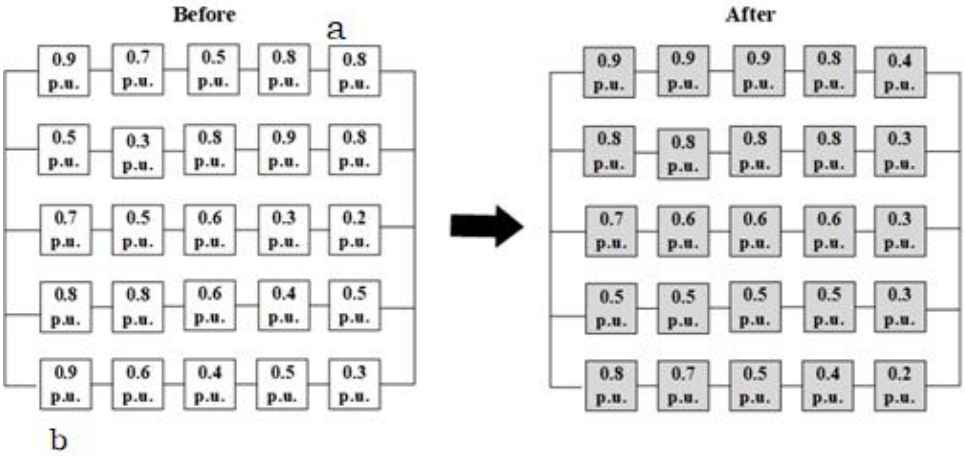

Fig. 4-3. Schematic diagram of PV module replacement

The specific algorithm is described as follows:

Step1：If the goal of the problem is to minimize, the value *Z*= infinity of the optimal solution is

set.

Step2：According to the branching rule, a node from a Fathomed node (local solution) is selected and divided into several new nodes at the next level.

Step3：Calculate the lower bound for each newly branched node.

Step4：The insight condition is tested for each node. If the node satisfies any of the following conditions, the node can be known and will not be considered: (1) The lower bound of the node is greater than or equal to the *Z* value. (2) A feasible solution with minimum lower bound value has been found in this node. (3) If this condition is true, it is necessary to compare the feasible solution with the z-value. (4) If the former one is smaller, it is necessary to update the z-value, which is the value of the feasible solution. This node cannot contain a viable solution.

Step5：To determine whether there are still unrecognized nodes. If unrecognized nodes exist, then go back to step 2. If there are no unrecognized nodes, the calculation stops and the optimal solution is obtained.

Given any PV array with maximum power generation P_b before reconfiguration, denote P_a the maximum power generation after the above B&B reconfiguration, then there exits a functional relationship *F* to represent this B&B process.

$$Pa = F(Pb) \tag{4.10}$$

The corresponding flowchart is presented in Fig. 4-4.

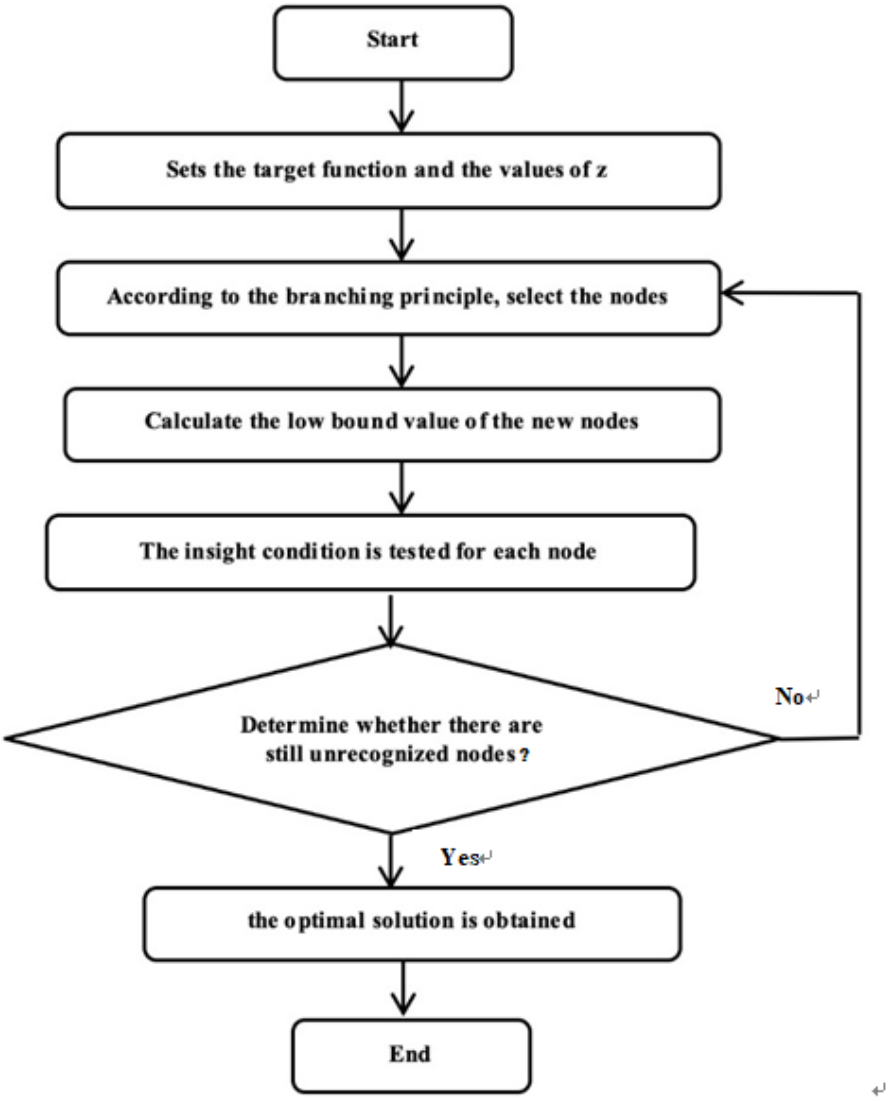

Fig. 4-4. Flowchart of the proposed algorithm

4.3.2 Cost analysis of PV array reconstruction

According to the survey, it is assumed that the PV array needs to be reconstructed once a year on average, and the PV array can generate power for 8 hours per day. A skilled grid worker needs an average of 45 mins to swap the PV modules from one place to another. Through the reconstruction of the PV array, the economic benefit of power generation can be increased by eliminating the labor cost caused by handling. The following equations are employed to calculate the labor cost and the electricity profit. In (4.11), M_p is the pure profit of the reconfiguration. In (4.12), M_1 is the labor cost, T_{st} is the number of reconfigured PV panels, and M_s is the average salary of the manpower. In (4.13), M_2 is the additional electric revenue profit, P_a is the PV array output power

after reconstruction, P_b is the PV array output power before reconstruction, and M_e is the electricity price. The target is to peruse the maximum value for M_p.

max $$M_p = M_2 - M_1 \tag{4.11}$$

subject to: $$M_1 = \left(T_{st}/5\right) * M_s \tag{4.12}$$

$$M_2 = M_e * \left(P_a - P_b\right) * 8 * 365/1000 \tag{4.13}$$

and equations (4.8)-(4.10).

4.4. Simulation and Case Studies

Take 2019 as a benchmark. Taking China, the United States, the United Kingdom, and Turkey as examples, it is verified whether the topology reconstruction method of PV array can truly obtain better economic benefits. The detailed information is shown as presented in Table 4-1.

TABLE 4-1 ELECTRICITY PRICE AND LABOR REMUNERATION IN 2019

Country	Electricity prices ($/ KWH)	The average salary ($/ hour)	handling cost per swapping ($/time)
China	0.084	7.4	5.55
America	0.125	16	12
Britain	0.256	17.2	12.9
Turkey	0.17	3.01	2.26

To demonstrate the validity of the proposed algorithm, a number of PV arrays with different sizes will be evaluated on 5 × 5 and 7 × 20 PV arrays. A commercial 300 W PV module is considered in the simulation. The maximum power outputs from these PV configurations, both before and after arrangements, are determined by employing a PV array model constructed in Python, which was employed to carry out the calculations, and the corresponding computing times for a 7 × 20 PV array was arranged. Our experimental environment is as follows: Intel(R) Core (7M) i7-8565u CPU @1.80GHz/ Windows 10 / 8 GB / 512gb SSD / UHD 620.

The maximum output power in a healthy module is set as 1 p.u. (STC), where standard test conditions represent 1000 W/m^2 irradiance at 25 °C module temperature. A typical large-scale non-uniform aging PV array is employed as a testing branch, which is presented in the upside in Table 4-2 ~Table 4-6, in which each number stands for the maximum output power due to aging. In each string, PV modules are in series connection, and all the strings are parallel connected, which is the typical connection method for commercial PV arrays. The downside of Table 4-2 is the result of reconfiguration with the proposed algorithm considering the manpower cost and electricity price in China. The downside of Table 4-3 is the result of reconfiguration with the proposed algorithm considering the manpower cost and electricity price in the USA. The downside of Table 4-4 is the result of reconfiguration with the proposed algorithm considering the manpower cost and electricity price in the UK. The downside of Table 4-5 is the result of reconfiguration with the proposed algorithm considering the manpower cost and electricity price in Turkey. The downside of Table 4-6 is the result of reconfiguration that only considers additional electric revenue profit.

TABLE 4-2 PV ARRAY BEFORE ARRANGEMENT FOR SECOND CASE IN CHINA

Before																			
0.7 p.u	0.8 p.u	0.7 p.u	0.5 p.u	0.4 p.u	0.8 p.u	0.5 p.u	0.7 p.u	0.4 p.u	0.4 p.u	0.7 p.u	0.8 p.u	0.7 p.u	0.5 p.u	0.4 p.u	0.8 p.u	0.5 p.u	0.7 p.u	0.4 p.u	0.3 p.u
0.6 p.u	0.7 p.u	0.6 p.u	0.7 p.u	0.7 p.u	0.7 p.u	0.4 p.u	0.7 p.u	0.6 p.u	0.6 p.u	0.6 p.u	0.7 p.u	0.6 p.u	0.7 p.u	0.7 p.u	0.7 p.u	0.4 p.u	0.7 p.u	0.6 p.u	0.6 p.u
0.7 p.u	0.7 p.u	0.7 p.u	0.8 p.u	0.6 p.u	0.6 p.u	0.8 p.u	0.5 p.u	0.7 p.u	0.6 p.u	0.7 p.u	0.7 p.u	0.7 p.u	0.8 p.u	0.6 p.u	0.6 p.u	0.8 p.u	0.5 p.u	0.7 p.u	0.6 p.u
0.8 p.u	0.6 p.u	0.7 p.u	0.7 p.u	0.6 p.u	0.7 p.u	0.7 p.u	0.8 p.u	0.5 p.u	0.5 p.u	0.8 p.u	0.6 p.u	0.7 p.u	0.7 p.u	0.7 p.u	0.7 p.u	0.7 p.u	0.8 p.u	0.5 p.u	0.7 p.u
0.8 p.u	0.8 p.u	0.8 p.u	0.6 p.u	0.5 p.u	0.5 p.u	0.7 p.u	0.5 p.u	0.6 p.u	0.5 p.u	0.8 p.u	0.8 p.u	0.7 p.u	0.6 p.u	0.5 p.u	0.5 p.u	0.7 p.u	0.5 p.u	0.6 p.u	0.5 p.u
0.7 p.u	0.9 p.u	0.8 p.u	0.7 p.u	0.6 p.u	0.5 p.u	0.6 p.u	0.9 p.u	0.7 p.u	0.5 p.u	0.7 p.u	0.9 p.u	0.8 p.u	0.7 p.u	0.6 p.u	0.5 p.u	0.6 p.u	0.9 p.u	0.7 p.u	0.5 p.u
0.9 p.u	0.9 p.u	0.8 p.u	0.7 p.u	0.6 p.u	0.6 p.u	0.6 p.u	0.9 p.u	0.7 p.u	0.9 p.u	0.7 p.u	0.8 p.u	0.8 p.u	0.7 p.u	0.9 p.u	0.6 p.u	0.6 p.u	0.9 p.u	0.8 p.u	0.7 p.u

After

0.7 p.u	0.8 p.u	0.6 p.u	0.5 p.u	0.5 p.u	0.5 p.u	0.5 p.u	0.5 p.u	0.5 p.u	0.5 p.u	0.5 p.u	0.5 p.u	0.5 p.u	0.5 p.u	0.5 p.u	0.5 p.u	0.5 p.u	0.4 p.u	0.3 p.u
0.6 p.u	0.7 p.u	0.6 p.u	0.7 p.u	0.7 p.u	0.7 p.u	0.7 p.u	0.6 p.u	0.7 p.u	0.6 p.u	0.7 p.u	0.6 p.u	0.6 p.u	0.7 p.u	0.6 p.u	0.4 p.u	0.4 p.u	0.6 p.u	0.6 p.u	0.6 p.u
0.7 p.u	0.7 p.u	0.7 p.u	0.8 p.u	0.7 p.u	0.7 p.u	0.7 p.u	0.8 p.u	0.7 p.u	0.7 p.u	0.8 p.u	0.7 p.u	0.7 p.u	0.7 p.u	0.7 p.u	0.7 p.u	0.7 p.u	0.7 p.u	0.5 p.u	0.5 p.u
0.7 p.u	0.7 p.u	0.7 p.u	0.7 p.u	0.7 p.u	0.7 p.u	0.7 p.u	0.7 p.u	0.7 p.u	0.7 p.u	0.7 p.u	0.7 p.u	0.7 p.u	0.7 p.u	0.7 p.u	0.7 p.u	0.7 p.u	0.7 p.u	0.5 p.u	0.4 p.u
0.6 p.u	0.7 p.u	0.6 p.u	0.6 p.u	0.9 p.u	0.7 p.u	0.8 p.u	0.7 p.u	0.8 p.u	0.8 p.u	0.8 p.u	0.8 p.u	0.8 p.u	0.8 p.u	0.8 p.u	0.7 p.u	0.8 p.u	0.7 p.u	0.5 p.u	0.5 p.u
0.6 p.u	0.6 p.u	0.8 p.u	0.6 p.u	0.6 p.u	0.6 p.u	0.6 p.u	0.7 p.u	0.6 p.u	0.6 p.u	0.6 p.u	0.6 p.u	0.6 p.u	0.6 p.u	0.6 p.u	0.6 p.u	0.6 p.u	0.6 p.u	0.5 p.u	0.4 p.u
0.9 p.u	0.9 p.u	0.8 p.u	0.5 p.u	0.9 p.u	0.9 p.u	0.9 p.u	0.9 p.u	0.8 p.u	0.9 p.u	0.9 p.u	0.8 p.u	0.8 p.u	0.8 p.u	0.8 p.u	0.8 p.u	0.8 p.u	0.9 p.u	0.8 p.u	0.4 p.u

TABLE 4-3 PV ARRAY BEFORE ARRANGEMENT FOR SECOND CASE IN USA

Before

0.7 p.u	0.8 p.u	0.7 p.u	0.5 p.u	0.4 p.u	0.8 p.u	0.5 p.u	0.7 p.u	0.4 p.u	0.4 p.u	0.7 p.u	0.8 p.u	0.7 p.u	0.5 p.u	0.4 p.u	0.8 p.u	0.5 p.u	0.7 p.u	0.4 p.u	0.3 p.u
0.6 p.u	0.7 p.u	0.6 p.u	0.7 p.u	0.7 p.u	0.7 p.u	0.4 p.u	0.7 p.u	0.6 p.u	0.6 p.u	0.6 p.u	0.7 p.u	0.6 p.u	0.7 p.u	0.7 p.u	0.7 p.u	0.4 p.u	0.7 p.u	0.6 p.u	0.6 p.u
0.7 p.u	0.7 p.u	0.7 p.u	0.8 p.u	0.6 p.u	0.6 p.u	0.8 p.u	0.5 p.u	0.7 p.u	0.6 p.u	0.7 p.u	0.7 p.u	0.7 p.u	0.8 p.u	0.6 p.u	0.6 p.u	0.8 p.u	0.5 p.u	0.7 p.u	0.6 p.u
0.8 p.u	0.6 p.u	0.7 p.u	0.7 p.u	0.6 p.u	0.7 p.u	0.7 p.u	0.8 p.u	0.5 p.u	0.5 p.u	0.8 p.u	0.6 p.u	0.7 p.u	0.7 p.u	0.7 p.u	0.7 p.u	0.7 p.u	0.8 p.u	0.5 p.u	0.7 p.u
0.8 p.u	0.8 p.u	0.8 p.u	0.6 p.u	0.5 p.u	0.5 p.u	0.7 p.u	0.5 p.u	0.6 p.u	0.5 p.u	0.8 p.u	0.8 p.u	0.7 p.u	0.6 p.u	0.5 p.u	0.5 p.u	0.7 p.u	0.5 p.u	0.6 p.u	0.5 p.u

0.7	0.9	0.8	0.7	0.6	0.5	0.6	0.9	0.7	0.5	0.7	0.9	0.8	0.7	0.6	0.5	0.6	0.9	0.7	0.5
p.u	p.u	p.u	p.u	p.u	p.u	p.u	p.u	p.u	p.u	p.u	p.u	p.u	p.u	p.u	p.u	p.u	p.u	p.u	p.u
0.9	0.9	0.8	0.7	0.6	0.6	0.6	0.9	0.7	0.9	0.7	0.8	0.8	0.7	0.9	0.6	0.6	0.9	0.8	0.7
p.u	p.u	p.u	p.u	p.u	p.u	p.u	p.u	p.u	p.u	p.u	p.u	p.u	p.u	p.u	p.u	p.u	p.u	p.u	p.u

After

0.6	0.5	0.8	0.4	0.4	0.5	0.5	0.5	0.5	0.5	0.5	0.5	0.5	0.5	0.5	0.5	0.5	0.5	0.4	0.3
p.u	p.u	p.u	p.u	p.u	p.u	p.u	p.u	p.u	p.u	p.u	p.u	p.u	p.u	p.u	p.u	p.u	p.u	p.u	p.u
0.6	0.7	0.6	0.9	0.7	0.7	0.7	0.4	0.8	0.8	0.8	0.8	0.8	0.8	0.8	0.8	0.7	0.7	0.8	0.5
p.u	p.u	p.u	p.u	p.u	p.u	p.u	p.u	p.u	p.u	p.u	p.u	p.u	p.u	p.u	p.u	p.u	p.u	p.u	p.u
0.7	0.7	0.7	0.7	0.7	0.7	0.7	0.7	0.7	0.7	0.7	0.7	0.7	0.7	0.7	0.7	0.7	0.7	0.5	0.4
p.u	p.u	p.u	p.u	p.u	p.u	p.u	p.u	p.u	p.u	p.u	p.u	p.u	p.u	p.u	p.u	p.u	p.u	p.u	p.u
0.8	0.8	0.8	0.7	0.7	0.7	0.7	0.7	0.7	0.7	0.7	0.7	0.7	0.7	0.7	0.7	0.7	0.7	0.5	0.5
p.u	p.u	p.u	p.u	p.u	p.u	p.u	p.u	p.u	p.u	p.u	p.u	p.u	p.u	p.u	p.u	p.u	p.u	p.u	p.u
0.7	0.7	0.7	0.7	0.7	0.7	0.7	0.6	0.7	0.6	0.6	0.6	0.6	0.7	0.6	0.6	0.6	0.6	0.5	0.4
p.u	p.u	p.u	p.u	p.u	p.u	p.u	p.u	p.u	p.u	p.u	p.u	p.u	p.u	p.u	p.u	p.u	p.u	p.u	p.u
0.7	0.6	0.8	0.6	0.6	0.6	0.6	0.6	0.6	0.6	0.6	0.6	0.6	0.6	0.6	0.6	0.6	0.6	0.4	0.5
p.u	p.u	p.u	p.u	p.u	p.u	p.u	p.u	p.u	p.u	p.u	p.u	p.u	p.u	p.u	p.u	p.u	p.u	p.u	p.u
0.9	0.9	0.8	0.8	0.6	0.9	0.9	0.9	0.9	0.9	0.8	0.8	0.8	0.8	0.9	0.8	0.8	0.9	0.8	0.5
p.u	p.u	p.u	p.u	p.u	p.u	p.u	p.u	p.u	p.u	p.u	p.u	p.u	p.u	p.u	p.u	p.u	p.u	p.u	p.u

TABLE 4-4 PV ARRAY BEFORE ARRANGEMENT FOR SECOND CASE IN UK

Before

0.7	0.8	0.7	0.5	0.4	0.8	0.5	0.7	0.4	0.4	0.7	0.8	0.7	0.5	0.4	0.8	0.5	0.7	0.4	0.3
p.u	p.u	p.u	p.u	p.u	p.u	p.u	p.u	p.u	p.u	p.u	p.u	p.u	p.u	p.u	p.u	p.u	p.u	p.u	p.u
0.6	0.7	0.6	0.7	0.7	0.7	0.4	0.7	0.6	0.6	0.6	0.7	0.6	0.7	0.7	0.7	0.4	0.7	0.6	0.6
p.u	p.u	p.u	p.u	p.u	p.u	p.u	p.u	p.u	p.u	p.u	p.u	p.u	p.u	p.u	p.u	p.u	p.u	p.u	p.u
0.7	0.7	0.7	0.8	0.6	0.6	0.8	0.5	0.7	0.6	0.7	0.7	0.7	0.8	0.6	0.6	0.8	0.5	0.7	0.6
p.u	p.u	p.u	p.u	p.u	p.u	p.u	p.u	p.u	p.u	p.u	p.u	p.u	p.u	p.u	p.u	p.u	p.u	p.u	p.u

0.8	0.6	0.7	0.7	0.6	0.7	0.7	0.8	0.5	0.5	0.8	0.6	0.7	0.7	0.7	0.7	0.7	0.8	0.5	0.7
p.u	p.u	p.u	p.u	p.u	p.u	p.u	p.u	p.u	p.u	p.u	p.u	p.u	p.u	p.u	p.u	p.u	p.u	p.u	p.u
0.8	0.8	0.8	0.6	0.5	0.5	0.7	0.5	0.6	0.5	0.8	0.8	0.7	0.6	0.5	0.5	0.7	0.5	0.6	0.5
p.u	p.u	p.u	p.u	p.u	p.u	p.u	p.u	p.u	p.u	p.u	p.u	p.u	p.u	p.u	p.u	p.u	p.u	p.u	p.u
0.7	0.9	0.8	0.7	0.6	0.5	0.6	0.9	0.7	0.5	0.7	0.9	0.8	0.7	0.6	0.5	0.6	0.9	0.7	0.5
p.u	p.u	p.u	p.u	p.u	p.u	p.u	p.u	p.u	p.u	p.u	p.u	p.u	p.u	p.u	p.u	p.u	p.u	p.u	p.u
0.9	0.9	0.8	0.7	0.6	0.6	0.6	0.9	0.7	0.9	0.7	0.8	0.8	0.7	0.9	0.6	0.6	0.9	0.8	0.7
p.u	p.u	p.u	p.u	p.u	p.u	p.u	p.u	p.u	p.u	p.u	p.u	p.u	p.u	p.u	p.u	p.u	p.u	p.u	p.u

After

0.6	0.6	0.8	0.5	0.5	0.5	0.5	0.5	0.5	0.5	0.5	0.5	0.5	0.5	0.5	0.5	0.5	0.5	0.4	0.3
p.u	p.u	p.u	p.u	p.u	p.u	p.u	p.u	p.u	p.u	p.u	p.u	p.u	p.u	p.u	p.u	p.u	p.u	p.u	p.u
0.9	0.6	0.6	0.7	0.8	0.8	0.8	0.7	0.8	0.8	0.7	0.8	0.8	0.8	0.8	0.7	0.7	0.7	0.5	0.5
p.u	p.u	p.u	p.u	p.u	p.u	p.u	p.u	p.u	p.u	p.u	p.u	p.u	p.u	p.u	p.u	p.u	p.u	p.u	p.u
0.7	0.7	0.7	0.8	0.7	0.7	0.7	0.8	0.7	0.7	0.8	0.7	0.7	0.7	0.7	0.7	0.7	0.7	0.5	0.5
p.u	p.u	p.u	p.u	p.u	p.u	p.u	p.u	p.u	p.u	p.u	p.u	p.u	p.u	p.u	p.u	p.u	p.u	p.u	p.u
0.7	0.7	0.7	0.7	0.7	0.7	0.7	0.7	0.7	0.7	0.7	0.7	0.7	0.7	0.7	0.7	0.7	0.7	0.5	0.4
p.u	p.u	p.u	p.u	p.u	p.u	p.u	p.u	p.u	p.u	p.u	p.u	p.u	p.u	p.u	p.u	p.u	p.u	p.u	p.u
0.7	0.7	0.7	0.7	0.7	0.7	0.7	0.6	0.7	0.6	0.6	0.6	0.6	0.6	0.6	0.6	0.6	0.6	0.4	0.4
p.u	p.u	p.u	p.u	p.u	p.u	p.u	p.u	p.u	p.u	p.u	p.u	p.u	p.u	p.u	p.u	p.u	p.u	p.u	p.u
0.6	0.6	0.6	0.6	0.6	0.6	0.6	0.7	0.6	0.8	0.6	0.6	0.6	0.6	0.6	0.6	0.6	0.6	0.4	0.4
p.u	p.u	p.u	p.u	p.u	p.u	p.u	p.u	p.u	p.u	p.u	p.u	p.u	p.u	p.u	p.u	p.u	p.u	p.u	p.u
0.8	0.9	0.9	0.9	0.9	0.9	0.9	0.9	0.9	0.9	0.8	0.8	0.8	0.8	0.8	0.8	0.8	0.8	0.5	0.4
p.u	p.u	p.u	p.u	p.u	p.u	p.u	p.u	p.u	p.u	p.u	p.u	p.u	p.u	p.u	p.u	p.u	p.u	p.u	p.u

TABLE 4-5 PV ARRAY BEFORE ARRANGEMENT FOR SECOND CASE IN TURKEY

Before

0.7	0.8	0.7	0.5	0.4	0.8	0.5	0.7	0.4	0.4	0.7	0.8	0.7	0.5	0.4	0.8	0.5	0.7	0.4	0.3
p.u	p.u	p.u	p.u	p.u	p.u	p.u	p.u	p.u	p.u	p.u	p.u	p.u	p.u	p.u	p.u	p.u	p.u	p.u	p.u

0.6 p.u	0.7 p.u	0.6 p.u	0.7 p.u	0.7 p.u	0.7 p.u	0.4 p.u	0.7 p.u	0.6 p.u	0.6 p.u	0.6 p.u	0.7 p.u	0.6 p.u	0.7 p.u	0.7 p.u	0.7 p.u	0.4 p.u	0.7 p.u	0.6 p.u	0.6 p.u
0.7 p.u	0.7 p.u	0.7 p.u	0.8 p.u	0.6 p.u	0.6 p.u	0.8 p.u	0.5 p.u	0.7 p.u	0.6 p.u	0.7 p.u	0.7 p.u	0.7 p.u	0.8 p.u	0.6 p.u	0.6 p.u	0.8 p.u	0.5 p.u	0.7 p.u	0.6 p.u
0.8 p.u	0.6 p.u	0.7 p.u	0.7 p.u	0.6 p.u	0.7 p.u	0.7 p.u	0.8 p.u	0.5 p.u	0.5 p.u	0.8 p.u	0.6 p.u	0.7 p.u	0.7 p.u	0.7 p.u	0.7 p.u	0.7 p.u	0.8 p.u	0.5 p.u	0.7 p.u
0.8 p.u	0.8 p.u	0.8 p.u	0.6 p.u	0.5 p.u	0.5 p.u	0.7 p.u	0.5 p.u	0.6 p.u	0.5 p.u	0.8 p.u	0.8 p.u	0.7 p.u	0.6 p.u	0.5 p.u	0.5 p.u	0.7 p.u	0.5 p.u	0.6 p.u	0.5 p.u
0.7 p.u	0.9 p.u	0.8 p.u	0.7 p.u	0.6 p.u	0.5 p.u	0.6 p.u	0.9 p.u	0.7 p.u	0.5 p.u	0.7 p.u	0.9 p.u	0.8 p.u	0.7 p.u	0.6 p.u	0.5 p.u	0.6 p.u	0.9 p.u	0.7 p.u	0.5 p.u
0.9 p.u	0.9 p.u	0.8 p.u	0.7 p.u	0.6 p.u	0.6 p.u	0.6 p.u	0.9 p.u	0.7 p.u	0.9 p.u	0.7 p.u	0.8 p.u	0.8 p.u	0.7 p.u	0.9 p.u	0.6 p.u	0.6 p.u	0.9 p.u	0.8 p.u	0.7 p.u

After

0.6 p.u	0.6 p.u	0.6 p.u	0.5 p.u	0.5 p.u	0.5 p.u	0.5 p.u	0.5 p.u	0.5 p.u	0.5 p.u	0.5 p.u	0.5 p.u	0.5 p.u	0.5 p.u	0.5 p.u	0.5 p.u	0.5 p.u	0.5 p.u	0.4 p.u	0.3 p.u
0.7 p.u	0.7 p.u	0.7 p.u	0.7 p.u	0.7 p.u	0.7 p.u	0.7 p.u	0.7 p.u	0.7 p.u	0.7 p.u	0.7 p.u	0.7 p.u	0.7 p.u	0.7 p.u	0.7 p.u	0.7 p.u	0.7 p.u	0.7 p.u	0.5 p.u	0.5 p.u
0.8 p.u	0.8 p.u	0.8 p.u	0.8 p.u	0.8 p.u	0.8 p.u	0.8 p.u	0.8 p.u	0.8 p.u	0.8 p.u	0.8 p.u	0.8 p.u	0.7 p.u	0.8 p.u	0.8 p.u	0.7 p.u	0.8 p.u	0.5 p.u	0.7 p.u	0.5 p.u
0.7 p.u	0.7 p.u	0.7 p.u	0.7 p.u	0.7 p.u	0.7 p.u	0.7 p.u	0.7 p.u	0.7 p.u	0.7 p.u	0.7 p.u	0.7 p.u	0.7 p.u	0.7 p.u	0.7 p.u	0.7 p.u	0.7 p.u	0.7 p.u	0.4 p.u	0.4 p.u
0.7 p.u	0.7 p.u	0.7 p.u	0.7 p.u	0.7 p.u	0.7 p.u	0.7 p.u	0.7 p.u	0.7 p.u	0.6 p.u	0.6 p.u	0.6 p.u	0.6 p.u	0.6 p.u	0.6 p.u	0.6 p.u	0.6 p.u	0.6 p.u	0.4 p.u	0.4 p.u
0.6 p.u	0.6 p.u	0.6 p.u	0.6 p.u	0.6 p.u	0.6 p.u	0.6 p.u	0.6 p.u	0.6 p.u	0.6 p.u	0.6 p.u	0.6 p.u	0.6 p.u	0.6 p.u	0.6 p.u	0.6 p.u	0.6 p.u	0.6 p.u	0.4 p.u	0.4 p.u
0.9 p.u	0.9 p.u	0.8 p.u	0.9 p.u	0.9 p.u	0.9 p.u	0.9 p.u	0.9 p.u	0.9 p.u	0.9 p.u	0.8 p.u	0.8 p.u	0.8 p.u	0.8 p.u	0.8 p.u	0.8 p.u	0.8 p.u	0.9 p.u	0.5 p.u	0.5 p.u

TABLE 4-6 PV ARRAY BEFORE ARRANGEMENT FOR SECOND CASE IN SAUDI

Before

0.7	0.8	0.7	0.5	0.4	0.8	0.5	0.7	0.4	0.4	0.7	0.8	0.7	0.5	0.4	0.8	0.5	0.7	0.4	0.3
p.u	p.u	p.u	p.u	p.u	p.u	p.u	p.u	p.u	p.u	p.u	p.u	p.u	p.u	p.u	p.u	p.u	p.u	p.u	p.u
0.6	0.7	0.6	0.7	0.7	0.7	0.4	0.7	0.6	0.6	0.6	0.7	0.6	0.7	0.7	0.7	0.4	0.7	0.6	0.6
p.u	p.u	p.u	p.u	p.u	p.u	p.u	p.u	p.u	p.u	p.u	p.u	p.u	p.u	p.u	p.u	p.u	p.u	p.u	p.u
0.7	0.7	0.7	0.8	0.6	0.6	0.8	0.5	0.7	0.6	0.7	0.7	0.7	0.8	0.6	0.6	0.8	0.5	0.7	0.6
p.u	p.u	p.u	p.u	p.u	p.u	p.u	p.u	p.u	p.u	p.u	p.u	p.u	p.u	p.u	p.u	p.u	p.u	p.u	p.u
0.8	0.6	0.7	0.7	0.6	0.7	0.7	0.8	0.5	0.5	0.8	0.6	0.7	0.7	0.7	0.7	0.7	0.8	0.5	0.7
p.u	p.u	p.u	p.u	p.u	p.u	p.u	p.u	p.u	p.u	p.u	p.u	p.u	p.u	p.u	p.u	p.u	p.u	p.u	p.u
0.8	0.8	0.8	0.6	0.5	0.5	0.7	0.5	0.6	0.5	0.8	0.8	0.7	0.6	0.5	0.5	0.7	0.5	0.6	0.5
p.u	p.u	p.u	p.u	p.u	p.u	p.u	p.u	p.u	p.u	p.u	p.u	p.u	p.u	p.u	p.u	p.u	p.u	p.u	p.u
0.7	0.9	0.8	0.7	0.6	0.5	0.6	0.9	0.7	0.5	0.7	0.9	0.8	0.7	0.6	0.5	0.6	0.9	0.7	0.5
p.u	p.u	p.u	p.u	p.u	p.u	p.u	p.u	p.u	p.u	p.u	p.u	p.u	p.u	p.u	p.u	p.u	p.u	p.u	p.u
0.9	0.9	0.8	0.7	0.6	0.6	0.6	0.9	0.7	0.9	0.7	0.8	0.8	0.7	0.9	0.6	0.6	0.9	0.8	0.7
p.u	p.u	p.u	p.u	p.u	p.u	p.u	p.u	p.u	p.u	p.u	p.u	p.u	p.u	p.u	p.u	p.u	p.u	p.u	p.u

After

0.9	0.9	0.9	0.9	0.9	0.9	0.9	0.9	0.9	0.9	0.8	0.8	0.8	0.8	0.8	0.8	0.8	0.9	0.5	0.5
p.u	p.u	p.u	p.u	p.u	p.u	p.u	p.u	p.u	p.u	p.u	p.u	p.u	p.u	p.u	p.u	p.u	p.u	p.u	p.u
0.8	0.8	0.8	0.8	0.8	0.8	0.8	0.8	0.8	0.8	0.8	0.8	0.8	0.8	0.8	0.7	0.7	0.7	0.5	0.5
p.u	p.u	p.u	p.u	p.u	p.u	p.u	p.u	p.u	p.u	p.u	p.u	p.u	p.u	p.u	p.u	p.u	p.u	p.u	p.u
0.7	0.7	0.7	0.7	0.7	0.7	0.7	0.7	0.7	0.7	0.7	0.7	0.7	0.7	0.7	0.7	0.7	0.7	0.5	0.5
p.u	p.u	p.u	p.u	p.u	p.u	p.u	p.u	p.u	p.u	p.u	p.u	p.u	p.u	p.u	p.u	p.u	p.u	p.u	p.u
0.7	0.7	0.7	0.7	0.7	0.7	0.7	0.7	0.7	0.7	0.7	0.7	0.7	0.7	0.7	0.7	0.7	0.7	0.4	0.4
p.u	p.u	p.u	p.u	p.u	p.u	p.u	p.u	p.u	p.u	p.u	p.u	p.u	p.u	p.u	p.u	p.u	p.u	p.u	p.u
0.7	0.7	0.7	0.7	0.7	0.7	0.7	0.7	0.7	0.6	0.6	0.6	0.6	0.6	0.6	0.6	0.6	0.6	0.4	0.4
p.u	p.u	p.u	p.u	p.u	p.u	p.u	p.u	p.u	p.u	p.u	p.u	p.u	p.u	p.u	p.u	p.u	p.u	p.u	p.u

0.6 p.u	0.6 p.u	0.6 p.u	0.6 p.u	0.6 p.u	0.6 p.u	0.6 p.u	0.6 p.u	0.6 p.u	0.6 p.u	0.6 p.u	0.6 p.u	0.6 p.u	0.6 p.u	0.6 p.u	0.6 p.u	0.6 p.u	0.6 p.u	0.4 p.u	0.4 p.u
0.6 p.u	0.6 p.u	0.6 p.u	0.5 p.u	0.5 p.u	0.5 p.u	0.5 p.u	0.5 p.u	0.5 p.u	0.5 p.u	0.5 p.u	0.5 p.u	0.5 p.u	0.5 p.u	0.5 p.u	0.5 p.u	0.5 p.u	0.5 p.u	0.4 p.u	0.3 p.u

Table 4-2 shows the simulation results that consider the electricity price and manpower cost in China, in which eighty manual swapping times are required. Without considering the maximum economic benefit, the additional electric revenue profit (M_2) is \$1192.06, and the corresponding labor cost (M_1) is \$693.75. When considering the maximum economic benefit, the additional electric revenue profit (M_2) is \$1059.61, and the corresponding labor cost (M_1) is \$330. Comparing those two reconfigurations, although the additional electric revenue profit is decreased by 11.1% in the proposed method, the labor cost (M_1) is decreased by 52.4%, and the pure profit of the offline maintenance increases by 46.4% due to the lower labor cost.

Table 4-3 displays the simulation results that consider the electricity price and manpower cost in the USA, in which eighty manual swapping times are required. Without considering the maximum economic benefit, the additional electric revenue profit (M_2) is \$1773.90, and the corresponding labor cost (M_1) is \$1500.00. It is clear that the additional electric revenue profit and labor cost are higher than that in China due to the high electricity price and labor cost. When considering the maximum economic benefit, the additional electric revenue profit (M_2) is \$1379.70, the corresponding labor cost (M_1) is \$600. Comparing those two reconfigurations, although the additional electric revenue profit is decreased by 22.2% in the proposed method, the labor cost (M_1) is decreased by 60%, and the pure profit of the offline maintenance is increased by 191.9% due to the lower labor cost.

The UK case is similar to the USA one in electrifying price and labor cost. Table 4-4 shows the simulation results that consider the electricity price and manpower cost in the UK, in which eighty manual swapping times are required. Without considering the maximum economic benefit, the additional electric revenue profit (M_2) is \$3632.95, and the corresponding labor cost (M_1) is \$1612.50. It is clear that the additional electric revenue profit and labor cost are higher than in China due to the high electricity price and labor cost. Considering the maximum economic benefit, the additional electric revenue profit (M_2) is \$3229.29, the corresponding labor cost (M_1) is \$709.50. Comparing those two reconfigurations, although the additional electric revenue profit is decreased by 11% in the proposed method, the labor cost (M_1) is decreased by 56%, and the pure profit of the offline maintained is increased by 24.7% due to the lower labor cost.

Table 4-5 shows the simulation results that consider the electricity price and manpower cost in Turkey, in which eighty manual swapping times are required. Without considering the maximum economic benefit, the additional electric revenue profit (M_2) is \$2412.50, and the corresponding labor cost (M_1) is \$282.50. Considering the maximum economic benefit, the additional electric revenue profit (M_2) is \$2375.50, and the corresponding labor cost (M_1) is \$213.75. Comparing those two reconfigurations, although the additional electric revenue profit is decreased by 1.5% in the proposed method, the labor cost (M_1) is decreased by 24%, and the pure profit of the offline maintenance is increased by 1.4% due to the lower labor cost. Due to the low cost of the manpower and high electricity price in Turkey, the proposed method can only improve the economic benefit by 1.4% by the proposed method.

According to the calculation results from Table 4-7 and Table 4-8, in the countries with high manpower cost and low electricity price, the proposed algorithm can decrease the cost of the offline reconfiguration by decreasing the swapping times, and the total profit can increase dramatically. In the countries with low manpower cost and high electricity price, although the proposed algorithm can decrease the cost of the manpower, the corresponding additional electric revenue profit is decreased as well. Therefore, there is no obvious profit increment.

TABLE 4-7 ECONOMIC BENEFIT ANALYSIS CONSIDERING THE MINIMUM HANDLING TIMES

Country	M_2(\$)	M_1(\$)	M_p(\$)
China	1059.61	330.00	729.61
USA	1379.70	600.00	779.70
UK	3229.29	709.50	2520.10
Turkey	2375.50	213.75	2161.75

TABLE 4-8 ECONOMIC BENEFIT ANALYSIS WITHOUT CONSIDERING THE MINIMUM HANDLING TIMES

Country	M_2 (\$)	M_1 (\$)	M_p (\$)
China	1192.06	693.75	498.31
USA	1773.90	1500.00	273.90

UK	3632.95	1612.50	2020.45
Turkey	2412.50	282.50	2130.00

4.5 Summary

Non-uniform aging of PV modules is a long-lasting challenge for large large-scale PV arrays, which not only decreases the output power of the PV array but also damages the PV modules if left untreated. Without rearranging non-uniformly aged PV arrays, typical online global-MPPT schemes can only track a compromised maximum rather than its maximum potential power of the non-uniform aging of PV array. This paper has proposed a new PV array reconfiguration strategy considering the lowest cost of manpower and electricity price. The manpower cost and electricity price in the USA, China, UK, and Turkey are considered in the paper to investigate different reconfigurations. A 7x20 array is employed to verify the proposed reconfirmation algorithm. Due to the difference of the manpower and electrify price in different countries, for a 7x20 PV array with the same non-uniform aging, there is about 46.4% increment in the profit for the application scenario in China; there is about 191.9% increment in profit in USA application scenario; there is about 24.7% profit in UK application scenario; there is about 1.4% increment in profit in Turkey application scenario. The proposed method also can be used in other countries to maintain the aged PV arrays. For the countries with high electricity price and low labor cost, such as South Africa, Turkey, etc., the proposed algorithm may not have a clear profit increment. The proposed algorithm will give more finical increment in the low electricity price and high labor cost countries, such as the USA, UK, Saudi Arabia.

Chapter 5 A New Strategy of PV Fire Prevention in Large-Scale PV Arrays: A Hybrid PV Array of Monofacial and Bifacial PV Modules

5.1 Introduction

As one of the most popular renewable power generation technologies, solar photovoltaics (PVs) have a promising perspective. The capacity of PV installation reached 505 GW in 2018 [152]. A steady increase was predicted, reaching 15% energy generation by 2024 in the world market [153]. The improvement of power generation efficiency can be addressed by new PV technologies as well as the optimization of row-to-row spacing. With regards to the new technology, the concept of bifacial photovoltaic (bPV) modules has been proposed by Luque [155]. Due to the simultaneous absorption of direct photon and albedo photon, bifacial PV modules can lead to a 50 % increase in power generation [156]. In addition, an optimal row spacing can potentially increase the annual power generation of PV arrays by 4% [157]. However, with the increasing capacity of PVs, the fire risks should also be carefully addressed. In 2009, the PV arrays of 1826 PV modules with a total generation capacity of 383 kW were damaged in a fire accident in California, USA [8]. In Germany, there were 430 fire cases reported by 2013 [158]. These fire accidents not only affected the local solar power generation but also damaged the associated residential or commercial properties.

At present, all PV heat transfer models are based on monofacial photovoltaic (mPV) modules analysis [159, 160]. The mPVs are encapsulated by ethylene-vinyl acetate (EVA), polyethylene terephthalate (PET), and other organic matters. The melting points of EVA and PET are 75 °C and 270 °C, respectively. When the mPV cells are working in poor conditions such as shading, aging, etc., the cell power is converted into heat. The temperature of the back sheet of PV panels can reach 347 °C in such situations and are prone to ignite [161]. Tewarson [162] experimentally identified a number of flammability parameters, which are the main materials of PV modules. The causes for the PV panel fire accidents can be broadly divided into (1) DC arc due to poor assembling quality of PV panels, (2) hot spot effect, and (3) the aging of PV system cables caused by poor drainage systems. Based on [163], Liao et al. [7] experimentally found that PV panels released 4.79 kW, 13.07 kW, 16.63 kW, 18.17 kW energy under the radiation conditions of 15 kW/m^2, 20 kW/m^2, 30 kW/m^2, 40 kW/m^2, respectively.

PV panel fires can be initiated by either self-ignition or accidental ignition [164]. In order to avoid self-ignition of PV panels, their ambient radiation and temperature need to be carefully monitored. Dust deposition not only reduces the efficiency of the power generation but also causes fires in severe cases. Compared with mPV modules, the bPV modules are less sensitive to sand and dust deposition. The calculations by Luque et al. [165,166] indicated that the soiling rate of mPV is 7.6 times more than that of bPV, suggesting that mPV is easier to accumulate dust. Meanwhile, when PV panels are affected by dust, the output power is reduced to 17.25% and 12.5% for the mPV modules and bPV modules, respectively. The spacing between PV panels is expected to have a significant influence on the fire spread between them. In order to ensure its power generation efficiency, the row-to-row space of a PV array should be adjusted according to the latitude and the optimal inclination [45]. Among them, considering the albedo of bPVs, Appelbaum [167] measured 20 º and 90 º inclination in the 20 rows bPV array. It was found that when the distance is increased by 1 m, the incident irradiance is increased by 0.98% and 7.9% in the 20 º and 90 º bPV arrays, respectively. These results indicated that the output of bPV is dominated by the inclination angle and row spacing. When the inclination angle is fixed, the larger the row spacing, the higher the output from the PV array. Further research along this direction has also been conducted by Katsaounis et al. [168], who revealed the relation between solar irradiance and cell temperature of bPV modules, as well as Zhang et al. [169], who compared the temperature difference between bPV and mPV under different shading conditions. Since the back of a bPV panel needs to absorb the reflected sunlight, the optimal tilt angle of the bPV can be up to 20 º greater than that of the mPV array [170]. According to the above research results, it is possible to determine the row spacing installation of bPV array under different conditions.

In the present study, a hybrid layout of large-scale PV arrays with bPV modules and mPV modules placed alternatively is proposed to reduce the PV fire risks. As the mPV modules need to be inclined by more degrees to catch fire than the bPV ones, a natural choice would be biased to the use of the bPV nodules from the standpoint of fire prevention. Because compared with bPV modules, mPV is easier to accumulate dust, which is more prone to generating the hot spot effect and aging. However, it is not cost-effective if only bPV modules are adopted as they are expensive. Since the array areas of a mPV module and a bPV module are different, from the perspective of array spacing, the row spacing of a mPV is smaller than that of a bPV. Therefore, the area of a bPV array is higher than that of a mPV array. As a compromise solution, a hybrid structure can be built by intersecting the bPV modules into the mPV ones. Firstly, a thermal model is proposed to relate the ignition temperature, i.e., the temperatures of the EVA and silicon cell, with the ambient temperature of the PV modules. The thermal model, together with thermogravimetric analysis

(TGA), will be used to illustrate the comparison between the flammability of the mPV and bPV materials over the high-temperature range. The results will be used to devise mitigation measures to reduce the fire risks of the arrays. Secondly, a turbulence flow model and a view factor model can determine the minimal distance between the mPV and the bPV modules, which can ensure high profits under safe conditions.

In the following study, Section 5.2 introduces the modeling of the bPV modules, and Section 5.3 compares and analyzes the thermal model of mPV and bPV modules, which include heat transfer and heat conduction. The conditions of ignition temperature of PV modules can be obtained. In Section 5.4, the heat transfer and the cost-benefit among the hybrid PV array are used to define the distance of each type of PV module. In Section 5.5, a set of experiments was designed to verify the accuracy of the thermal models in Section 5.3 and 5.4. Section 5.6 presents the conclusion.

5.2 Modeling of BPV Modules

Different from the traditional mPV with an opaque back sheet, bPV has a transparent back sheet that can absorb sunlight to generate electricity. There are three types of solar crystalline silicon cells of bPV modules: n-type passivated emitter rear totally-diffused (n-PERT), n-type heterojuntion with intrinsic thin layer (n-HIT), and p-type passivated emitter and rear cell (p-PERC) modules. The advantages of n-PERT modules are the superior life expectancy of minority carriers, zero light-induced attenuation effect, adequate low-light response, lower temperature coefficient, 85%~90% double-side gain, and 10%~30% back sheet power gain. The disadvantages are that it requires specialized n-type silicon wafers, and the battery production process is complicated. The advantages of n-HIT modules are high conversion efficiency, high double-side gain, high open-circuit voltage, and satisfactory temperature characteristics. The disadvantages are the high investment in production equipment, strict process requirements, and it requires low-temperature packaging technology. The advantages of p-PERC modules are the simplified production process and high conversion efficiency. However, the disadvantages of p-PERC modules are low conversion efficiency, light-induced attenuation, and low double-side gain. Compared with mPV modules, both the front and back sides of bPV modules can use tempered glass as a protective material, which provides adequate lighting, weather resistance, and high reliability. The power gain on the back can significantly increase the power generation efficiency per unit area. The installation methods are also diversified, which can be vertical and tiltable. Therefore, it can be used in many occasions, such as greenhouses, highway fences, sunrooms, lakes, grasslands, etc. [171]. Although the manufacturing cost of bPV is slightly higher than mPV,

the power generation efficiency is greatly improved, which has attracted extensive attention from scientific researchers.

Currently, the irradiance modeling of bPV is still mainly based on the mPV irradiance model, which takes the sum of the irradiance of the front and back panels into consideration. Either the equatorial coordinate system or the horizon coordinate system can be adopted by the celestial coordinate system of the irradiance model. Generally, the horizontal solar irradiance outside the atmosphere is calculated according to the zenith angle. Then, the hourly solar irradiance is calculated by the hourly clearness coefficient. Finally, the omnidirectional irradiance of the inclined surface of the PV module can be calculated by using the solar incident angle [172-181]. The irradiance model of the bPV back sheet mainly includes scattered irradiance and ground reflection irradiance. According to whether the scattered irradiance is equal in all directions, irradiance can be divided into sky isotropy and sky anisotropy. Due to the impact of the bPV bracket, the backscattered irradiance belongs to the sky anisotropy, and the integral equation of the correction factor for the scattering incident angle can be obtained by using numerical methods [173]. Also, a configuration coefficient is introduced to quantify the complex effect of back shadow. Firstly, the rear surface is divided into 180 equal-area blocks. Then, assuming the shadow area in each block is also equal, the irradiance of each part is corrected by the incident angle multiplied by the corresponding configuration coefficient. Finally, the backscattered irradiance can be obtained by superimposing the corrected irradiance from each block [174]. The high-speed feature of the modeling method makes it suitable for large-scale power generation components. As for small-scale components, the method of distinguishing positions along the length of the part can be used [175-176]. However, this method is of high modeling complexity and computationally expensive.

This section mainly introduces the modeling and characteristics of bPV modules and its power generation under shading, and a bPV irradiance model and a bPV model are established by using MATLAB/SIMULINK. The bPV model proposed in this study is not only prone to operate but also accurate. Initially, by using the declination angle, zenith angle, and incident angle to determine the direct frontal irradiance, scattered irradiance, and ground reflected irradiance, respectively, it will effectively establish a calculation module for total irradiance. Then, build a PV array and compare its horizontal and vertical shadings. The power generation efficiency is needed to be observed under different shading conditions. Finally, an experiment is implemented to verify its accuracy. It is worth noting that the PV modules in the experiment are based on the optimal row spacing. It is necessary to determine the frontal irradiance model initially. The model is a gradual

process. It firstly introduces the solar radiation from outside the atmosphere to the horizontal plane before directing into the inclined plane of the module. According to [177], the calculation formula of the model, parameters such as the declination angle (δ), zenith angle (θ_z), incident angle (solar elevation angle α, azimuth γ_s) are needed, which are shown in (5.1)~(5.4).

$$\delta = 23.45\ sin[2\pi(n+284)/365] \tag{5.1}$$

$$cos\theta_z = cos\varphi cos\delta cos\omega + sin\varphi sin\delta \tag{5.2}$$

$$sin\alpha = sin\varphi sin\delta + cos\varphi cos\delta cos\omega \tag{5.3}$$

$$sin\gamma_s = cos\delta sin\omega / cos\alpha \tag{5.4}$$

where n is one day of a year, φ is the latitude (°), ω is the solar hour angle (°).

Then, the total irradiance (I) model requires the irradiance model outside the atmosphere (I_0) to be established and combined with the solar irradiance coefficient (k_T), and the model can be expressed by (5.5) ~ (5.8).

$$I = \varepsilon I_s cos\theta_z k_T \tag{5.5}$$

$$\varepsilon = 1+0.033cos(2\pi n / 365) \tag{5.6}$$

$$k_T = I / I_0 \tag{5.7}$$

$$I_d / I = \begin{cases} 1-0.09k_T & , \quad k_T \le 0.22; \\ 0.9511-0.1604k_T+4.388{k_T}^2-16.638{k_T}^3 & , \quad 0.22 < k_T \le 0.8; \\ 0.165 & , \quad k_T > 0.8. \end{cases} \tag{5.8}$$

where I_s is the solar constant (W/m^2), which is 1367W/m^2, ε is the earth orbit eccentricity correction factor, I_d is the hourly scattered irradiance (W/m^2).

Finally, by considering the tilt angle of the module, the direct frontal irradiance, scattered irradiance, and ground reflected irradiance of the double-sided module are established, respectively. The three parallel sky anisotropic irradiance models are added together to obtain the total frontal irradiance model [178]. The formulas are shown as:

$$I = I_b + I_d \tag{5.9}$$

$$\frac{I_{b,T}}{I_b} = \frac{sin\delta sin\varphi cos\beta - sin\delta cos\varphi sin\beta cos\gamma + cos\delta cos\varphi cos\beta cos\omega + cos\delta sin\varphi sin\beta cos\gamma cos\omega + cos\delta sin\beta sin\gamma sin\omega}{cos\theta_z} \tag{5.10}$$

$$I_T = (I_b + I_d\, I_b/I_0)\, I_{b,T}/I_b + I_d(1 - I_b/I_0)[1 + (1+cos\,\beta)/2][1 + (I_b/I)^{0.5}\, sin^3(\beta/2)] + I\rho(1 - cos\,\beta)/2 \tag{5.11}$$

where I_b is horizontal plane irradiance (W/m^2), $I_{b,T}$ is the hourly direct irradiance of inclined surface (W/m^2), ρ is ground reflectivity, and β is the tilt angle of PV modules (°).

The backside is equivalent to the inversion of the front side. Namely, the tilt angle is increased by 180° and is input to the backside irradiance (BSI) model. By combining the front side irradiance (FSI) module, the total irradiance will be obtained, as shown in Fig. 5-1. However, the simulation shows that the backside irradiance module is based solely on the sky anisotropic model, which has negative values in the direct irradiance part. The reason is that the coordinate system used for modeling is a transparent body, whereas the Earth is a physical entity with a limited direct angle. Solar irradiance cannot penetrate the Earth to achieve a direct angle to the PV panels continuously. Therefore, it is necessary to consider whether the direct solar irradiance can be collected from the backside of bPV. By observation, besides the time of sunrise and sunset, the sun cannot directly shine on the backside.

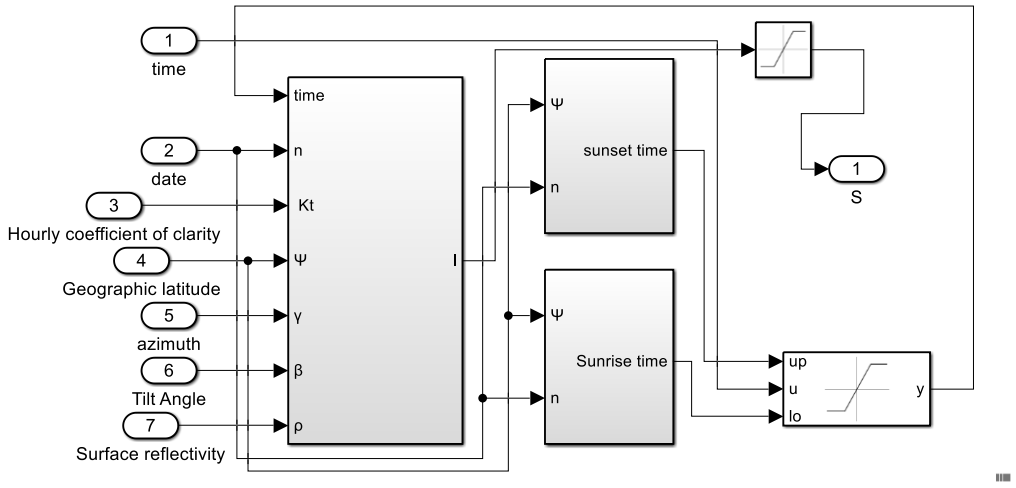

Fig. 5-1. Modeling of total irradiance of components during sunrise and sunset

The simulation is focused on the period between sunrise and sunset. Therefore, the azimuth of sunrise and sunset need to determine, which is shown in (5.12)~(5.14). Among them, Eq. (5.14) is the solar time angle and solar time converted in radians. By combing the value of sunrise and

sunset, the model of bPV generation is established, which is shown in Fig. 5-2. As a result, the direct irradiance on the backside is limited to the direct angle, and its value is zero at sunrise and sunset.

$$cos\omega_{s\,r} = tan\varphi\ tan\delta \tag{5.12}$$

$$\omega_{s\,r} = -\omega_{s\,s} \tag{5.13}$$

$$t = \frac{\omega \times 180}{\pi \times 15} + 12 \tag{5.14}$$

where ω_{sr} is the azimuth of sunrise (°), ω_{ss} is the azimuth of sunset (°), and t is the solar time (h).

Based on the model of the total irradiance of bPV in Fig. 5-1, and referring to the PV mathematical model in [179], the power generation model of bPV modules can be composed, which is shown in Fig. 5-2. As the components are connected in series, the equivalent current source is connected in parallel with a reverse diode. Unlike the diode in the equivalent circuit, this diode is a freewheeling diode that prevents short-circuiting of the current source under irregular shadows.

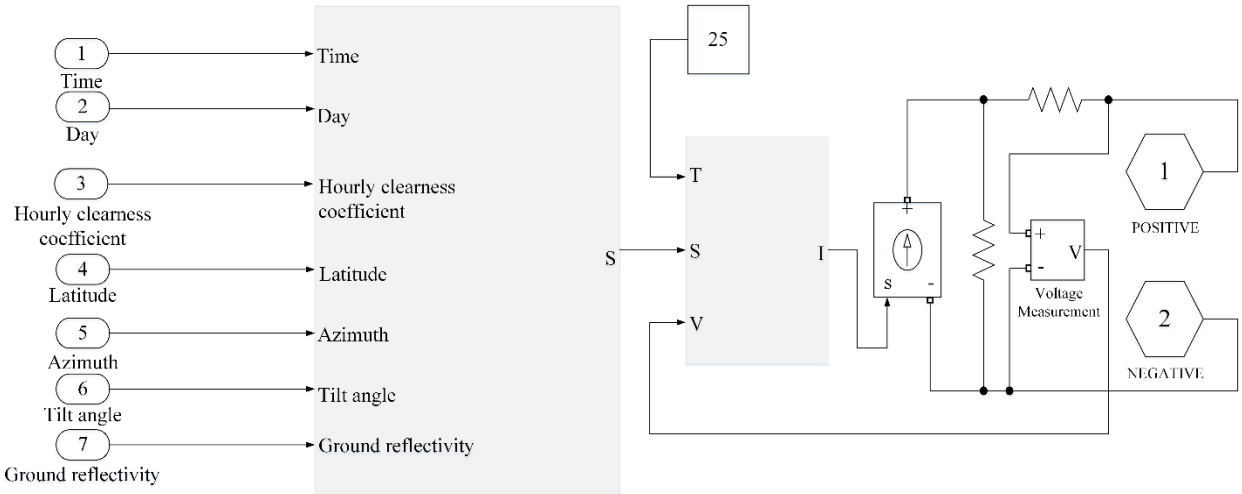

Fig. 5-2. Generation modeling of bPV components

5.3 Thermal Models of MPV and BPV

For PV arrays, bPV panels offer the best flame retardant properties due to a combination of good heat dissipation and high safety standards for several reasons: 1) low-temperature coefficient; 2) corrosion resistance. Unlike mPV modules, both sides of bPV modules use toughened glass with a melting point of 800 °C as the protective material. It is not prone to burn like TPT, which is the membrane of the backboard of a PV module. Furthermore, as it is encapsulated by glass and EVA,

the double-sided glass panel will not burn easily when encountering a fire. In addition, although the price of bPV is higher than mPV, its power generation efficiency is 12%~71% higher than mPV at latitudes of 40 º to 65 º [182]. Due to the difference in structure and materials of mPV and bPV, the thermal inertia is different, which determines how easy it is to burn. The thermal inertia of an object is the product of its heat transfer coefficient, density, and the specific heat capacity [183]. The greater the thermal inertia, the less likely the object can be ignited [184]. According to the parameters of module materials in Table 5-1, it can be calculated that the thermal inertia of the bPV is higher than that of the mPV modules, which proves the safety of the bPV is better than the mPV modules. In addition, when a cell of bPV is blocked, since the cell on the other side is still working normally, its power is not entirely converted to heat. Thus, EVA is not heated sufficiently to self-ignite. Hence, the probability of bPV module self-ignition is extremely low.

TABLE 5-1 THE PARAMETERS OF PV MATERIALS

	d (mm)	ρ (kg/m^3)	Cp (J/kg·k)	K (w/m·k)	ΔHc (kJ/g)
Glass	1.8	3000	500	1.8	0
EVA	0.2	940	2090	0.3	30.9
TPT	0.6	1395	1210	0.13	21.9
Solar cell	0.2	2320	700	150	0

The multi-layer structure of PV modules is illustrated in Fig. 5-3, while the thickness and thermophysical properties of the different layers are listed in Table 5-1. It is practically difficult to measure the temperature of PV cells directly. Therefore, a thermal model is hence proposed to capture the heat transfer process and calculate the temperature in each layer. The model is based on the following assumptions:

- Due to the small internal thickness of each layer, the internal longitudinal temperature gradient is neglected.
- The heat flux received by the back sheet and glass layer of the PV panel is equally distributed.
- Due to the close contacts, the gap between the EVA and silicon cell is neglected.

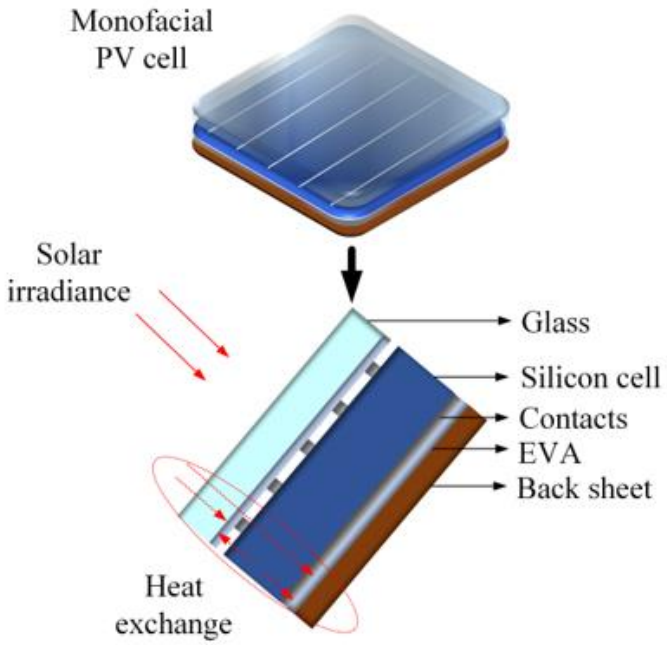

(a)

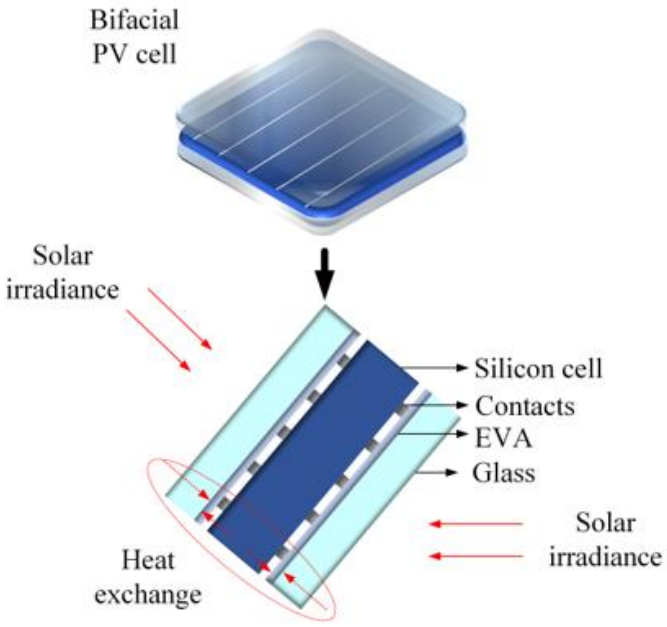

(b)

Fig. 5-3. Multi-layer structure of the (a) mPV and (b) bPV panels

5.3.1 Thermal model of mPV

The heat transfer model of an mPV panel is proposed as an equivalent thermal circuit, as shown in Fig. 5-4. Such an approach can facilitate the use of thermal resistance in different layers to calculate the energy transmission and heat loss [185].

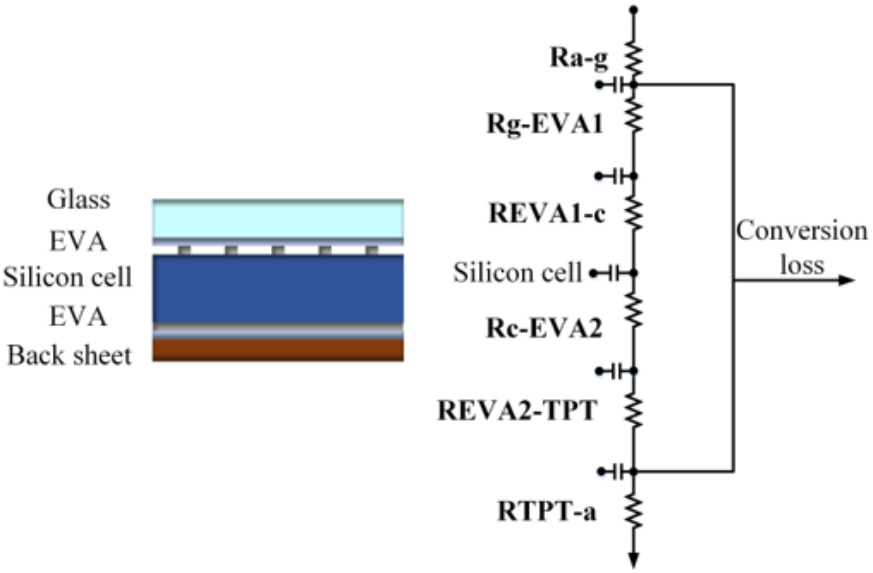

Fig. 5-4. The equivalent thermal circuit of mPV

(a) For the glass layer, the equation can be expressed as:

$$\alpha_g I_T = k(T_g - T_a) + u_{g-EVA1}(T_g - T_{EVA1}) \tag{5.14}$$

where α_g is the absorptance of glass, I_T is the irradiance intensity (W/m^2), k is the convective heat transfer coefficient (W/(m^2·ºC)), $u_{g\text{-}EVA1}$ is the convective heat transfer coefficient from glass to upper EVA film (W/(m^2·ºC)), T_g is the temperature of glass (ºC), T_a is the ambient temperature (ºC), and T_{EVA1} is the temperature of upper EVA film (ºC).

In Eq. (5.14), the temperature of the ambient and glass plate can be measured by a thermal detector, from which the temperature of the upper EVA film can be derived. However, considering the impact of thermal resistance of internal material, the upper EVA temperature obtained in Eq. (5.14) is the critical temperature of the glass layer next to the EVA layer. The actual upper EVA temperature can be derived according to the equation set of thermal resistance, which is expressed in Eq. (5.15).

$$R_{g-EVA1} = \frac{T'_{EVA1} - T_{EVA1}}{\alpha_{EVA1} I_T \tau_g A} = \frac{\delta_g}{2\lambda_g A} + \frac{\delta_{EVA}}{2\lambda_{EVA} A} \tag{5.15}$$

where $R_{g\text{-}EVA1}$ is the thermal resistance (Ω) between the glass and upper EVA, α_{EVA1} is the absorptance of upper EVA, τ_g is transmittance of glass, A is the area of the PV panel (m^2), λ_g is the glass thermal conductivity (W/(m·K)), λ_{EVA} is the EVA thermal conductive (W/(m·K)), δ_g is the thickness of the glass (m), δ_{EVA} is the thickness of the EVA film (m), and T'_{EVA} is the actual temperature of upper EVA (ºC).

(b) For the upper EVA layer, the equation of heat transfer can be expressed as:

$$\alpha_{EVA1}\tau_g I_T + u_{g-EVA1}(T_g - T_{EVA1}^{'}) = u_{EVA1-c}(T_{EVA1}^{'} - T_c) \quad (5.16)$$

where $u_{EVA1\text{-}c}$ is the heat transfer coefficient from upper EVA film to solar cell (W/(m^2·ºC)), and T_c is the critical temperature of a solar cell (ºC).

Considering the PV internal thermal resistance, the actual temperature of solar cell can be derived by critical temperature of solar cell, which is expressed as:

$$R_{EVA1-c} = \frac{T_c^{'} - T_c}{\alpha_c I_T \tau_g \tau_{EVA1} A} = \frac{\delta_{EVA}}{2\lambda_{EVA} A} + \frac{\delta_c}{2\lambda_c A} \quad (5.17)$$

where $R_{EVA1\text{-}c}$ is the thermal resistance between upper EVA and solar cell (Ω), τ_{EVA1} is transmittance of upper EVA, α_c is the absorptance of the solar cell, λ_c is the thermal conductive of solar cell (W/(m·K)), δ_c is the thickness of the solar cell (m), and the $T_c^{'}$ is the actual temperature of a solar cell (ºC).

(c) For the silicon cell layer:

$$\alpha_c \tau_{EVA1}\tau_g I_T + u_{EVA1-c}(T_{EVA1}^{'} - T_c^{'}) = \eta_c \alpha_c \tau_{EVA1}\tau_g I_T + u_{c-EVA2}(T_c^{'} - T_{EVA2}) \quad (5.18)$$

where η_c is the PV efficiency of a solar cell, $u_{c\text{-}EVA2}$ is the heat transfer coefficient from a solar cell to lower EVA (W/(m^2·ºC)), and T_{EVA2} is the critical temperature of lower EVA in the mPV module (ºC).

Similarly, the actual temperature of the lower EVA can be calculated as:

$$R_{c-EVA2} = \frac{T_{EVA2}^{'} - T_{EVA2}}{(\beta_c \alpha_{EVA2}\tau_c \tau_{EVA1}\tau_g I_T + (1-\beta_c)\alpha_{EVA2}\tau_{EVA1}\tau_g I_T)A} = \frac{\delta_c}{2\lambda_c A} + \frac{\delta_{EVA}}{2\lambda_{EVA} A} \quad (5.19)$$

where $R_{c\text{-}EVA2}$ is the thermal resistance between a solar cell and lower EVA (Ω), β_c is the packing factor of the solar cell, α_{EVA2} is the absorptance of the lower EVA, and $T_{EVA2}^{'}$ is the actual temperature of the lower EVA film (ºC).

(d) For the lower EVA layer:

$$\beta_c \alpha_{EVA2}\tau_c \tau_{EVA1}\tau_g I_T + (1-\beta_c)\alpha_{EVA2}\tau_{EVA1}\tau_g I_T + \beta_c u_{c-EVA2}(T_c^{'} - T_{EVA2}^{'}) = u_{EVA2-b}(T_{EVA2}^{'} - T_b) \quad (5.20)$$

where $u_{EVA2\text{-}b}$ is the heat transfer coefficient from lower EVA to the back sheet (W/(m^2·ºC)), and T_b is the critical temperature of the back sheet of the mPV module (ºC).

Accordingly, the critical temperature of the back sheet can be obtained by:

$$R_{EVA2-TPT} = \frac{T_b^{'} - T_b}{(\beta_c \alpha_b \tau_c \tau_{EVA2} \tau_{EVA1} \tau_g I_T + (1-\beta_c)\alpha_b \tau_{EVA1} \tau_{EVA2} \tau_g I_T)A} = \frac{\delta_{EVA}}{2\lambda_{EVA} A} + \frac{\delta_b}{2\lambda_b A} \quad (5.21)$$

where $R_{EVA2\text{-}TPT}$ is the thermal resistance between lower EVA and back sheet of a mPV panel (Ω), α_b is the absorptance, λ_b is the thermal conductive (W/(m·K)), δ_b is the thickness (m), and $T^{'}_b$ is the actual temperature (ºC) of the back sheet respectively.

(e) For the back-sheet layer, the equation can be expressed as Eq. (5.22).

$$\beta_c \alpha_b \tau_c \tau_{EVA2} \tau_{EVA1} \tau_g I_T + (1-\beta_c)\alpha_b \tau_{EVA1} \tau_{EVA2} \tau_g I_T + u_{EVA2-b}(T^{'}_{EVA2} - T^{'}_b) = u_{b-ba}(T^{'}_b - T_{ba}) \quad (5.22)$$

where $u_{b\text{-}ba}$ is the convective heat transfer coefficient from back sheet to backside ambient temperature (W/(m^2·ºC)), and T_{ba} is the backside ambient temperature of the mPV module (ºC), respectively.

Due to the turbulence flow of the air, the ambient temperature is different between the frontside and backside of the mPV panel. Comparing with the uniform surface temperature of the mPV panel on the front, the surrounding conditions on the back of the mPV panel are more complicated, such as the temperature of the back sheet, the shadow of the backside, and the air turbulence from the front side. Therefore, the backside temperature gradient is large, and it is difficult to measure a fixed value with a thermometer. However, it is possible to judge whether it will ignite the mPV panel based on the critical value of the temperature at a certain point.

For two adjacent layers of a PV module, the conductive heat transfer coefficient can be expressed as:

$$u_{i-j} = \frac{1}{(\delta_i / \lambda_i) + (\delta_j / \lambda_j)} \quad (5.23)$$

where λ_i and λ_j are the thermal conductivity (W/(m·K)), δ_i and δ_j are the thickness of the layer(m).

5.3.2 Thermal model of bPV

Similarly, an equivalent thermal circuit can be applied to the bPV module, as shown in Fig. 5-5, under the same assumptions. The only difference between the two types of modules is the use of

the glass layer instead of the TPT back sheet in the bPV. As a result, the bPV is bidirectional for the irradiance and heat absorption, it can be regarded as a convective heat transfer model, and the silicon cell layer is the boundary. As the heat energy from the front side of bPV is converted to the silicon cell layer, the thermal energy is converted into electrical energy. The forward heat energy is significantly smaller than the reverse heat conduction energy from the rear glass layer when the forward heat energy exceeds the cell layer. Therefore, the forward heat energy will be neglected on the lower layer. As mentioned above, for upper layers like front glass, upper EVA, the thermal models of mPV and bPV are the same.

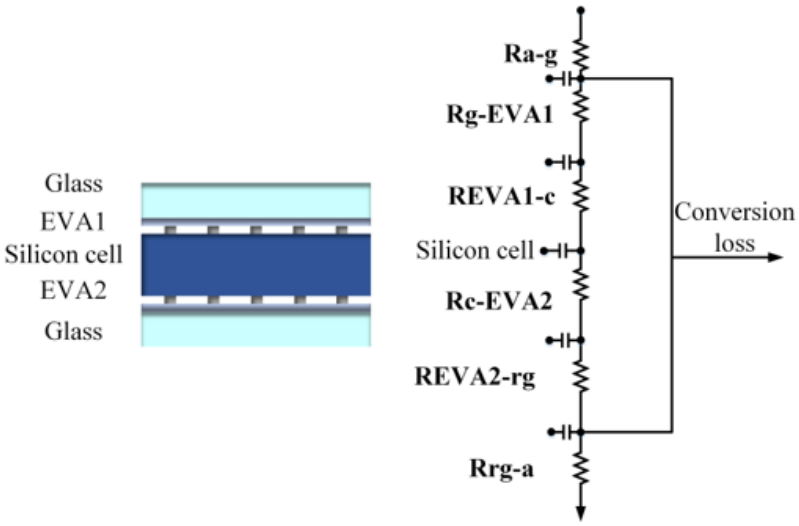

Fig. 5-5. The equivalent thermal circuit for the bPV module

(a) For the rear glass layer:

$$\alpha_{rg} I_T^{'} = k(T_{rg} - T_a) + u_{rg-EVA2}(T_{rg} - T_{EVA2}) \tag{5.24}$$

where α_{rg} is the absorptance of the rear glass, $I_T^{'}$ is the rear irradiance intensity (W/m^2), $u_{rg\text{-}EVA2}$ is the heat transfer coefficient from rear glass to lower EVA film (W/(m^2·ºC)), T_{rg} is the temperature of rear glass (ºC). It should be noticed that the rear irradiance intensity absorption is n% of the front irradiance intensity, where n% is the light absorption proportion, which is dependent on the tilt angle of bPV panel.

Then, the actual temperature of lower EVA film can be derived by using the equation set of thermal resistance, like the model of mPV.

(b) For the lower EVA layer of the bPV:

$$\alpha_{EVA2}\tau_{rg} I_T^{'} + u_{rg-EVA2}(T_{rg} - T_{EVA2}^{'}) = u_{EVA2-c}(T_{EVA2}^{'} - T_c) \tag{5.25}$$

where τ_{rg} is the transmittance of rear glass of bPV, $u_{EVA2\text{-}c}$ is the heat transfer coefficient from the lower EVA film to the solar cell (W/(m^2·°C)).

(c) For the silicon cell layer, the energy can be regarded as the sum of forwarding energy transfer and reverse energy transfer:

$$\begin{aligned}&\alpha_c(\tau_{EVA1}\tau_g I_T+\tau_{EVA2}\tau_{rg}I_T^{'})+u_{EVA1-c}(T_{EVA1}^{'}-T_c^{'})+u_{EVA2-c}(T_{EVA2}^{'}-T_c^{'})=\\&\eta_c\alpha_c(\tau_{EVA1}\tau_g I_T+\tau_{EVA2}\tau_{rg}I_T^{'})+u_{c-EVA2}(T_c^{'}-T_{EVA2})+u_{c-EVA1}(T_c^{'}-T_{EVA1})\end{aligned} \tag{5.26}$$

In summary, the relationship between the temperature of the EVA (and PV cell) and the outside temperature in bPV and mPV can be obtained, respectively, using these equivalent circuit models. In this way, the external temperature that can render the PV panel to be ignited can be deduced backward.

5.4 Thermal Model of MPV and BPV Configuration of the PV Array

As discussed earlier, the bPV module is known to be more resilient against fire but more costly. It is, therefore, proposed to use a hybrid PV array in which the bPV modules are inserted between the mPV modules as shown in Fig. 5-6 in order to achieve a balance between safety and cost-effectiveness.

In this section, the optimal configuration of a hybrid PV array is discussed in two aspects: fire propagation and cost-effectiveness, which are the key factors that determine the installation spacing between the PV panels. Consideration will also be given to keep the land use as low as possible while achieving the desired power output.

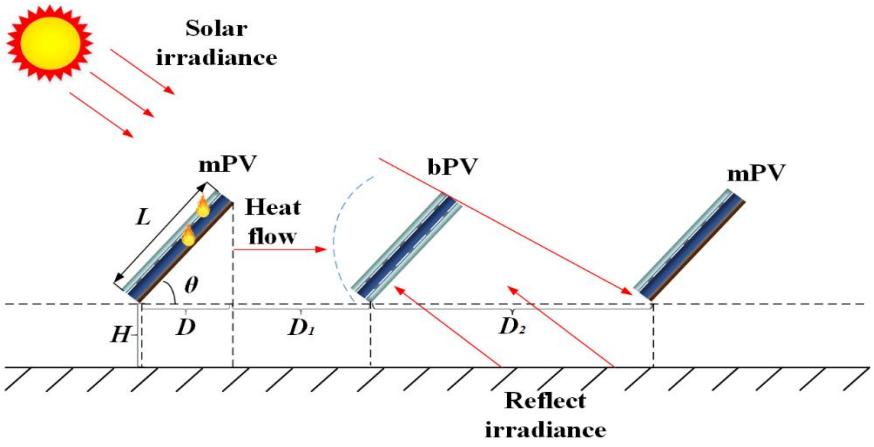

Fig. 5-6. The installation strategy of the hybrid PV array

5.4.1 Fire propagation

The distance *S* between mPV and bPV installation in the hybrid PV array equals $D+D_1$, in which *D* is affected by the tilt angle (θ) of the PV panel. As for the factor of fire propagation between mPV and bPV, it is essential to define the security space of the PV array D_1, which is affected by the wind velocity, radiation source, and airflow.

Since the temperature of the combustion source changes with the airflow, the momentum is considered in the array. As for the contact between air and surface of a PV panel, it is a turbulence flow situation. Nusselt number (*Nu*) can be obtained by combining Newton's law of cooling and Fourier's law of heat conduction with the general definition of *Nu* [186]. Meanwhile, combined with the *Nu* calculation by the Dittus-Boelter equation, the distance between the inlet (fire source) and the surface of the panel D_1 can be calculated by Eq. (5.27).

$$Nu = -\frac{\partial T}{\partial n}\frac{D_1}{T_{ig} - T_0} = 0.023\,\mathrm{Re}^{0.8}\,\mathrm{Pr}^{0.4} \tag{5.27}$$

where ∂T/∂n is the PV panel surface normal temperature gradient, *Re* is the Reynolds number and *Pr* is Prandtl number, T_0 is the initial temperature of the PV array (ºC), T_{ig} is the combustion temperature of PV panel (ºC), which is equal to T_g or T_{rg}.

$$\mathrm{Re} = \rho v d \,/\, \mu \tag{5.28}$$

$$\mathrm{Pr} = c_p \mu \,/\, \lambda \tag{5.29}$$

where ρ is the air density (kg/m^3), *v* is the wind velocity (m/s), μ is dynamic viscosity (Pa·s), c_p is the specific heat capacity of airflow (J/(kg·ºC)), and *d* is the length of heat conduction (m).

The distance *S* between mPV and bPV is derived as:

$$S = L\cos\theta + D_1 \tag{5.30}$$

where *L* is the length of PV panels (m), and θ is the tilt angle of PV panels (º).

5.4.2 Cost-effectiveness

In order for bPV to fully absorb the reflected irradiance from the ground and occupy a small area of land as much as possible, the distance D_2 between bPV and mPV needs to be defined. Due to the study based on P-type bPV panel and mPV panel, according to the data provided by PV panel manufacturers, the price of bPV is 2.5 times more than that of mPV, and the power generation

efficiency of the front side of bPV e_{mPV} is the same as that of mPV, which is 21%. Meanwhile, the double-side gain of a bPV module $g_{double\text{-}side}$ is approximately 70%, which means that the efficiency of bPV is 3.33 times that of mPV. The albedo of bPV e_{albedo} can be calculated by (5.31) [187], which is 15%.

$$g_{double-side} = \left(\frac{e_{albedo} - e_{mPV}}{e_{mPV}} \right) \times 100\% \tag{5.31}$$

In addition, based on the mathematical model of bPV, the view factor from rear side can be calculated by (5.32) [188]. However, the rear side view factor can be obtained by bifacial gain, and the distance D_2 between bPV and mPV panel is obtained by (5.32).

$$\begin{aligned} e_{albedo} &= \frac{\sqrt{H^2 + D_2^{\,2}} + A - H - L^2 - H^2 - 2HL\cos(\theta + 90^\circ) - D_2^{\,2} + 2BD_2 \cos(\arctan(\frac{H + L\sin\theta}{L\cos\theta}))}{2D_2} \\ B &= \sqrt{L^2 + H^2 + 2HL\cos(\theta + 90^\circ)} \end{aligned} \tag{5.32}$$

where H is the height of the PV array (m).

Theoretically, the cost performance of bPV is much higher than that of mPV, and all bPV modules should be used in the array. However, if a bPV array is required to fully absorb the reflected radiation from the ground, the row spacing of the bPV array will be higher than that of the hybrid array and the mPV array, which can be regarded as D_2. Counting the area occupied by the land, the benefits of bPV are far less cost-effective than hybrid arrays. To sum up, the space of installation of the hybrid PV array follows Eqs. (5.30) and (5.32).

5.5 Experiment Results

In order to verify the feasibility and accuracy of the hybrid array strategy, the experiment is conducted in two parts, which contains thermogravimetric and fire propagation experiments. The facilities and its parameters are shown in Fig. 5-7 and Table 5-2, respectively, including bPV, mPV, Fresnel lens, thermocouple, multimeter, and thermal imaging camera. The above facilities are installed as shown in Fig. 5-7. Install the PV array according to Fig. 5-4, and its inclination is based on the latitude of Xuzhou, China (34°16'N). Simultaneously, the above facilities are used for simulation and testing.

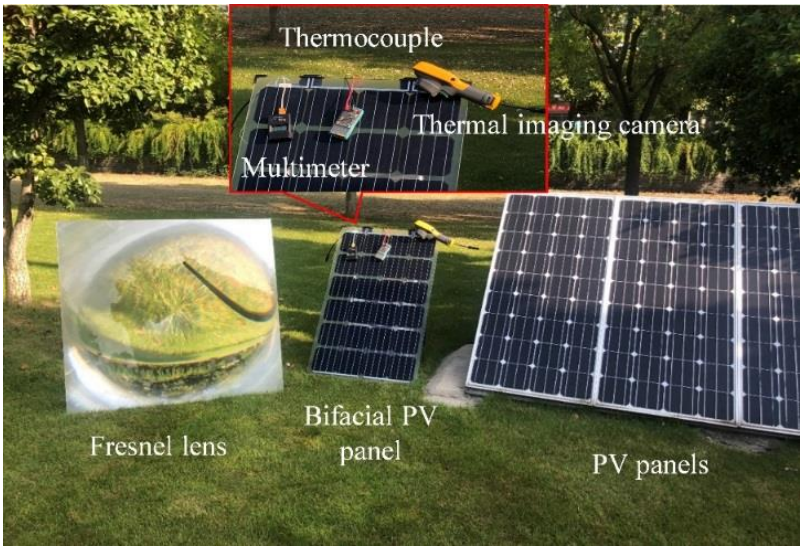

Fig. 5-7. The facilities of experiment

TABLE 5-2 THE PARAMETERS OF EXPERIMENT FACILITIES

	Fresnel lens	bPV	mPV
Size (mm)	1000*1000*10	1100*630*6	1500*650*10
Open circuit voltage (V)		11.48	7.44
Short circuit current (A)		1.63	3.07

Before the combustion experiment of PV panels, the thermal test of the two kinds of PV panels is needed to carry out, which is used to analyze the difference of thermal sense between the bPV and mPV. The environmental temperature of the test is from 20 °C to 25 °C, and the time is between 10:00 a.m. to 15:00 p.m.. The result is shown in Fig. 5-8, and the unit of the data values in the figure is °F. During the change process of solar radiation intensity, the changing trends and amplitudes of the temperatures on the surfaces of bPV and mPV are basically the same. However, considering that bPV absorbs heat on both sides, and the reflection of light can increase the intensity of radiation, and the temperature of the microenvironment will increase when it works. Therefore, the temperature trend of the two kinds of PV panels seems to be the same. It is worth noting that although the overall performance of the PV cell decreases as the radiation intensity increases (increased ambient temperature), the benefits brought by the backside of bPV panel outweigh the performance degradation. Therefore, the impact of temperature on mPV is much greater than that of bPV.

In addition, a mPV is more sensitive to temperature, which indicates that a mPV is more prone to failure, especially when the DC arc effect of its wires occurs because of the high temperature. Due to the different structures of the two kinds of PV panels, the bPV fire rating has been upgraded from C-level to A-level for ordinary crystalline silicon modules. Therefore, in the next combustion experiment, the combustion failure of mPV will be used as the starting point to verify the flame retardancy of bPV. Firstly, an array of 3 panels (the structure is mPV-bPV-mPV) needs to be built in the combustion experiment, and the first mPV is set as the fire source. Secondly, different distances from the fire source are arranged to measure the changes in the surface temperature and appearance of the PV panels. The burning situation is recorded during the burning process. Finally, the impact of self-ignition on PV panels and whether PV panels will intensify the combustion process are evaluated.

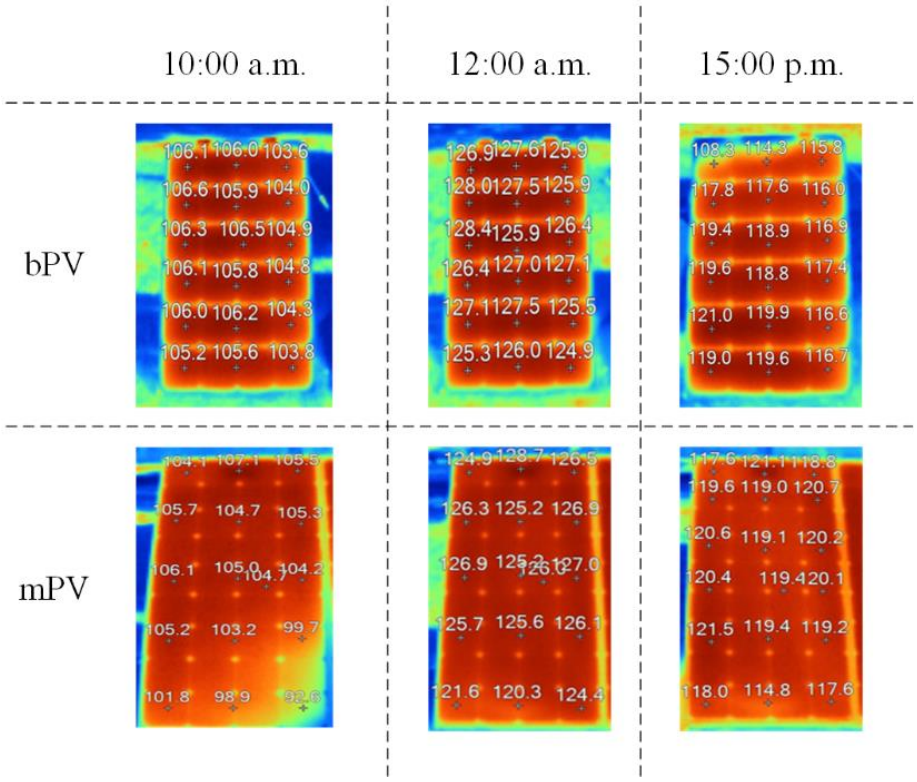

Fig. 5-8. The comparison of thermal test between bPV and mPV from 10:00 a.m. to 15:00 p.m.

The combustion experiment is to verify the fire resistance of the PV array, and the steps are based on the flow chart in Fig. 5-9. Firstly, the sunlight focused by the Fresnel lens is used to simulate the hot spot effect, which makes the illuminated PV panel ignite spontaneously. The combustion exotherm of mPV panel is measured, and its temperature T_0 is set as the incident heat flow of the PV array. Secondly, use T_0 to compare the ignition temperature of the bPV T_{ig}, and if T_{ig} is greater

than T_0 in the heat flow transfer, it means that the heat release of mPV will not burn bPV, that is, the PV array is safe. On the contrary, the PV array will burn by incident heat flow. Then, the ambient temperature around the bPV T_a is obtained from it. Finally, once the T_a is determined, it will proceed to the last step to obtain a safe row spacing by comparing the distance between the two PV panels.

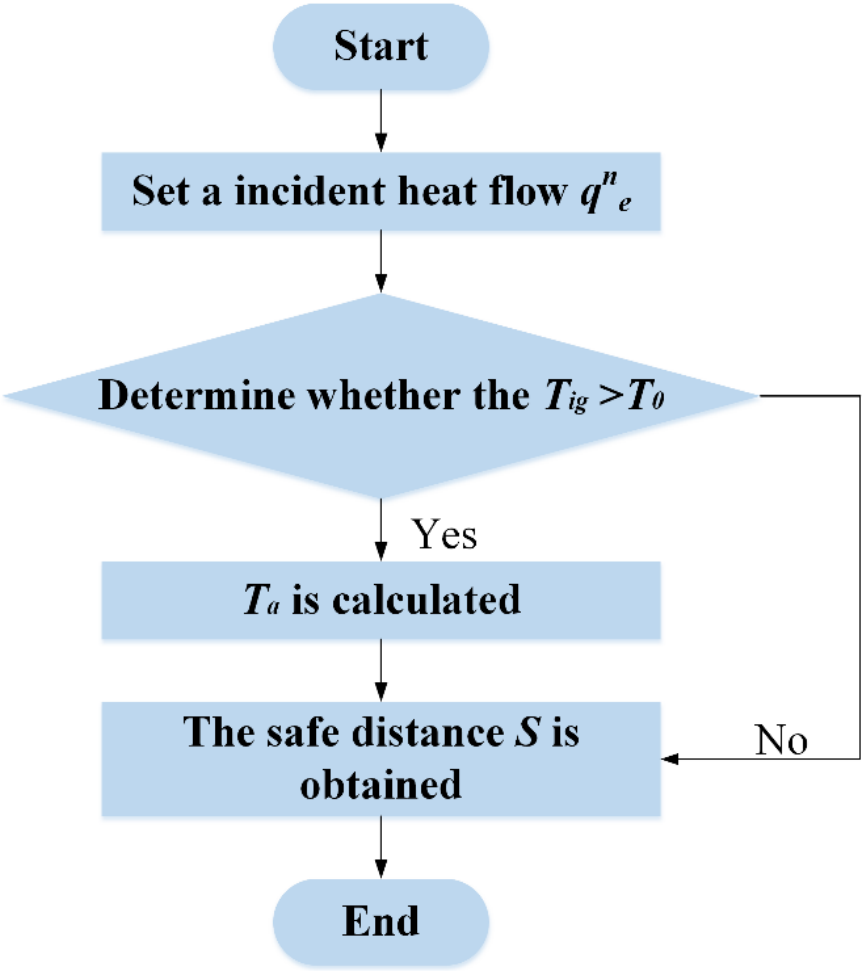

Fig. 5-9. The procedure of combustion experiment

Through the combustion experiment of bPV solar panels, there are three stages of combustion in the observation. Firstly, the temperature in the range of 200~380 °C, a small part of the bPV panel is heated and cracked, and a small number of bubbles seep out from the cracks. Then, keep heating panel to 400-461 °C, the middle interlayer part remains unchanged for 480 s, and only the double-layer glass sealant at the edge melts and scorches. Finally, as the temperature continues to rise to 547 °C, the glass begins to fall off. The intermediate colloids burns first, and the bPV panels begins to soften and fall. Its combustion flame temperature is 560-580 °C, and the combustion time is 170 s. The procedure is shown in Fig. 5-10.

The overall ignition temperature of the bPV panel is about 547 °C. Compared with the mPV panel, the ignition point of bPV is higher than that of mPV (about 400 °C). In addition, in the case of a breeze in the environment, namely heat flow transfer, it has little impact on the adjacent panels and will not ignite the surrounding panels.

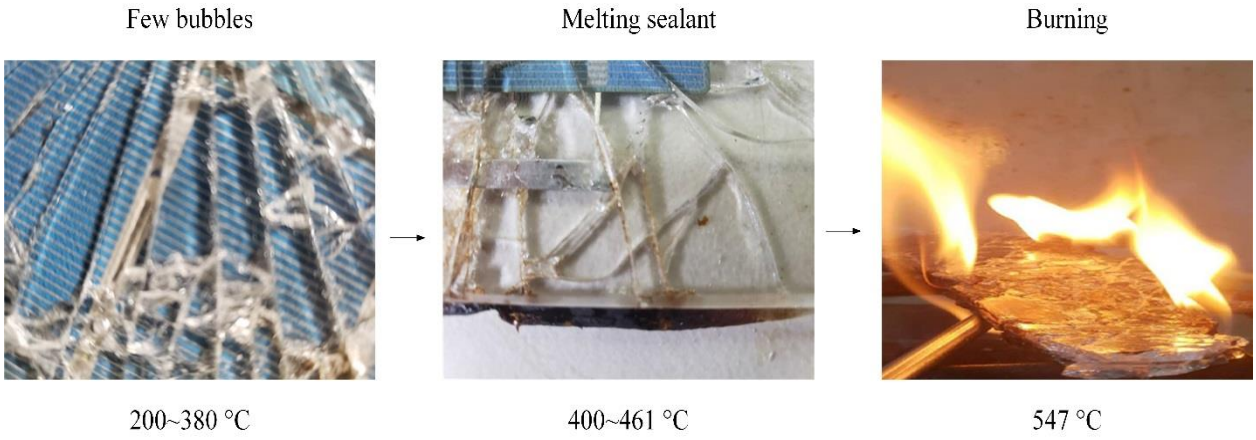

Fig. 5-10. The change of bPV heating

Since the burning of PV panels will release a large amount of flammable and toxic gases, thermogravimetric experiments can be used to analyze the stability of PV module materials, namely the mass of the released gas. According to the results of the thermogravimetry experiment from Fig. 5-11, the time of mass change occurs when the thermogravimetry progresses to 1500s, namely 25 minutes in both types of PV panels. The temperature in the sharp change zone is the 2040s to 2400s (34 minutes to 40 minutes). Compared with Fig. 5-11(b), the TG curve in Fig. 5-11(a) has a “slope”, which indicates the bPV has certain flame retardancy.

There are two points that can be explained. Firstly, compared with the mPV, the melting point and ignition point of the bPV material have been greatly improved. Secondly, compared with the firing efficiency of the open flame, the difference is about 100 ºC between two kinds of PV panel, it indicates that the structure of the bPV greatly increases the ignition temperature, and the airtight structure delays the ignition time.

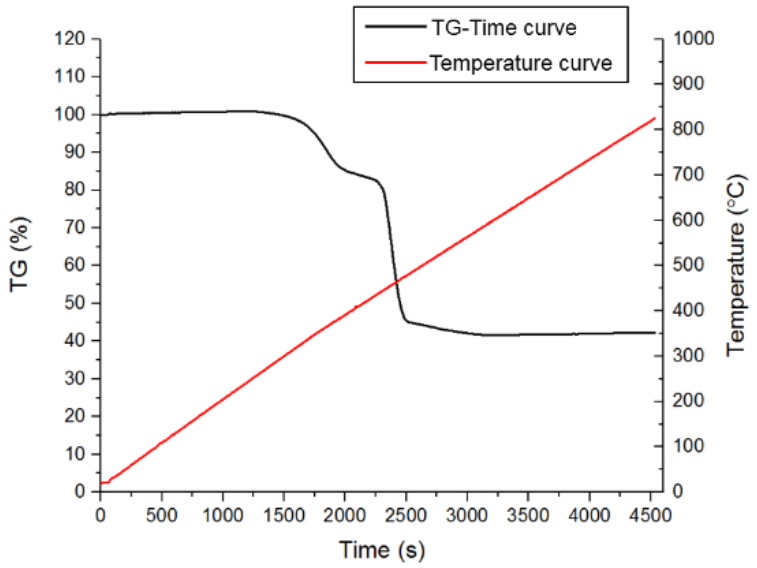

(a)

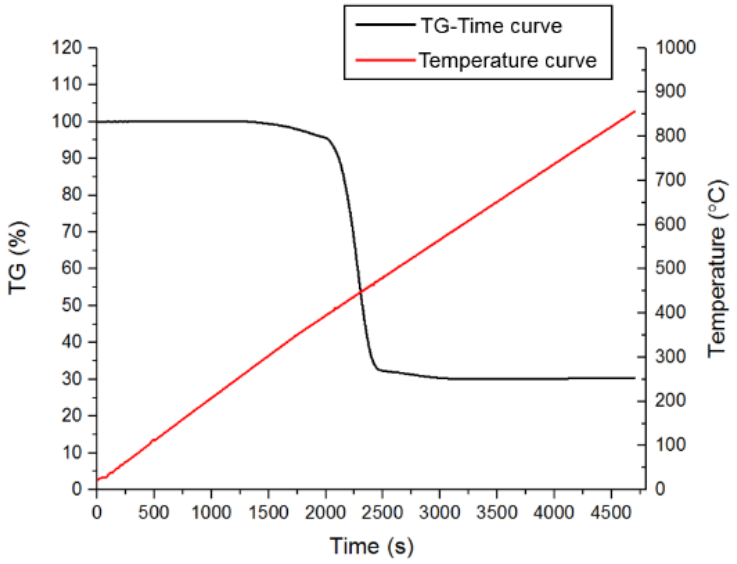

(b)

Fig. 5-11. The results of thermogravimetric experiments. (a) bPV (b) mPV

The fires of the PV array are mostly related to cables. In order to simulate the influence of the real partial heating, the experiment was carried out on the basis of the thermogravimetric experiment and the combustion experiment. In order to reflect the partial heating effects of hot spots and electrical faults in the array, an artificial partial hot spot experiment is carried out using Fresnel lenses.

Initially, perform hot spot ignition on the first PV panel of the hybrid array, namely the released heat of the burning PV panel, with the incident temperature of the PV array being 260 ºC. During this time period, there is no significant change in the bPV panel. However, for a hot spot effective mPV panel, the front side of the panel will burn with an open flame for heating 5s, and the whole PV panel will burn after 20s. Meanwhile, the release temperature reaches 560 ºC to the adjacent bPV panel. For the front side, bubbles appeared on the surface for about 30s, and the glass burst in about 1 minute, and more obvious smoke appeared on the back after 150s, and the smoke dimension is 4 cm^2. However, when the position and intensity of the hot spot remained unchanged, the burst range and smoke range did not expand significantly until 5 minutes, and no open flame appeared. For the heating part of the backside, the glass on the back burst when the heating process lasts for about 10s~15s and the high concentration smoke appears on the front. The smoke reaches the highest concentration in about 1 minute. After continuing to heat the backside in 5 minutes, there is no open flame on the solar panels. When the surface temperature is 1150 ºC, it is continuously heated for 8 minutes, the open flame on the front side, and the fire dimension is 25 cm^2, but no change on the backside. However, the open flame will slake after 30s. All procedures of the heating experiment for each PV panel are shown in Fig. 5-12.

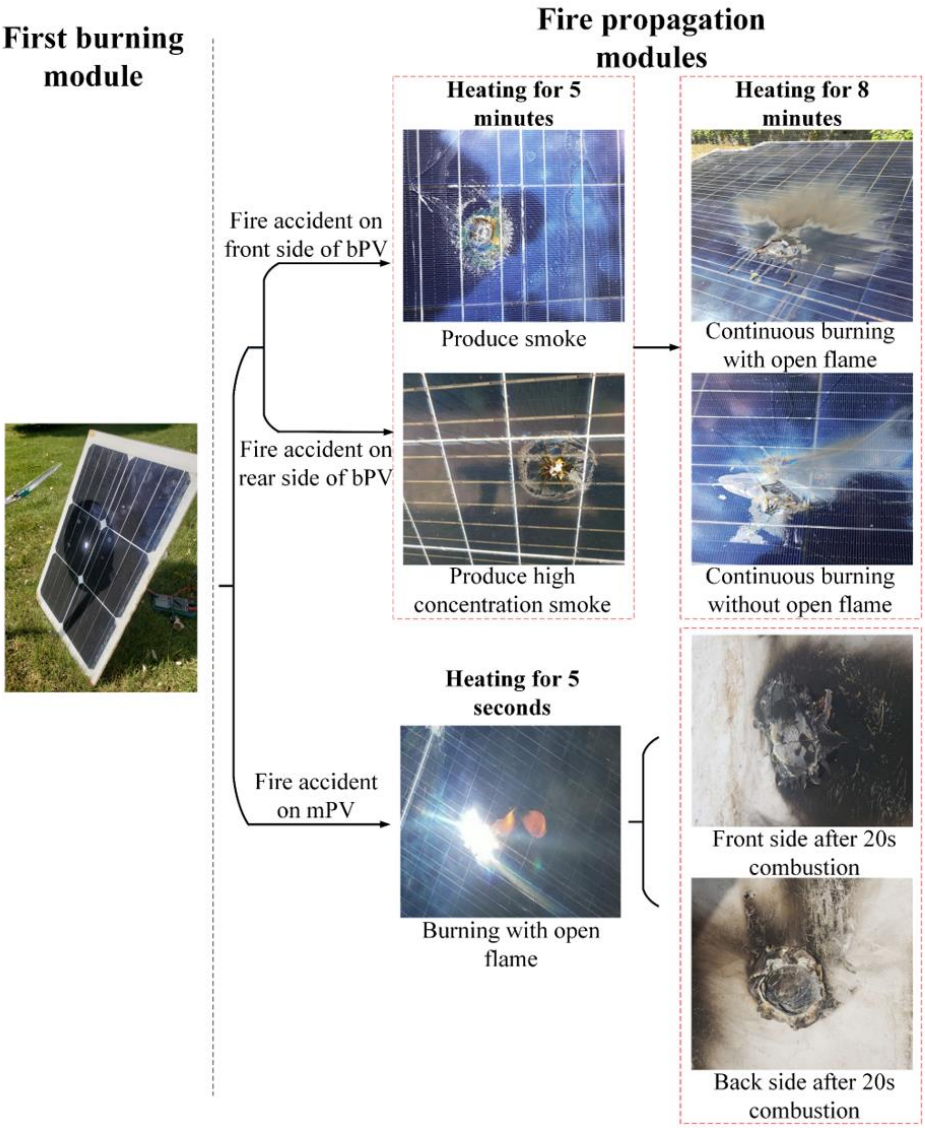

Fig. 5-12. The procedure of heating experiment

In summary, according to the proposed PV array, flame retardant and profitability were verified by experiments. The experimental results show the critical distance, which is calculated from the above-mentioned row spacing of the PV panel formula, ensures high profitability and safety.

5.6 Summary

This study proposes a new management strategy for large-scale PV arrays, namely, hybrid array of mPV and bPV modules for improving the safety and profitability of PV arrays. The proposal is obtained on the basis of single-phase thermal coupling theory, so it is easy to implement. The main contributions of our study are as follows:

1) According to the thermal models of the two kinds of PV panels, the ignite temperature of the flammable part of the plastic film in the panel is calculated, taking into account

the thermal resistance of the panel. Thus, the ambient temperature at which the PV panel burns can be deduced. Simultaneously, by analyzing the turbulent motion of the airflow in the PV array, a single-phase thermal coupling model is established.

2) According to the reflectivity of the bPV, the row spacing of the bPV array is derived, namely, the distance from bPV to mPV in the hybrid array. Combined with the safety distance *S* from mPV to bPV, a model of the hybrid array can be obtained, which will detail the PV array installation rules clearly.

3) Through the double-sided gain and reflection factor of bPVs, the optimal distance between bPV and mPV in the PV array is obtained, which increases the output of the array.

Finally, this strategy effectively prevents the spread of fire in the PV array and keeps the PV array in an efficient and safe working state. Moreover, this research is conducive to the promotion of related technologies in the industrial field.

Chapter 6 Conclusions and Future Work

6.1 Summary

This thesis describes in detail several management strategies for improving PV array efficiency and safety. As an environmentally friendly power generation method, PV power is renewable, making it a promising alternative to traditional thermal power generation. Hundreds of scholars and engineers around the world are studying PV management-related technologies to improve the efficiency and safety of PV power. Unfortunately, much work remains to be done before PV power generation technology is fully mature, especially for the safety issues that are concerned the most by the public. The continuous fire cases of PV arrays have hindered the promotion of PV power generation. Therefore, it is crucial to develop technologies dedicated to improving its efficiency and safety. The risks of PV power generation, which is different from traditional thermal power generation, mainly come from the impact of external factors. Therefore, this thesis proposed management strategies of large-scale PV arrays.

Firstly, the thesis introduced two issues under the impact of sand and dust blockage on the PV power panels, which show the relationships between dust reduction and power generation efficiency, and page temperature, respectively. In response to these two problems, this paper proposes solutions that can help improve the safety and output of PV arrays. Secondly, when the PV panel is severely affected by sand and dust, the PV panel will suffer from aging and other issues, causing the power output to be significantly reduced. Considering that traditional methods are usually costly and leave little margin for profits, a genetic algorithm is also proposed for PV array reorganization to increase both the output and profits. Thirdly, as the aging issue is believed to be the main cause of the reduced efficiency of PV power generation and the fire hazards of PV arrays, it is classified as a problem that needs to be solved, and a comprehensive review is to be conducted. According to the UL manual, the safety considerations of PV power generation should be explained in detail, which will provide guidance for relevant research and raise public awareness of the safety issues of PV power generation. Then, a DC-DC converter must be employed to increase the efficiency of PV power generation. Although converters are traditionally used in existing PV arrays, it is worth noting that the combiner box will generate DC arc due to the aging of the cables, which will be a potential risk of fire. Simultaneously, due to the integration of more power electronic equipment, system reliability will be reduced. Therefore, this thesis designed a PV array arrangement method that combines mPVs and bPVs in an array to prevent large-scale PV fires by setting a safe installation distance.

In Chapter 2, an in-depth literature review was performed, introducing the causes of PV fire risks and mainstream solutions. With the increasing number of applications of solar PV technology, safe operation and maintenance of the installed solar panels become more critical as hot spot effects and DC arcs might cause fire accidents. The risk mitigation solutions mainly focus on two aspects: structure reconfiguration and the development of a faulty diagnosis algorithm. The first is to reduce the hot spot effect by adjusting the space between two PV modules in a PV array or relocating some PV modules. The second is to detect the DC arc faults before it causes a fire. There are three types of arc detection techniques, including physical analysis, neural network analysis, and wavelet detection analysis. Through these detection methods, the faulty PV cells can be found promptly, thereby reducing the risk of PV fire. Based on the review, some precautions are implemented in the industry to prevent solar panel-related fire accidents in large-scale solar PV plants that are located adjacent to residential and commercial areas.

Chapter 3 introduced the research of PV dust reduction based on numerical simulation. For a PV power generation system, the shading effect of PV panels caused by dust deposition is extremely undesired. The deposition of dust results in a severe reduction of power generation output since the received irradiance and cooling of PV panels are affected by the shading and blocking. In this study, a numerical simulation method was proposed to model the dust accumulation on PV panels to simulate how PV power generation is affected by different wind directions and wind speeds. The proposed model is of highly accurate numerical simulation and short calculation cycle, providing reliable prediction for the soiling management of PV panels in the wind-sand environment to a certain degree. Through simulations and experiments, the impacts of dust accumulation on the performance of PV panels with different wind directions are studied detailedly. The study is based on the environment of Liverpool, England, in a year, with the wind speed changing from 4.43 m/s to 6.48 m/s and the dust particle size of 10 μm to 100 μm. Moreover, for PV arrays, the turbulences of the dust distribution around the PV panels were also analyzed. The data collected from experiments and simulations are used to verify the effectiveness of the proposed strategy.

Chapter 4 introduced the PV array recombination strategy based on a genetic algorithm. In the past decades, numerous large-scale PV plants have been constructed globally. However, the capital and operational costs remains high, which limits their potential to be applied further. Because the installed PV modules often operate in harsh environments (i.e., storm, high temperature, dust, hail, etc.), non-uniform aging phenomena of PV modules are inevitable. The phenomena impact adversely on the performance of PV plants, especially in the middle and late periods of their service

life. This paper developed an offline PV module reconfiguration strategy for the non-uniform aging PV array to mitigate this effect. In order to maximize the economic benefit, electricity price and labor costs are considered in the offline reconfiguration. The Branch-and-Bound based optimization algorithm is proposed to find the highest economic benefit. In order to verify the proposed algorithm, MATLAB software-based modeling and simulation were performed in four case studies. A typical 42kW PV array with a 7×20 connection is employed in a testing benchmark, and the human resources cost and electricity price in the USA, UK, China, and Turkey are also considered. The results demonstrated that the economic benefit from a non-uniformly aged PV array is improved by using the proposed reconfiguration method.

Chapter 5 introduced a novel array installation strategy to improve array security. Many existing PV plants have prioritized the spacing distance of solar panels solely for the maximum power generation without careful consideration of the safety against fire accidents of the PV arrays. In order to reduce the risk of fire in the large-scale application of solar panels whilst increasing the PV power outputs, this study proposed to use bPV panels instead of flame-retardant materials to isolate flammable PV arrays with reasonable installation spacing. This study contributed to the fire risk reduction in twofold: Firstly, we identify the relationship between the combustion temperature and the ambient temperature of different PV panel materials, namely the bPV and mPV. Secondly, the installation distances between PV panels are optimized based on the ambient temperature and turbulence field that cause combustion. The proposed optimal placement of bPV and mPV combinations in large-scale solar PV power plants effectively prevents solar panel fire accidents. Due to the application of the bPV, this design can generate the same amount of power for the same size of areas.

6.2 Future Work

Based on the conclusions above and considering the limitations of the work that existed, future research can be directed in the following areas.

- **Further investigation on PV cleaning cycle in different areas**

Chapter 3 demonstrated that the accuracy of PV dust fall prediction based on numerical simulation is significantly high, and the relationship between dust, output, and heat dissipation was discovered. Generally, each region produces different results due to different latitudes, wind speeds, and wind directions. Although the UK PV dust reduction forecast has been solved by existing technology, efficient and cost-effective cleaning solutions have not yet been implemented. Therefore,

comprehensive studies and research can be conducted to address this issue, which will further improve the efficiency of PV power generation.

- **Further investigation for PV reconfiguration with different algorithms**

This thesis proposed a PV reconfiguration strategy based on GA, which includes an algorithm with numerous advantages, such as cost-effectiveness, easy operation, etc. In Chapter 4, the potential benefits for several countries were compared, assuming implementing the proposed strategy. However, with the development of data-driven technologies, GA may be replaced by other algorithms shortly. Neural networks, as an emerging data-driven technology, are currently widely employed to detect PV faults such as arcs, whose calculation methods are different from GA and yet to be mass implemented on PV reconfiguration strategies. Therefore, developing PV array arrangement strategies based on neural networks is the future research direction. Instead of focusing on multi-functions, more advanced strategies need to be studied in the future.

- **Further investigation for bPV in different cost-effective areas**

Although the hybrid array method proposed in Chapter 5 can achieve higher security and improve array power generation to a certain extent, its power generation efficiency is far inferior to that of pure bPV arrays. However, bPV panels cannot be massively applied due to their high cost. Thus, the next step is to improve the structure and packaging of bPV panels to reduce costs. Meanwhile, when a fire accident happens to bPV, it will not produce a large amount of toxic gas. To solve these issues, the structure of bPV should be studied in depth to improve its reliability and further improve the safety of PV applications.

Reference

[1] A. Louwen, Wilfried G.J.H.M. van Sark, Andre´ P.C. Faaij, Ruud E.I. Schropp, "Re-assessment of net energy production and greenhouse gas emissions avoidance after 40 years of photovoltaics development," *Nature communications*, 7:13728, DOI: 10.1038/ncomms13728, 6 Dec 2016.

[2] Fang-rong Ren, Ze Tian, Jingjing Liu, Yu-ting Shen, "Analysis of CO2 emission reduction contribution and efficiency of China's solar photovoltaic industry: Based on Input-output perspective," *Energy*, Volume 199, 2020, 117493, ISSN 0360-5442, https://doi.org/10.1016/j.energy.2020.117493.

[3] IRENA, "Future of solar photovoltaic," ISBN 978-92-9260-156-0, 2019.

[4] I.L.R. Gomes, R. Melicio, V.M.F. Mendes, "Dust effect impact on PV in an aggregation with wind and thermal powers," *Sustainable Energy*, Grids and Networks, Volume 22, 2020, 100359, ISSN 2352-4677, https://doi.org/10.1016/j.segan.2020.100359.

[5] S. S. Nair, "A Survey report of the firefighters on fire hazards of PV fire," *2018 IEEE International Conference on System, Computation, Automation and Networking (ICSCA), Pondicherry*, 2018, pp. 1-5, doi: 10.1109/ICSCAN.2018.8541219.

[6] P. D. Moskowitz, V. M. Fthenakis, "Toxic materials released from photovoltaic modules during fires: Health risks," *Solar Cells*, Volume 29, Issue 1, 1990, Pages 63-71, ISSN 0379-6787.

[7] B. Liao, L. Yang, X. Ju, Y. Peng, Y. Gao, "Experimental study on burning and toxicity hazards of a PET laminated photovoltaic panel," *Solar Energy Materials and Solar Cells*, Volume 206, 2020, 110295, ISSN 0927-0248.

[8] J. Sipe, "Development of Fire Mitigation Solutions for Photovoltaic (PV) Systems Installed on Building Roofs," July 2016.

[9] http://www.mofcom.gov.cn/article/i/jyjl/m/201302/20130200032328.shtml, 20/02/2013.

[10] G. Manzini, P. Gramazio, S. Guastella, C. Liciotti, G. L. Baffoni, "The Fire Risk in Photovoltaic Installations - Test Protocols For Fire Behavior of PV Modules," *Energy Procedia*, Volume 82, 2015, Pages 752-758, ISSN 1876-6102.

[11] W. John, K. Sarah, “How Can We Make PV Modules Safer,” *Conference Record of the IEEE Photovoltaic Specialists Conference*, June 2012.

[12] Chr. Lamnatou, G. Notton, D. Chemisana, C. Cristofari, “Storage systems for building-integrated photovoltaic (BIPV) and building-integrated photovoltaic/thermal (BIPVT) installations: Environmental profile and other aspects,” *Science of The Total Environment*, Volume 699, 2020, 134269, ISSN 0048-9697.

[13] M. Perry, A. Troccoli, “Impact of a fire burn on solar irradiance and PV power,” *Solar Energy*, Volume 114, 2015, Pages 167-173, ISSN 0038-092X.

[14] G. N. Tiwari, R. K. Mishra, S. C. Solanki, “Photovoltaic modules and their applications: A review on thermal modeling,” *Applied Energy*, Volume 88, Issue 7, 2011, Pages 2287-2304, ISSN 0306-2619.

[15] D. Prince Winston, S. Kumaravel, B. Praveen Kumar, S. Devakirubakaran, “Performance improvement of solar PV array topologies during various partial shading conditions,” *Solar Energy*, Volume 196, 2020, Pages 228-242, ISSN 0038-092X.

[16] C. Coonick, “Fire and Solar PV Systems – Investigations and Evidence,” *breNational Solar Centre*, 11th May 2018. P100874-1004, Issue 2.9.

[17] https://www.china5e.com/m/news/news-229160-0.html.

[18] P. Rajput, G.N. Tiwari, O.S. Sastry, “Thermal modeling and experimental validation of hot spot in crystalline silicon photovoltaic modules for real outdoor condition,” *Solar Energy*, Volume 139, 2016, Pages 569-580, ISSN 0038-092X.

[19] Y. Hu, W. Cao, J. Ma, S. J. Finney and D. Li, “Identifying PV Module Mismatch Faults by a Thermography-Based Temperature Distribution Analysis,” *IEEE Transactions on Device and Materials Reliability*, vol. 14, no. 4, pp. 951-960, Dec. 2014, doi: 10.1109/TDMR.2014.2348195.

[20] Y. Hu, B. Gao, X. Song, G. Tian, K. Li, X. He, “Photovoltaic fault detection using a parameter based model,” *Solar Energy*, Volume 96, 2013, Pages 96-102, ISSN 0038-092X.

[21] A. C. Vasko, A. Vijh, V. G. Karpov, “Hot spots spontaneously emerging in thin film photovoltaics,” *Solar Energy*, Volume 108, 2014, Pages 264-273, ISSN 0038-092X.

[22] N. L. Georgijevic, M. V. Jankovic, S. Srdic and Z. Radakovic, “The Detection of Series Arc Fault in Photovoltaic Systems Based on the Arc Current Entropy,” *IEEE Transactions on Power Electronics*, vol. 31, no. 8, pp. 5917-5930, Aug. 2016, doi: 10.1109/TPEL.2015.2489759.

[23] B. Lecouvet, M. Sclavons, S. Bourbigot, C. Bailly, “Thermal and flammability properties of polyethersulfone/halloysite nanocomposites prepared by melt compounding,” *Polymer Degradation and Stability*, Volume 98, Issue 10, 2013, Pages 1993-2004, ISSN 0141-3910.

[24] A. Ito, T. Kashiwagi, “Characterization of flame spread over PMMA using holographic interferometry sample orientation effects,” *Combustion and Flame*, Volume 71, Issue 2, 1988, Pages 189-204, ISSN 0010-2180.

[25] P. A. Beaulieu, N. A. Dembsey, “Effect of oxygen on flame heat flux in horizontal and vertical orientations,” *Fire Safety Journal*, Volume 43, Issue 6, 2008, Pages 410-428, ISSN 0379-7112.

[26] M.B. Ayani, J.A. Esfahani, R. Mehrabian, “Downward flame spread over PMMA sheets in quiescent air: Experimental and theoretical studies,” *Fire Safety Journal*, Volume 41, Issue 2, 2006, Pages 164-169, SSN 0379-7112.

[27] M. A. Delichatsios, “Piloted ignition times, critical heat fluxes and mass loss rates at reduced oxygen atmospheres,” *Fire Safety Journal*, Volume 40, Issue 3, 2005, Pages 197-212, ISSN 0379-7112.

[28] M.C. Falvo, S. Capparella, “Safety issues in PV systems: Design choices for a secure fault detection and for preventing fire risk,” *Case Studies in Fire Safety*, Volume 3, 2015, Pages 1-16, ISSN 2214-398X.

[29] K. Murata, T. Yagiura, K. Takeda, M. Tanaka, S. Kiyama, “New type of photovoltaic module integrated with roofing material (highly fire-resistant PV tile),” *Solar Energy Materials and Solar Cells*, Volume 75, Issues 3–4, 2003, Pages 647-653.

[30] K. Chen, C. Huang, J. He, “Fault detection, classification and location for transmission lines and distribution systems: a review on the methods,” *High Voltage*, vol. 1, no. 1, pp. 25-33, 4 2016, doi: 10.1049/hve.2016.0005.

[31] L. Chen, P. Wang, L. Xu, “Novel detection method for DC series arc faults by using morphological filtering,” *The Journal of China Universities of Posts and Telecommunications*, Volume 22, Issue 5, 2015, Pages 84-91, ISSN 1005-8885.

[32] https://www.nengapp.com/news/detail/3043104

[33] S. Lee, C. Wu, K. Hung, “A Study on Fire Risks to Firefighters in the Building with Photovoltaic System,” *Proceedings of the 2017 IEEE International Conference on Applied System Innovation*, 2017.

[34] J. K. Hastings, M. A. Juds, C. J. Luebke and B. Pahl, “A study of ignition time for materials exposed to DC arcing in PV systems,” *2011 37th IEEE Photovoltaic Specialists Conference, Seattle, WA*, 2011, pp. 003724-003729.

[35] R. Tommasini, E. Pons, F. Palamara, C. Turturici, P. Colella, “Risk of electrocution during fire suppression activities involving photovoltaic systems,” *Fire Safety Journal*, Volume 67, 2014, Pages 35-41, ISSN 0379-7112.

[36] https://kknews.cc/zh-my/news/bkg4xv6.html

[37] UL 61730-2, “PV Module Safety Assessment Part 2: Test Requirements”, 2017.

[38] UL 790, “Safety Standards for Roof Fire Tests”, 2018.

[39] JG/T 492, “General Technical Requirements for Building Photovoltaic Modules”, 2016.

[40] GB8624, “Combustion Performance”, 2006.

[41] Y. Zheng, “Analysis on fire safety of integrated photovoltaic building system,” *Fire Science and Technology*, 2018. (in Chinese)

[42] L. Mazziotti, et al., “Fire risk related to the use of PV systems in building facades,” *Matec Web of Conferences*, Volume 46, 2016, 05001, Page 9. https://doi.org/10.1051/matecconf/20164605001.

[43] H. Häberlin, F. Volkenborn, M. Halfmann, et al., “Determination of fire safety risks at PV systems and development of risk minimization measures,” 2011, http://www.pv-brandsicherheit.de/fileadmin/downloads_fe/4AV.2.23_Final.pdf.

[44] Z. Zhang, J. Wu, L. Wang, F. Liu, P. Jia, L. Dai, Y. Lu, T. Bian, “The analysis on simulation and invalidation of hot-spot temperature distribution in micro-defective

crystalline silicon solar cells," *Renewable Energy*, Volume 147, Part 1, 2020, Pages 2218-2228, ISSN 0960-1481.

[45] Z. Wu, Z. Zhou, A. Mohammed, "Time-effective Dust Deposition Analysis of PV Modules Based on Finite Element Simulation for Candidate Site Determination," *IEEE Access*, 2020, PP. 1-1. 10.1109/ACCESS.2020.2985158.

[46] Z. Wu, W. Li, S. Kuka and M. Alkahtani, "Analysis of Dust Deposition on PV Arrays by CFD Simulation," *IECON 2019 - 45th Annual Conference of the IEEE Industrial Electronics Society, Lisbon, Portugal*, 2019, pp. 5439-5443.

[47] N. G. Dhere, N. S. Shiradkar, "Fire hazard and other safety concerns of photovoltaic systems," *Journal of Photonics for Energy*, 2012.

[48] F. Bayrak, H. F. Oztop, "Effects of static and dynamic shading on thermodynamic and electrical performance for photovoltaic panels," *Applied Thermal Engineering*, Volume 169, 2020, 114900, ISSN 1359-4311.

[49] X. Ju, et al., "Impact of flat roof–integrated solar photovoltaic installation mode on building fire safety," *Fire and Materials*, Volume 43, Issue 7, 2019, https://doi.org/10.1002/fam.2755.

[50] P. Dunbabin, "Fire and Solar PV Systems – Recommendations for the Fire and Rescue Services," *Scinence and Innovation*, 2017.

[51] S. Silvestre, A. Boronat, A. Chouder, "Study of bypass diodes configuration on PV modules", *Applied Energy*, Volume 86, Issue 9, 2009, Pages 1632-1640, ISSN 0306-2619.

[52] K. A. Kim, P. T. Krein, "Reexamination of Photovoltaic Hot Spotting to Show Inadequacy of the Bypass Diode", *IEEE Journal of Photovoltaics*, vol. 5, no. 5, pp. 1435-1441, Sept. 2015, doi: 10.1109/JPHOTOV.2015.244409.

[53] S. Daliento, F. D. Napoli, P. Guerriero, V. d'Alessandro, "A modified bypass circuit for improved hot spot reliability of solar panels subject to partial shading", *Solar Energy*, Volume 134, 2016, Pages 211-218, ISSN 0038-092X.

[54] M. Dhimish, V. Holmes, P. Mather, M. Sibley, “Novel hot spot mitigation technique to enhance photovoltaic solar panels output power performance”, *Solar Energy Materials and Solar Cells,* Volume 179, 2018, Pages 72-79, ISSN 0927-0248.

[55] P. Guerriero, P. Tricoli, S. Daliento, “A bypass circuit for avoiding the hot spot in PV modules”, *Solar Energy,* Volume 181, 2019, Pages 430-438, ISSN 0038-092X.

[56] M. Dhimish, G. Badran, “Current limiter circuit to avoid photovoltaic mismatch conditions including hot-spots and shading”, *Renewable Energy,* Volume 145, 2020, Pages 2201-2216, ISSN 0960-1481.

[57] Outline of investigation for photovoltaic (PV) DC arc-fault circuit protection Underwriters Laboratories (2011)

[58] G. Bao, X. Gao, R. Jiang, K. Huang, "A Novel Differential High-Frequency Current Transformer Sensor for Series Arc Fault Detection", *Sensors*, 2019.

[59] N. Gustavsson, “Evaluation and simulation of black-box arc models for high-voltage circuit breakers”, *Linköping, Sweden: Linköping University,* 2004.

[60] X. Peng, J. Lai, “Application of Clustering Analysis on Typical Power Consumption Profile Analysis”. *Power System Protection and Control*, 2014. (in Chinese)

[61] C. Yao, P. Qiao, P. Chen, Y. Chen, “Fractal antenna of 0.4~1 GHz for UHF monitoring of partial discharge in electrical equipment”. *High Voltage Engineering*, 2014, 40. 2285-2291. 10.13336/j.1003-6520.hve.2014.08.005.

[62] M. C. Damas, R. T. Robiscoe, “Detection of radio-frequency signals emitted by an arc-discharge”, *Journal of Applied Physics*, 1988, Volume 64, Issue 2 > 10.1063/1.341971.

[63] J. Johnson, S. Kuszmaul, W. Bower, D. Schoenwald, “Using PV module and line frequency response data to create robust arc fault detectors”. *Proceedings of the 26th european photovoltaic solar energy conference,* 2011. p. 3745–50.

[64] J. Johnson, D. Pahl, C. Luebke, T. Pier, T. Miller, J. Strauch, et al. “Photovoltaic DC arc fault detector testing at sandia national laboratories”. *Proceedings of the 37th IEEE photovoltaic specialist conference,* 2011 p. 3614–9.

[65] S. Chae, J. Park, S. Oh, “Series DC Arc Fault Detection Algorithm for DC Microgrids Using Relative Magnitude Comparison”, *IEEE Journal of Emerging and Selected Topics*

in Power Electronics, vol. 4, no. 4, pp. 1270-1278, Dec. 2016, doi: 10.1109/JESTPE.2016.2592186.

[66] B. Novak, "Implementing arc detection in solar applications: achieving compliance with the new UL 1699B Standard". *Texas Instrument*, 2012.

[67] S. Zhao, R. Zhang, J. Du, "Photovoltaic series Arc Fault Detection Utilizing Wavelet Tranform", *Journal of Huaqiao University*. 2017. (in chinese)

[68] H. Braun et al., "Signal processing for fault detection in photovoltaic arrays", *2012 IEEE International Conference on Acoustics, Speech and Signal Processing (ICASSP), Kyoto*, 2012, pp. 1681-1684, doi: 10.1109/ICASSP.2012.6288220.

[69] S. Buddha et al., "Signal processing for photovoltaic applications", *2012 IEEE International Conference on Emerging Signal Processing Applications, Las Vegas, NV*, 2012, pp. 115-118, doi: 10.1109/ESPA.2012.6152459.

[70] F. Schimpf and L. E. Norum, "Recognition of electric arcing in the DC-wiring of photovoltaic systems", *INTELEC 2009 - 31st International Telecommunications Energy Conference, Incheon*, 2009, pp. 1-6, doi: 10.1109/INTLEC.2009.5352037.

[71] X. Yao, L. Herrera, S. Ji, K. Zou, J. Wang, "Characteristic Study and Time-Domain Discrete- Wavelet-Transform Based Hybrid Detection of Series DC Arc Faults", *IEEE Transactions on Power Electronics*, vol. 29, no. 6, pp. 3103-3115, June 2014, doi: 10.1109/TPEL.2013.2273292.

[72] H. Zhu, Z. Wang, R. S. Balog, "Real time arc fault detection in PV systems using wavelet decomposition", *2016 IEEE 43rd Photovoltaic Specialists Conference (PVSC), Portland, OR*, 2016, pp. 1761-1766, doi: 10.1109/PVSC.2016.7749926.

[73] Z. Wang, R. S. Balog, "Arc fault and flash signal analysis in DC distribution systems using wavelet transformation", *IEEE Transactions on Smart Grid*, 2015, 6(4): 1955-1963.

[74] H. Lan, R. Zhang, "Study on the feature extraction of fault arc sound signal based on wavelet analysis", *Proceedings of the CSU-EPSA*, 2008, 20(4): 57-62.

[75] M. Rabla, E. Tisserand, P, Schweitzer, "Arc fault analysis and localisation by cross-correlation in 270 V DC", *Proceedings of IEEE Holm Conference on Electrical Contacts. Newport, USA: IEEE*, 2013: 1-6.

[76] C. Wu, W. Xu, Z. Li, L. Xu. “Arc Fault Type Identification and Circuit Protection in Photovoltaic System”, *Proceeding of the CSEE*. 2017. (in chinese)

[77] Q. Lu, T. Wang, B. He, T. Ru, D. Chen. "A new series arc fault identification method based on wavelet transform", *IECON 2017 - 43rd Annual Conference of the IEEE Industrial Electronics Society*, 2017.

[78] C. Wu, Y. Hu, Z. Li, W. Fei, “On-line Detection and Location of DC Bus Arc Faults in PV Systems Based on SSTDR”, *Proceeding of the CSEE*, 2020. (in chinese)

[79] Y. Guo, L. Wang, L. Wu, B. Jiang, “Wavelet packet analysis applied in detection of low-voltage DC arc fault”, *Proceedings of the 4th IEEE conference on industrial electronics and applications*, 2009 p. 4013–6.

[80] C. Luebke, T. Pier, B. Pahl, D. Breig, J. Zuercher, "Field test results of DC arc fault detection on residential and utility scale PV arrays," *2011 37th IEEE Photovoltaic Specialists Conference, Seattle, WA*, 2011, pp. 001832-001836.

[81] C. Wu, X. Feng, T. Yuan, Z. Li, Y. Zhong, “Photovoltaic arc fault detection method based on bp neural network”, *Acta energiae solaris sinica*, 2016, 37. 2958-2964.

[82] Y. He, Q. Xu, S. Yang, B. Yu, “A Power Load Probability Density Forecasting Method Based on RBF Neural Network Quantile Regression”, *Proceedings of the CSEE*, 2013. (in Chinese)

[83] X. Ding, H. Zhu, H. Yin, Y. Wang, “DC arc fault detection based on machine learning method”, *Transducer and Microsystem Technologies*, 2017. (in Chinese)

[84] J. A. Momoh, R. Button, “Design and analysis of aerospace arcing faults using fast fourier transformation and artificial neural network”, *Proceeding of IEEE power and energy society general meeting*, 2003, p. 788-93.

[85] X. Lu, P. Lin, S. Cheng, Y. Lin, Z. Chen, L. Wu, Q. Zheng, “Fault diagnosis for photovoltaic array based on convolutional neural network and electrical time series graph”, *Energy Conversion and Management*, Volume 196, 2019, Pages 950-965, ISSN 0196-8904.

[86] G. Zhang, “Intelligent control system and application”, *China Electric Power Press*, 2007. (in Chinese)

[87] Z. Wang, R.S. Balog, “Arc fault and flash detection in photovoltaic systems using wavelet transform and support vector machines”, *Proceedings of the IEEE 43rd photovoltaic specialists conference*, 2016. p. 3275–80.

[88] K. Yang, R. Zhang, J. Yang, C. Liu, S. Chen, F. Zhang, “A novel arc fault detector for early detection of electrical fires”, *Sensor*, 16 (2016), pp. 1-24.

[89] B. Grichting, J. Goette and M. Jacomet, “Cascaded fuzzy logic based arc fault detection in photovoltaic applications”, *2015 International Conference on Clean Electrical Power (ICCEP), Taormina*, 2015, pp. 178-183, doi: 10.1109/ICCEP.2015.7177620.

[90] Mahmoud Dhimish, Violeta Holmes, Bruce Mehrdadi, Mark Dales, Peter Mather, “Photovoltaic fault detection algorithm based on theoretical curves modeling and fuzzy classification system”, *Energy*, Volume 140, Part 1, 2017, Pages 276-290, ISSN 0360-5442.

[91] S. Martin, “Fire safety and solar electric and photovoltaic systems”, *Fire*, Volume 107, Issue 1363, 2013, Page 33.

[92]Z. Abderrezzaq, M. Mohammed, N. Ammar, S. Nordine, D. Rachid and B. Ahmed, “Impact of dust accumulation on PV panel performance in the Saharan region,” *2017 18th International Conference on Sciences and Techniques of Automatic Control and Computer Engineering (STA), Monastir*, 2017, pp. 471-475.

[93] P. Wang, J. Xie, L. Ni, L. Wan, K. Ou, L. Zheng, K. Sun, “Reducing the effect of dust deposition on the. generating efficiency of solar PV modules by super-hydrophobic films,” *Solar Energy*, Volume 169, 2018, Pages 277-283, ISSN 0038-092X

[94] S. P. Ayeng'o, H. Axelsen, D. Haberschusz, D. U. Sauer, “A model for direct-coupled PV systems with batteries depending on solar radiation, temperature and number of serial connected PV cells,” *Solar Energy*, Volume 183, 2019, Pages 120-131, ISSN 0038-092X.

[95] S. A.M. Said, G. Hassan, H. M. Walwil, N. Al-Aqeeli, “The effect of environmental factors and dust accumulation on photovoltaic modules and dust-accumulation mitigation strategies,” *Renewable and Sustainable Energy Reviews*, Volume 82, Part 1, 2018, Pages 743-760, ISSN 1364-0321.

[96] L. Hocine, K. M. Samira, “Optimal PV panel’s end-life assessment based on the supervision of their own aging evolution and waste management forecasting,” *Solar Energy*, Volume 191, 2019, Pages 227-234, ISSN 0038-092X.

[97] A. A. Hachicha, I. Al-Sawafta, Z. Said, “Impact of dust on the performance of solar photovoltaic (PV) systems under United Arab Emirates weather conditions,” *Renewable Energy*, Volume 141, 2019, Pages 287-297, ISSN 0960-1481.

[98] Y. Jiang, L. Lu, H. Lu, “A novel model to estimate the cleaning frequency for dirty solar photovoltaic (PV) modules in desert environment,” *Solar Energy*, Volume 140, 2016, Pages 236-240, ISSN 0038-092X.

[99] S. A. Sulaiman, M. N. H. Mat, F. M. Guangul, M. A. Bou-Rabee, “Real-time study on the effect of dust accumulation on performance of solar PV panels in Malaysia,” *2015 International Conference on Electrical and Information Technologies (ICEIT), Marrakech*, 2015, pp. 269-274.

[100] W. Javed, Y. Wubulikasimu, B. Figgis, B. Guo, “Characterization of dust accumulated on photovoltaic panels in Doha, Qatar,” *Solar Energy*, Volume 142, 2017, Pages 123-135, ISSN 0038-092X.

[101] L. Stone, D. Hastie, S. Zigan, “Using a coupled CFD – DPM approach to predict particle settling in a horizontal air stream,” *Advanced Powder Technology*, Volume 30, Issue 4, 2019, Pages 869-878, ISSN 0921-8831.

[102] H. Lu, W. Zhao, “Effects of particle sizes and tilt angles on dust deposition characteristics of a ground-mounted solar photovoltaic system,” *Applied Energy*, Volume 220, 2018, Pages 514-526, ISSN 0306-2619.

[103] H Lu, L. Zhang, “Influences of dust deposition on ground-mounted solar photovoltaic arrays: A CFD simulation study,” *Renewable Energy*, Volume 135, 2019, Pages 21-31, ISSN 0960-1481.

[104] H. Lu, L. Lu, Y. Wang, “Numerical investigation of dust pollution on a solar photovoltaic (PV) system mounted on an isolated building,” *Applied Energy*, Volume 180, 2016, Pages 27-36, ISSN 0306-2619.

[105] M. Bressan, A. Gutierrez, L. Garcia Gutierrez, C. Alonso, “Development of a real-time hot-spot prevention using an emulator of partially shaded PV systems,” *Renewable Energy*, Volume 127, 2018, Pages 334-343, ISSN 0960-1481.

[106] R. A. M. Ferreira, D. L.F. Pottie, L. H. C. Dias, B. J. Cardoso Filho, M. P. Porto, “A directional-spectral approach to estimate temperature of outdoor PV panels,” *Solar Energy*, Volume 183, 2019, Pages 782-790, ISSN 0038-092X.

[107] F. M. Zaihidee, S. Mekhilef, M. Seyedmahmoudian, B. Horan, “Dust as an unalterable deteriorative factor affecting PV panel's efficiency: Why and how,” *Renewable and Sustainable Energy Reviews*, Volume 65, 2016, Pages 1267-1278, ISSN 1364-0321.

[108] C. M. Jubayer, H. Hangan, “Numerical simulation of wind effects on a stand-alone ground mounted photovoltaic (PV) system,” *Journal of Wind Engineering and Industrial Aerodynamics*, Volume 134, 2014, Pages 56-64, ISSN 0167-6105.

[109] M. S. Ashhab, O. Akash, “Experiment on PV panels tilt angle and dust,” *2016 5th International Conference on Electronic Devices, Systems and Applications (ICEDSA)*, Ras Al Khaimah, 2016, pp. 1-3.

[110] R. Conceição, H. G. Silva, L. Fialho, F. M. Lopes, M. Collares-Pereira, “PV system design with the effect of soiling on the optimum tilt angle,” *Renewable Energy*, Volume 133, 2019, Pages 787-796, ISSN 0960-1481.

[111] A.A. Babatunde, S. Abbasoglu, M. Senol, “Analysis of the impact of dust, tilt angle and orientation on performance of PV Plants,” *Renewable and Sustainable Energy Reviews*, Volume 90, 2018, Pages 1017-1026, ISSN 1364-0321.

[112] Fluent Ansys Theory guide [M]. US: ANSYS Inc, 2009.

[113] W. Ge, J. Li, “Macro-scale phenomena reproduced in microscopic systems-pseudo-particle modeling of Fluidization,” *Chemical Engineering Science*, 2003, 58(8): 1565-1585.

[114] Q. Sun, H. Li, “A novel pseudo-particle model for gas in gas-solid two-phase flow,” *Engineering chemistry and metallurgy*, 1999, 3: 019.

[115] A. Busch, S. T. Johansen, “An Eulerian-Lagrangian CFD study of a particle settling in an orthogonal shear flow of a shear-thinning, mildly viscoelastic fluid,” *Journal of Non-Newtonian Fluid Mechanics*, Volume 263, 2019, Pages 77-103, ISSN 0377-0257.

[116] M. G. Chowdhury, D. Goossens, H. Goverde, F. Catthoor, “Experimentally validated CFD simulations predicting wind effects on photovoltaic modules mounted on inclined surfaces,” *Sustainable Energy Technologies and Assessments*, Volume 30, 2018, Pages 201-208, ISSN 2213-1388.

[117] C. Fountoukis, B. Figgis, L. Ackermann, M. A. Ayoub, “Effects of atmospheric dust deposition on solar PV energy production in a desert environment,” *Solar Energy*, Volume 164, 2018, Pages 94-100, ISSN 0038-092X.

[118] P. L. Carotenuto, P. Manganiello, G. Petrone, and G. Spagnuolo, “Online recording a PV module fingerprint,” *IEEE Journal of Photovoltaics*, vol. 4, no. 2, 659-668, Mar. 2014.

[119] Y. A. Mahmoud, W. Xiao, H. H. Zeineldin, “A parameterization approach for enhancing PV model accuracy,” *IEEE Trans. Ind. Electron.*, vol. 60, no.12, pp. 5708-5716, 2013.

[120] M. Z. S El-Dein, M. Kazerani, M. M. A. Salama, “Optimal photovoltaic array reconfiguration to reduce partial shading losses,” *IEEE Trans. Sustainable Energy*, Vol. 4, Issue 1, pp. 145-153, 2013.

[121] M. Mattei, G. Notton, C. Cristofari, M. Muselli, P. Poggi, “Calculation of the polycrystalline PV module temperature using a simple method of energy balance,” *Renewable Energy*, 31, pp.553-567, 2006.

[122] M. Boztepe, F. Guinjoan, G. Velasco-Quesada, S. Silvestre, A. Chouder, E. Karatepe, “Global MPPT scheme for photovoltaic string inverters based on restricted voltage window search algorithm,” *IEEE Trans. Ind. Electron.*, vol. 61, no. 7, 3302-3312, Jul. 2014.

[123] M. Abdelhamid, R. Singh, M. Omar, “Review of microcrack detection techniques for silicon solar cells”, *IEEE Journal of Photovoltaics*, vol. 4, no. 1, 514 - 524, Jan. 2014.

[124] B. N. Alajmi, K. H. Ahmed, S. J. Finney, B. W. Williams, “A maximum power point tracking technique for partially shaded photovoltaic systems in microgrids,” *IEEE Trans. Industrial Electronics*, vol. 60, no. 4, pp. 1596-1606, April 2013.

[125] Produce information, Yingli Solar Ltd, Online Available: http://www.yinglisolar.com/en/products/solar-modules/

[126] Y. Hu, Y. Deng, Q. Liu, X. He, "Asymmetry three-level grid-connected current hysteresis control with varying bus voltage and virtual over-sample method," *IEEE Trans. Power Electron.*, vol. 29, no. 6, pp. 3214-3222, Jun. 2014.

[127] B. Zhao, Q. Song, W. Liu, Y. Sun, "A synthetic discrete design methodology of high-frequency isolated bidirectional DC/DC converter for grid-connected battery energy storage system using advanced components," *IEEE Trans. Ind. Electron.*, vol. 61, no. 10, 5402- 5410, Oct. 2014.

[128] W. Li, W. Li; X. Xiang; Y. Hu; X. He. "High step-up interleaved converter with built-in transformer voltage multiplier cells for sustainable energy applications," *IEEE Trans. Power Electron.*, vol. 29, no. 6, pp. 2829-2836, Jun. 2014.

[129] S. Djordjevic, D. Parlevliet, P. Jennings, "Detectable faults on recently installed solar modules in Western Australia," *Renewable Energy*, vol. 67, 2014, 215-221.

[130] E. L. Meyer, E. Ernest van Dyk, "Assessing the reliability and degradation of photovoltaic module performance parameters," *IEEE Trans. Reliability*, vol. 53, Issue 1, pp. 83-92, Mar. 2004.

[131] E. V. Paraskevadaki, S. A. Papathanassiou, "Evaluation of MPP voltage and power of mc-Si PV modules in partial shading conditions," *IEEE Trans. Energy Conversion*, vol. 26, Issue 3, pp.923-932, 2011.

[132] C. Buerhopa, D. Schlegela, M. Niessb, C. Vodermayerb, R. Weißmanna, C. J. Brabeca, "Reliability of IR-imaging of PV-plants under operating conditions," *Solar Energy Materials and Solar Cells*, vol. 107, pp. 154-164, 2012.

[133] Z. Zou, Y. Hu, B. Gao, W. L. Woo and X. Zhao, "Study of the gradual change phenomenon in the infrared image when monitoring photovoltaic array," *Journal of Applied Physics*, vol. 115, no. 4, pp. 043522-1-11, 2014.

[134] M. Simon and E. L. Meyer, "Detection and analysis of hot-spot formation in solar cells," *Solar Energy Materials and Solar Cells*, vol. 94, no. 2, pp. 106-113, 2010.

[135] J. Kurnik, M. Jankovec, K. Brecl and M. Topic, “Outdoor testing of PV module temperature and performance under different mounting and operational conditions,” *Solar Energy Materials & Solar Cells,* vol. 95, pp. 373-376, 2011.

[136] Y. Hu, W. Cao, J. Wu, B. Ji, D. Holliday, “Thermography-based virtual MPPT scheme for improving PV energy efficiency at partial shading conditions”, *IEEE Trans. Power Electron.,* vol. 29, no. 11, pp. 5667-5672, Jun. 2014.

[137] T. Takashima, J. Yamaguchi, K. Otani, T. Oozeki, K. Kato, “Experimental studies of fault location in PV module strings,” *Solar Energy Materials and Solar Cells,* vol. 93 issues. 6-7, pp. 1079-1082, Jun. 2009.

[138] R. A. Kumar, M. S. Suresh, J. Nagaraju, “Measurement of AC parameters of gallium arsenide (GaAs/Ge) solar cell by impedance spectroscopy,” *IEEE Trans. Electron Devices,* vol. 48, issue 9, pp. 2177-2179, 2001.

[139] A. Chouder, S. Silvestre, “Automatic supervision and fault detection of PV systems based on power losses analysis,” *Energy Conversion and Management,* vol. 51, issue 10, pp. 1929-1937, Oct. 2010.

[140] S. Silvestre, A. Chouder, E. Karatepe, “Automatic fault detection in grid connected PV systems,” *Solar Energy,* vol. 94, pp. 119-127, Aug. 2013.

[141] D. Nguyen， B. Lehman. “An adaptive solar photovoltaic array using model-based reconfiguration algorithm,” *IEEE Trans. Ind. Electron.,* vol. 55, no. 7, pp. 2644-2654, Jul. 2008.

[142] P. Jonathan Storey, Peter R. Wilson, and Darren Bagnall, “Improved Optimization Strategy for Irradiance Equalization in Dynamic Photovoltaic Arrays,” *IEEE Trans. Power Electron.,* vol. 28, no. 6, 2946–2956, Jun. 2013.

[143] S. Jonathan, R. W. Peter, and B. Darren, “The Optimized-String Dynamic Photovoltaic Array,” *IEEE Trans. Power Electron.,* vol. 29, no. 4, 1768–1776, Apr. 2014.

[144] Y. Wang, X. Lin, Y. Kim, N. Chang, and M. Pedram, “Architecture and control algorithms for cmbating partial shading in photovoltaic sstems,” *IEEE Trans. Computer-Aided Design Integr. Circuits Syst.,* vol. 33, no. 6, 917-929, Jun. 2014.

[145] G. Velasco-Quesada, F. Guinjoan-Gispert, R. Pique-Lopez, M. RomanLumbreras, and A. Conesa-Roca, "Electrical PV array reconfiguration strategy for energy extraction improvement in grid-connected PV systems," *IEEE Trans. Ind. Electron.*, vol. 56, no. 11, pp. 4319–4331, Nov. 2009.

[146] A. Ndiaye, C. M.F. Kebe, A. Charki, P. A. Ndiaye, V. Sambou, A. Kobi, "Degradation evaluation of crystalline-silicon photovoltaic modulesafter a few operation years in a tropical environment," *Solar Energy*, vol. 103, pp. 70–77, Feb. 2014.

[147] C.R. Osterwald, A. Anderberg, S. Rummel, L. Ottoson, "Degradation Analysis of Weathered Crystalline-Silicon PV Modules," *29th IEEE Photovoltaic Specialists Conference,New Orleans, Louisiana,*2002.

[148] L. Cristaldi, M. Faifer, M. Rossi, S. Toscani, M. Catelani, L. Ciani, M. Lazzaroni, "Simplified method for evaluating the effects of dust and aging on photovoltaic panels," *Measurement*, vol. 54, pp. 207–214, Aug. 2014.

[149] Ababacar Ndiaye, Cheikh M. F. Kébé, Pape A. Ndiaye, Abdérafi Charkib, Abdessamad Kobi, Vincent Sambou. "A Novel Method for Investigating Photovoltaic Module Degradation," *Energy Procedia*, 36 (2013) 1222 – 1231.

[150] M.A. Munoz, M.C. Alonso-Garcia, Nieves Vela, F. Chenlo. "Early degradation of silicon PV modules and guaranty conditions," *Solar Energy*, 85 (2011) 2264–2274.

[151] D. Chianese, N Cereghetti, S. Rezzonico, and G. Travaglini, "18 Types of PV Modules Under the Lens," *Proc.16th Euro. PV Sol. Energy Conf., Glasgow, Scotland*, 2000.

[152]REN21. "Renewables 2019 Global Status Report". https://ren21.net/gsr-2019/pages/foreword/foreword/.

[153] H. Forstner, S. Bandil, et al., "International Technology Roadmap for Photovoltaic (ITRPV) 2013 Results", 24 March 2014.

[154] A. Luque, A. Cuevas, J.M. Ruiz, "Double-sided n+–p–n+ solar-cell for bifacial concentration", *Solar Cells*, Oct 1980, vol 2, P151–166.

[155] A. Cuevas, A. Luque, J. Eguren, J. del Alamo, "50 Per cent more output power from an albedo-collecting flat panel using bifacial solar cells", *Solar Energy*, Volume 29, Issue 5, 1982, Pages 419-420, ISSN 0038-092X, https://doi.org/10.1016/0038-092X(82)90078-0.

[156] S. F. A. Shah, I. A. Khan and H. A. Khan, “Performance Evaluation of Two Similar 100MW Solar PV Plants Located in Environmentally Homogeneous Conditions”, *IEEE Access,* vol. 7, pp. 161697-161707, 2019, doi: 10.1109/ACCESS.2019.2951688.

[157]United States Environmental Protection Agency (USEPA), “EPA’s Composite Model for Leachate Migration with Transformation Products (EPACMTP)”, *Parameter/Data Background Document,* 2003.

[158] H. H. Zondag, W. V. Helden, “Materials Science stagnation temperature in PVT collector”, *Materials Science,* 2002,

[159] N. Shao, L. Ma, J. Zhang, “Experimental study on electrical and thermal performance and heat transfer characteristic of PV/T roof in summer”, *Applied Thermal Engineering,* Volume 162, 2019, 114276, ISSN 1359-4311,

[160] P. Anbu, B. Kamal, D. Thiruvadigal, S, Sakthivel, “Fire Hazards and Overheating Caused by Shading Faults on Photo Voltaic Solar Panel”, *Fire Technology,* 2015, 52. 10.1007/s10694-015-0509-7.

[161] A. Tewarson, “Flammability Parameters of Materials: Ignition, Combustion, and Fire Propagation *”, *Journal of Fire Sciences,* July 1st 1994, Volume: 12 issue: 4, page(s): 329-356.

[162] Z. Wu, Y. Hu, J. X. Wen, F. Zhou and X. Ye, “A Review for Solar Panel Fire Accident Prevention in Large-Scale PV Applications”, *IEEE Access,* vol. 8, pp. 132466-132480, 2020, doi: 10.1109/ACCESS.2020.3010212.

[163] H. K. Hajjar, F. A. Dubaikel and I. M. Ballard, “Bifacial photovoltaic technology for the oil and gas industry”, *2015 Saudi Arabia Smart Grid (SASG), Jeddah,* 2015, pp. 1-4, doi: 10.1109/SASG.2015.7449283.

[164] E. Luque, F. Antonanzas-Torres, R. Escobar, “Effect of soiling in bifacial PV modules and cleaning schedule optimization”, *Energy Conversion and Management,* Volume 174, 2018, Pages 615-625, ISSN 0196-8904, https://doi.org/10.1016/j.enconman.2018.08.065.

[165] J. Appelbaum, “Bifacial photovoltaic panels field,” *Renewable Energy*, Volume 85, 2016, Pages 338-343, ISSN 0960-1481, https://doi.org/10.1016/j.renene.2015.06.050.

[166] Th. Katsaounis, K. Kotsovos, I. Gereige, A. Basaheeh, M. Abdullah, A. Khayat, E. Al-Habshi, A. Al-Saggaf, A.E. Tzavaras, "Performance assessment of bifacial c-Si PV modules through device simulations and outdoor measurements", *Renewable Energy*, Volume 143, 2019, Pages 1285-1298, ISSN 0960-1481,

[167] Y. Zhang, Y. Yu, F. Meng and Z. Liu, "Experimental Investigation of the Shading and Mismatch Effects on the Performance of Bifacial Photovoltaic Modules", *IEEE Journal of Photovoltaics*, vol. 10, no. 1, pp. 296-305, Jan. 2020, doi: 10.1109/JPHOTOV.2019.2949766.

[168] A. Asgharzadeh, B. Marion, C. Deline, C. Hansen, J. S. Stein and F. Toor, "A Sensitivity Study of the Impact of Installation Parameters and System Configuration on the Performance of Bifacial PV Arrays", *IEEE Journal of Photovoltaics,* vol. 8, no. 3, pp. 798-805, May 2018, doi: 10.1109/JPHOTOV.2018.2819676.

[169]Wu Shiqin, "Design and research of photovoltaic power generation system with double-sided photovoltaic modules," *Solar energy,* 2019(05):30-33+41.

[170] R. Perez, P. Ineichen, R. Seals, "Modeling daylight availability and irradiance components from direct and global irradiance," *Solar Energy,* 1990, 44(5):271-289.

[171] B. Marion, "Numerical method for angle-of-incidence correction factors for diffuse radiation incident photovoltaic modules," *Solar Energy*, 2017, 147(MAY):344-348.

[172] B. Marion, "A practical irradiance model for bifacial PV modules," *2017 IEEE 44th Photovoltaic Specialist Conference (PVSC)*, Washington, DC, 2017, pp. 1537-1542.

[173]A. Lorenzo, G. Sala, S. Lopez-Romero, "Diffusing reflectors for bifacial photovoltaic panels," *Solar Cells,* 13: 277-292, 1985.

[174] U. Yusufoglu, U. Pletzer, L. Koduvelikulathu, "Analysis of the annual performance of bifacial modules and optimization methods," *IEEE Journal of Photovoltaics*, 5: 320-328.

[175] J. Bai, "Modeling, simulation and optimization of solar photovoltaic system," *Electronic Industry Press,* 2014.

[176] Van Kerschaver E, Zechner C, Dicker J. "Double sided minority carrier collection in silicon solar cells," *IEEE Transactions on Electron Devices*, vol. 47, no. 4, pp. 711-717, April 2000.

[177] J. Zhang, G. Hao, H. Li, et., “Effects of different ground backgrounds on the power generation performance of double-sided photovoltaic modules,” *Acta solar energy*, 2020,41(03):298-304.

[178] Q. Tao, Z. Li, F. Jiang, “Daily solar radiation estimation based on meteorological and air quality observation data,” *Journal of jimei university (natural science edition)*, 2014,19(05):369-374.

[179] Warabisako T, Matsukuma K, Kokuna S, “Bifacial multicrystalline silicon solar cell,” *Conference Record of the Twenty Third IEEE Photovoltaic Specialists Conference - 1993* (Cat. No.93CH3283-9), Louisville, KY, USA, 1993, pp. 248-251.

[180]Su Jianhui, Yu Shijie, Zhao Wei, “mathematical model for silicon solar cell engineering”, *Journal of solar energy*, 2001(04):409-412.

[181] Wu Chunhua, Xu Kun, Huang Jianming, “Research on photovoltaic distributed MPPT based on non inverse buck boost converter,” *New electrical energy technology*, 2011,30(04):84-8.

[182] C. D. Rodríguez-Gallegos, M. Bieri, O. Gandhi, J. P. Singh, Th. Reindl, S.K. Panda, “Monofacial vs bifacial Si-based PV modules: Which one is more cost-effective?”, *Solar Energy*, Volume 176, 2018, Pages 412-438, ISSN 0038-092X, https://doi.org/10.1016/j.solener.2018.10.012.

[183] J. G. Quintiere, “A theoretical basis for flammability properties”, *Fire and materials*, 28th October 2005, Volume30, Issue3 P175–214, https://doi.org/10.1002/fam.905.

[184] B.T. Rhodes, J.G. Quintiere, “Burning rate and flame heat flux for PMMA in a cone calorimeter”, *Fire Safety Journal*, Volume 26, Issue 3, 1996, Pages 221-240, ISSN 0379-7112, https://doi.org/10.1016/S0379-7112(96)00025-2.

[185] W. Gu, T. Ma, M. Li, L. Shen, Y. Zhang, “A coupled optical-electrical-thermal model of the bifacial photovoltaic module”, *Applied Energy*, Volume 258, 2020, 114075, ISSN 0306-2619, https://doi.org/10.1016/j.apenergy.2019.114075.

[186] A. Bjerg, K. Christoffersen, H. Sørensen, J. Hærvig, “Flow structures and heat transfer in repeating arrangements of staggered rectangular winglet pairs by Large Eddy Simulations: Effect of winglet height and longitudinal pitch distance”, *International*

Journal of Heat and Mass Transfer, Volume 131, 2019, Pages 654-663, ISSN 0017-9310, https://doi.org/10.1016/j.ijheatmasstransfer.2018.11.015.

[187] D. Berrian, J. Libal, M. Klenk, H. Nussbaumer and R. Kopecek, "Performance of Bifacial PV Arrays With Fixed Tilt and Horizontal Single-Axis Tracking: Comparison of Simulated and Measured Data", *IEEE Journal of Photovoltaics*, vol. 9, no. 6, pp. 1583-1589, Nov. 2019, doi: 10.1109/JPHOTOV.2019.2924394.

[188] Z. Zhang, M. Wu, Y. Lu, C. Xu, L. Wang, Y. Hu, F. Zhang, "The mathematical and experimental analysis on the steady-state operating temperature of bifacial photovoltaic modules", *Renewable Energy*, Volume 155, 2020, Pages 658-668, ISSN 0960-1481, https://doi.org/10.1016/j.renene.2020.03.121.